Bridging Models and Mechanisms: Integrating Proteome Remodeling with Antibiotic Response

by

Brittany Howell

A thesis
presented to the University of Waterloo
in fulfillment of the
thesis requirement for the degree of
Doctor of Philosophy
in
Applied Mathematics

Waterloo, Ontario, Canada, 2025

© Brittany Howell 2025

Examining Committee Membership

The following served on the Examining Committee for this thesis. The decision of the Examining Committee is by majority vote.

External Examiner:	Dr. Rosalind Allen Professor, Institute of Microbiology Friedrich Schiller University of Jena
Supervisor(s):	Dr. Matthew Scott Associate Professor, Dept. of Applied Mathematics University of Waterloo
Internal Member:	Dr. Brian Ingalls Professor, Dept. of Applied Mathematics University of Waterloo
	Dr. Sue Ann Campbell Professor, Dept. of Applied Mathematics University of Waterloo
Internal-External Member:	Dr. Christian Euler Assistant Professor, Dept. of Chemical Engineering University of Waterloo

Author's Declaration

I hereby declare that I am the sole author of this thesis. This is a true copy of the thesis, including any required final revisions, as accepted by my examiners.

I understand that my thesis may be made electronically available to the public.

Abstract

Antibiotic resistance is an urgent challenge in medicine, and treatment outcomes are often moulded not only by genetic resistance but by the physiological adaptation of bacteria under drug exposure. Comprehending these constraints requires integrating how translational capacity, nutrient supply, and global feedback cooperatively determine recovery and survival. This thesis extends and validates a mechanistic model that integrates nutrient-dependent growth laws with dynamic proteome allocation to capture *Escherichia coli*'s response to pulse-dose exposure to the ribosome-targeting antibiotic tetracycline in glucose- and glycerol-based media. Experimental measurements of growth delay times, RNA/protein ratios, and inhibition curves supplied direct physiological targets that guided model refinement, making certain that theory remained connected to reproducible lab data. The modeling effort highlighted two crucial effects that had previously been overlooked. First, following the removal of a ribosome-targeting antibiotic, ribosomes no longer constitute the primary limiter of growth, unlike their role under most steady-state conditions. Second, a proportional feedback controller based on the non-steady-state mismatch in amino acid flux was necessary to capture the rapid timescales of antibiotic adaptation and post-pulse recovery.

The resulting model reconciled all experimental datasets across both carbon sources, reproducing delay time plateaus, RNA/protein recovery dynamics, and inhibition profiles in a physiologically interpretable way. Sensitivity and Hessian analyses showed that recovery dynamics are primarily governed by transport rates and the strength of feedback control, whereas shifts in how binding and transport interact have little influence on the resulting physiological behavior predicted by the model. This contrast showcases which regulatory components are necessary for shaping recovery and which play only a minor, compensatory role. Clinically, the model argues against prolonged dosing, which permits rapid recovery during treatment, and instead supports pulses that maximize growth inhibition for a fixed total amount of antibiotic. Such regimes minimize the time bacteria spend in sub-inhibitory drug concentrations, thus limiting the opportunity for resistant variants to emerge, and provide a quantitative rationale for pulse- and intermittent-dosing strategies that exploit the post-antibiotic effect. More broadly, this work exemplifies how combining experiments with physiologically grounded modeling can illustrate unifying supply–demand principles of bacterial adaptation. Although developed for *E. coli* and tetracycline, the mathematical modeling framework is readily adaptable to other reversibly binding ribosome-targeting antibiotics, and could possibly be extended to other antibiotic classes, offering a foundation for linking physiology to treatment strategies in diverse microbial environments.

Acknowledgements

Pursuing this work has been both a challenge and a privilege. I am grateful to those who shared their wisdom, support, and encouragement.

First and foremost, I wish to thank my supervisor, Dr. Matthew Scott. Matt, your mentorship has made me a better student, scientist, and mathematician. You taught me to ask *why* rather than merely what. Your guidance and insight have shaped this research and the way I think about problems.

Thank you to my committee members, Dr. Brian Ingalls and Dr. Sue-Ann Campbell, for careful reading and constructive criticism that improved the clarity and rigor of this work. I am also grateful to my examiners, Dr. Christian Euler and Dr. Rosalind Allen, for generously giving their time and thoughtful feedback.

I would like to acknowledge my high-school mathematics teacher, John French, whose passion and encouragement set me on this path. I am deeply grateful to my undergraduate supervisor, Dr. Olga Vasilyeva, for sparking my interest in applied mathematics, and to my Master's supervisor, Dr. Hermann Eberl, for introducing me to the intersection of mathematics and biology. Their early guidance played an important role in the trajectory that led to this work.

To my colleague and dear friend Dr. Stéphanie Abo. Thank you for your unwavering friendship and for the many therapeutic conversations, academic and personal. Merci pour tout, ma chère. Thanks also to my colleagues and collaborators Dr. Atiyeh (Ati) Ahmadi, Mohammad Zim, Dr. Aaron Yip, Mohammad Abrar, and Yujie (Jack) Zhang, for helpful discussions, feedback, and for being generous with your time and expertise in and out of the lab.

To my family, Frances, Randy, and Shawn. Mom, Dad, and Bud, thank you for always believing in me, for instilling the value of hard work, and for supporting my education at every step. I hope I have made you proud. I would also like to thank our cat, Ron, for being a sweet and cuddly companion when I needed a break. And a special thanks to coffee and iced capps for fueling the long days and nights that carried me to the end of this thesis.

To my husband Malhar. You have been my rock throughout this journey. Thank you for encouraging me to pursue this research, for pushing me to master my craft, for reading drafts, and for your late-night reassurance. Your support has meant more than words can say. You are my best friend, and I would not be the person I am today without you.
I love you.

Dedication

Dedicated to growth, in both cells and in thought.

Table of Contents

Examining Committee ii

Author's Declaration iii

Abstract iv

Acknowledgements v

Dedication vi

List of Figures xi

List of Tables xiii

1 Introduction 1

2 Biological Background 5

2.1 Introduction to Bacteria and the Model Organism *Escherichia coli* 5

2.2 Bacterial Growth Dynamics 7

2.2.1 Introduction 7

2.2.2 Phases of Bacterial Growth 8

2.2.3 Quantitative Measures of Growth 11

2.2.4 Bacterial Growth Environments: Emphasis on Batch Culture 12

2.2.5 Mathematical & Computational Models of Bacterial Growth 13
2.3 Bacterial Physiology 14
2.3.1 Growth Physiology 14
2.3.2 "Growth Laws" 15
2.3.3 Proteome Partitioning 15
2.4 Antibiotics and their Cellular Targets 18
2.4.1 Overview of Antibiotics and Mechanisms 18
2.4.2 Major Antibiotic Targets 19
2.5 Proteomic Response to Stress 23

3 Mathematical Background **25**
3.1 Foundational Models and Their Limitations 25
3.1.1 Our Correction: New Growth Regime 33
3.2 Antibiotic Inhibition Modeling 36
3.3 Sensitivity Analysis 36
3.3.1 First-Order Sensitivity Analysis 37
3.3.2 One-at-a-Time Perturbation Strategy 37
3.3.3 Second-Order Sensitivity and Hessian Estimation 38
3.3.4 Composite Parameters and Coupled Effects 39
3.4 Parameter Estimation and Model Fitting 40
3.4.1 Information Criteria for Model Comparison 40

4 Materials & Methods **42**
4.1 Quantities of Interest 42
4.2 Experimental Design 44
4.2.1 Growth of Bacterial Culture 44
4.2.2 Growth Experiments 45
4.2.3 Model-Based Rationale for Pulse-Dose Experiments 49

4.2.4 RNA and Protein Quantification . . . 52
4.2.5 Experimental Data Summary . . . 53
4.3 Mathematical Methods . . . 55
4.3.1 Physiological Constraints and Model Assumptions . . . 56
4.3.2 Model Simulation . . . 57
4.3.3 Parameter Initialization and Bounds . . . 58
4.3.4 Sensitivity Analysis . . . 59
4.3.5 Optimization Procedures . . . 59

5 Results **62**
5.1 Overview of Modeling Goals and Strategy . . . 62
5.2 Initial Corrections and Experimental Characterization . . . 63
5.3 Model Fitting and Optimization Framework . . . 64
5.3.1 Early Fitting Attempts and Challenges . . . 64
5.3.2 Sensitivity Analysis of the Initially Corrected Model . . . 69
5.3.3 Enhancing the Fitting Framework . . . 70
5.4 Mathematical Model with Proportional Feedback Synthesis . . . 72
5.4.1 Mechanistic Interpretation of the Proportional Feedback . . . 75
5.5 Sensitivity and Hessian Analysis . . . 79
5.5.1 Local Sensitivity of Pulse-Phase RNA/Protein Ratio . . . 79
5.5.2 Hessian Eigenvector Analysis . . . 81
5.5.3 Model Comparison Across Successive Refinements . . . 81

6 Discussion **85**
6.1 Foundations and Model Evolution . . . 85
6.2 Physiological Correction: Post-Pulse Metabolic Limitation . . . 86
6.3 Physiological Role of the Proportional Feedback Controller . . . 89
6.4 Therapeutic Implications and Optimal Pulse Duration . . . 90

6.5 Limitations & Challenges . . . 92
6.5.1 Model Structure . . . 92
6.5.2 Experimental Constraints . . . 93
6.5.3 Computational Challenges . . . 93
6.5.4 Scope of Applicability . . . 94
6.6 Future Directions and Broader Implications . . . 94
6.6.1 Model Extensions . . . 95
6.6.2 Physiology-Informed Antibiotic Strategies . . . 97
6.6.3 Resistance Mechanisms and Proteomic Adaptation . . . 99
6.6.4 Generalizability and Robustness of the Framework . . . 101

7 Conclusion **103**
7.1 Summary of Contributions . . . 103
7.2 Broader Implications . . . 105

References **107**

APPENDIX **126**

List of Figures

2.1 Cellular organization of *E. coli* and the ribosome-driven translation process. 6

2.2 Phases of bacterial growth. 9

2.3 Proteome partitioning into functional sectors. 16

2.4 Mechanism of tetracycline inhibition. 21

3.1 Linear constraints between ribosome concentration and growth rate. 27

3.2 Mechanistic schematic of ribosome-targeting antibiotic interactions. 29

3.3 Modeled bacterial growth rate dynamics in response to a ribosome-targeting antibiotic pulse. 35

3.4 Contour plot of the quadratic cost approximation. 38

4.1 Illustration of delay time Δt from growth trajectories. 44

4.2 Hypothesized relationship between pulse length and delay time for different values of the drug-free growth rate (λ_0). 48

5.1 Initial corrected model fitting under glucose and glycerol 66

5.2 Growth-rate trajectory during a long antibiotic pulse illustrating piecewise regimes. 68

5.3 Model fits incorporating proportional feedback on synthesis under glucose and glycerol conditions. 74

5.4 Proportional feedback control of ribosome synthesis and growth recovery. . 78

5.5 Sensitivity analysis of the pulse-phase RNA/protein ratio 80

5.6 Hessian eigenvector component histograms 82

5.7 Comparison of model formulations across growth phases 83

6.1 Optimal pulse duration inferred from delay time saturation. 91
6.2 Example antibiotic interaction network in *E. coli*. 99
6.3 Exponential convergence underlying the delay time plateau. 102

List of Tables

4.1 Inhibition curve growth rate data at multiple tetracycline concentrations. . 54

4.2 Delay time measurements across pulse durations T for glucose and glycerol. 54

4.3 Normalized RNA/Protein ratios measured across experimental phases for a pulse of length $T = 4\,h$. 55

5.1 Optimal parameters for the initial revised model under glucose and glycerol conditions. 69

5.2 Local sensitivity of Δt and ρ for the initially corrected model 70

5.3 Optimal parameters for the proportional feedback controller under glucose and glycerol conditions. 73

5.4 Information-criterion comparison of model refinements 84

Chapter 1

Introduction

Antibiotic resistance is one of the most considerable challenges in modern medicine. Bacterial infections that were once easily treated are now increasingly persistent, with resistance mechanisms spreading across species and domains [7]. Without new strategies, antibiotic resistance threatens to set back decades of progress and make routine procedures incredibly risky. These grounds motivate the need to study not only how bacteria evolve genetic resistance, but also how they adapt physiologically to transient antibiotic exposure [70][128]. This thesis' foundation is the quantitative study of how bacterial growth physiology guides the dynamics of recovery from ribosome-targeting antibiotic exposure. Bacterial adaptation to antibiotics is not instantaneous or invariable. Cells adjust their growth, metabolism, and protein synthesis machinery dynamically, often recovering after drug removal in reproducible ways [50][55]. Knowledge of these dynamics is critical, because recovery during or after treatment affects treatment efficacy, persistence, and the probability of resistance evolution [72][177]. In particular, *Escherichia coli* provides a model organism. It is genetically compliant, experimentally accessible, and its physiology has been characterized thoroughly across nutrient conditions and antibiotic exposures [141][184][189]. Studying *E. coli* under controlled laboratory settings thus provides a powerful view into the physiological principles that underlie bacterial transformation.

Vital to bacterial physiology is the finite allocation of cellular resources. A bacterial cell cannot maximize all processes simultaneously. Its proteome, the complete set of proteins expressed by the cell, must be partitioned across competing requirements such as ribosome production, metabolic and nutrient uptake functions, and protective or repair proteins [12][136][189][232]. Because the total protein concentration is approximately constant, increasing the concentration of one group of proteins necessarily reduces the concentration of other proteins, so this partitioning imposes fundamental constraints on growth [192].

This concentration homeostasis arises because protein synthesis and cell volume expansion are tightly coupled, maintaining a nearly constant cytoplasmic protein density across steady-state conditions [189][192]. When nutrients are abundant, ribosome synthesis is upregulated, accelerating growth. Under nutrient scarcity, ribosome synthesis decreases and proteome mass shifts toward catabolic and transport proteins [207][231]. In contrast, when translation is inhibited by a ribosome-targeting antibiotic, cells increase ribosome synthesis even as growth slows, yielding a near-linear negative correlation between ribosome abundance and growth rate [189][192]. These trade-offs are not arbitrary, they follow replicable relationships known as bacterial "growth laws" that link ribosome concentration to growth rate [44][189]. Such laws provide a mechanistic window for understanding how bacteria respond to antibiotics. When translation is limited, the cell reallocates proteome mass according to the same underlying principles that control nutrient shifts [71]. This evident growth rate dependence of ribosome abundance outlines a leading difficulty in predicting bacterial responses to ribosome-targeting antibiotics. The concentration of the antibiotic's primary target is itself growth-regulated and thus changes with the physiological state of the cell.

Clinically, antibiotics are seldom delivered as a constant dose. Instead, patients experience fluctuating exposures determined by absorption, distribution, metabolism, and excretion. Pulse or intermittent-dosing regimens therefore better reflect real treatment scenarios than static exposures [89][209]. From a physiological perspective, pulses impose a dynamic challenge. Cells must shift their proteome by increasing ribosome synthesis during inhibition and reallocating resources again during recovery. These time-dependent changes in growth and allocation cannot be captured by steady-state measurements or models, which describe only fixed conditions. [4][20]. They also inform treatment strategies, poorly timed or prolonged administration could allow bacteria to recover during exposure, while carefully adjusting pulse timing can redistribute a fixed total drug exposure to maximize growth inhibition [72]. Mathematical models provide a way to formalize these processes and test hypotheses. However, most existing models either focus purely on nutrient limitation or on antibiotic inhibition, rarely both together [117][190]. A motivation for this work is the recognition that, although ribosome abundance is firmly growth-rate-dependent, ribosomes themselves are not the limiting factor for growth once antibiotic inhibition is removed. After a ribosome-targeting antibiotic pulse, the cell's capacity to recover is controlled instead by how quickly it reallocates proteome fraction to metabolic functions. Following this shift in the growth-limiting sector is critical for explaining the dynamics of post-pulse recovery.

This thesis extends and validates a unified mathematical model that integrates nutrient-dependent growth laws with antibiotic-target interactions. In this model, ribosome synthesis is given by a proportional feedback controller that responds to the imbalance between

nutrient supply and translational demand. This simple representation is consistent with the qualitative behaviour expected from ppGpp-mediated regulation and proved sufficient to reproduce the observed post-pulse recovery dynamics, thereby linking experimental observations with physiological constraints. Overall, this thesis showcases that a simple proportional feedback synthesis representation within the model can reconcile various observations of bacterial recovery, showing that the interaction between nutrient supply and ribosome demand is a useful organization principle for interpreting these dynamics.

The remainder of this thesis is structured as follows, combining biological background, mathematical formulation, experimental verification, and quantitative modeling to investigate the dynamics of bacterial growth under antibiotic stress.

Chapter 2 – Biological Background

This chapter presents the biological framework required to contextualize the modeling process. It is comprised of fundamental concepts in bacterial physiology, the biology of *E. coli*, modes of antibiotic action, and cellular adaptations to environmental and pharmacological stressors. The role of ribosome-targeting antibiotics and proteomic resource allocation are highlighted as central motifs throughout the work.

Chapter 3 – Mathematical Background

This chapter outlines the mathematical principles used throughout the thesis to model bacterial growth and antibiotic response. The focus here is narrowed to concepts directly applied in this work. These include bacterial growth laws, ribosome inhibition frameworks, and the Langmuir binding and transport relationship that guide antibiotic uptake. Methods for parameter estimation and fitting are introduced, along with sensitivity and Hessian-based techniques for evaluating model robustness and parameter influence. Together, these tools establish the mathematical bases for developing, calibrating, and interpreting the proportional feedback controller presented in later chapters.

Chapter 4 – Materials & Methods

This chapter summarizes the experimental techniques used to produce data for model validation. It details the culture conditions, growth media compositions, antibiotic administration protocols, and procedures for measuring bacterial growth, delay times, and RNA/protein ratios.

Chapter 5 – Results

This chapter presents the progressive refinement of the pulse-response model. It begins with experimental growth-inhibition curves and delay time measurements for *E. coli* in glucose and glycerol, establishing baseline IC_{50} values and recovery patterns. Successive modeling refinements are then discussed. First, removal of the post-pulse growth rate overshoot through nutrient-limited recovery, and finally, culminating in the development of a proportional feedback controller in the model, which connects ribosome synthesis dynamics to the imbalance between nutrient-limited and translation-limited growth. RNA/protein ratios are used alongside delay times and inhibition curves to validate each refinement and proteome allocation. The chapter concludes with sensitivity and Hessian analyses, which identify dominant physiological controls, stiff and sloppy parameter combinations, and compensatory couplings between binding, transport, and feedback regulation.

Chapter 6 – Discussion

This chapter compiles the results into a broader narrative. It highlights how the proportional feedback controller formulation in the model provides an integrated description of nutrient-limited and antibiotic-limited growth within a single, simple control response, and discusses its implications for pulse dosing, post-pulse recovery, and proteome reallocation. The findings are placed in the context of antibiotic therapy design, linking physiological constraints to pharmacokinetic/pharmacodynamic (PK/PD) frameworks. Limitations and challenges are assessed, including coarse-graining of proteome allocation, experimental scope, and parameter identifiability. Future directions are outlined, ranging from explicit ppGpp dynamics and whole-proteome extensions to adaptation under non-ribosomal antibiotics, host environments, and resistance evolution.

Chapter 7 – Conclusion

The final chapter summarizes the primary contributions of the thesis. It echoes that the proportional feedback controller in the model successfully captures the observed recovery dynamics from antibiotic pulses by balancing nutrient supply and ribosome demand, providing a consolidated explanation for delay times, RNA/protein ratio adaptation, and inhibition curves across conditions. Broader implications are drawn for microbiology and clinical practice, including the rationale for higher-intensity dosing strategies, the risks of prolonged low-dose exposure, and the general applicability of proportional feedback principles to other antibiotics and microbial systems. The chapter closes with a perspective on how integrating experiments with physiologically grounded modeling can inform both basic biology and translational strategies against antibiotic resistance.

Chapter 2

Biological Background

2.1 Introduction to Bacteria and the Model Organism *Escherichia coli*

Bacteria are the most prevalent organisms on Earth. Their success stems from exceptional adaptability, driven by metabolic variety and genetic plasticity, which allows bacteria to acquire new traits and thrive under diverse and extreme conditions [51]. Bacteria greatly influence the cycling of carbon, nitrogen, sulfur, and phosphorus, maintaining Earth's chemical balance and supporting life. These include nitrogen-fixing species such as *Rhizobium*, sulfate-reducing bacteria, and cyanobacteria that carry out oxygenic photosynthesis [58]. Microbial contributions extend into climate modulation, symbiosis, and biotechnology. Among these organisms, *Escherichia coli* has become the principal microbe for understanding bacterial physiology and metabolism. It is a rod-shaped, Gram-negative bacterium belonging to the *Enterobacteriaceae* family. Gram-negative bacteria have an inner cytoplasmic membrane, a thin peptidoglycan layer, and an outer membrane containing lipopolysaccharides. This envelope affects permeability to nutrients and many antibiotics, including ribosome-targeting drugs (see Figure 2.1A) [204]. *E. coli* is also a facultative anaerobe, able to respire aerobically when oxygen is present or shift to fermentation or to anaerobic respiration using alternative terminal electron acceptors [17][121]. These physiological traits, together with its rapid growth (approximately 40 minute generation time at 37°C in minimal medium, shorter in rich medium) and its broad temperature tolerance (optimum near 39°C, viable from 8–48°C), make it a fundamental organism for quantitative studies of bacterial growth and physiology [140].

E. coli is notable for its ability to adapt its physiology to environmental conditions such as nutrient availability, temperature, osmolarity, and exposure to antibiotics, such as tetracycline which inhibits protein synthesis by blocking the A-site of the ribosome and preventing aminoacyl-tRNA from entering during the elongation step of translation (see Figure 2.1B) [115]. Its metabolic versatility, switching between carbon sources and adjusting macromolecular synthesis to nutrient supply, enables it to maintain growth across diverse environments. Under aerobic conditions it generates adenosine triphosphate (ATP) mainly through oxidative phosphorylation using oxygen as the terminal electron acceptor, with the tricarboxylic-acid (TCA) cycle providing biosynthetic precursors and reducing power. Under oxygen-limited conditions it shifts to fermentation or to anaerobic respiration using alternative terminal electron acceptors such as nitrate or fumarate [17][121]. A defining feature of *E. coli* physiology is the tight regulation of macromolecular synthesis, especially of ribosomes, in response to nutrient supply. Ribosome concentration increases in nutrient-rich conditions and decreases in nutrient-poor conditions, a relationship first quantified in early studies of bacterial growth and later formalized in a "growth law" framework [184][189]. Because protein synthesis is rate-limiting for biomass accumulation, the ribosome concentration and the polypeptide-elongation rate together determine the achievable growth rate. Perturbations to ribosome function, whether by mutation or by ribosome-targeting antibiotics, proportionally reduce growth [156][236].

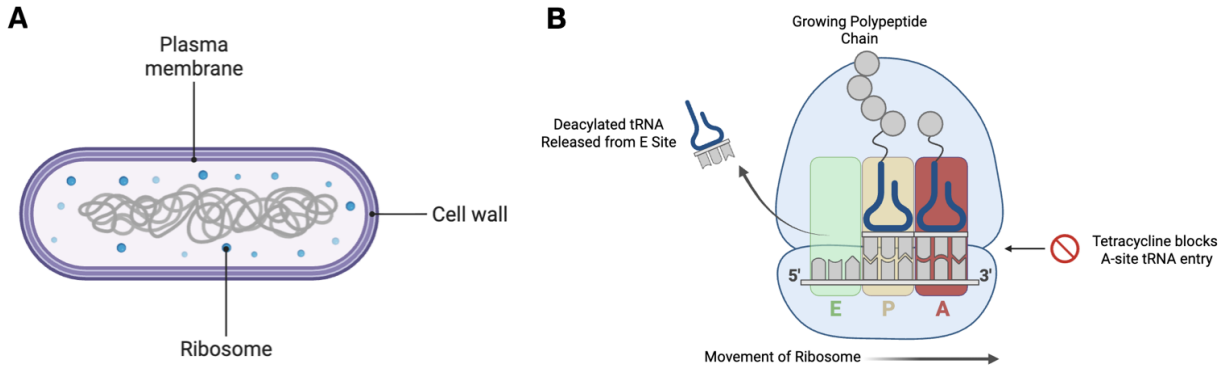


Figure 2.1: Schematic of *E. coli* cellular organization and ribosome-mediated translation. (A) Simplified cell diagram highlighting ribosomes, the primary target of many translation-inhibiting antibiotics, and the cell envelope, which influences uptake and growth dynamics. (B) Translation elongation cycle: the ribosome progresses along mRNA, cycling tRNAs through the A, P, and E sites. Tetracycline blocks aminoacyl-tRNA entry at the A-site, inhibiting elongation. *Created with BioRender.com.*

Recent studies have shown that a cell's metabolic state, for example, whether it is in a high-flux, energy-packed state with rapid biosynthesis or in a slow-growing, energy-restricted state, can strongly influence its susceptibility to antibiotics, such as those that limit protein synthesis (such as chloramphenicol via elongation prevention). Namely, *E. coli* cells with high metabolic energy production (high respiratory activity and ATP generation, though not necessarily fast growth) are more susceptible to cell wall-targeting antibiotics such as penicillin, whereas cells in a low-energy state exhibit increased tolerance [113]. These growth state effects are antibiotic class-specific. Susceptibility to ribosome-targeting antibiotics is highest when cells are actively synthesizing proteins, as these drugs rely on active translation for their efficacy [71]. High ribosome concentration and active protein synthesis flux have been suggested to influence the spatial organization and packing of macromolecules in the cytoplasm, notably under exposure to sub-lethal concentrations of ribosome-targeting antibiotics [229]. Mechanistic models further propose that adaptation to ribosome-targeting antibiotics involves reallocating cellular resources away from growth-enhancing metabolic functions and, under translation inhibition, often increasing ribosome synthesis as guanosine tetraphosphate (ppGpp)-mediated repression is relieved, while at the same time promoting programs like chaperone networks and other ppGpp-controlled processes [76][189][198]. Together, these findings emphasize that the connection between metabolic activity, ribosome abundance, and antibiotic mode of action is a determinant of how *E. coli* responds to ribosome-targeting drugs.

2.2 Bacterial Growth Dynamics

2.2.1 Introduction

Bacterial growth signifies a fundamental biological process, highlighting the capacity of cells to convert nutrients into biomass and reproduce across various environments. This dynamic connection of metabolism, macromolecular synthesis, and resource allocation supports microbial survival and ecological success. Growth dynamics not only determine how populations thrive but also shape bacterial physiology at the cellular level, influencing gene-expression programs, the allocation of the proteome between ribosomal, metabolic, and maintenance proteins, and the induction of protective functions such as chaperones, proteases, and oxidative-stress defences. As such, growth serves as a vital indicator of cellular health and fitness, linking environmental inputs to phenotypic outputs [12][139][189]. Understanding bacterial growth dynamics has extensive implications in microbiology, biotechnology, and medicine. In laboratory and industrial settings, optimizing

growth conditions improves yields of recombinant proteins and metabolites [135]. Clinically and experimentally, the influence of bacterial growth rate on antibiotic susceptibility is not uniform across drug classes. For many reversible ribosome-targeting agents and cell wall antibiotics, fast growing cells are typically more susceptible, whereas slower-growing or dormant cells often display increased tolerance [7]. On the other hand, for some irreversible ribosome-targeting antibiotics, the effect of growth rate on vulnerability is much weaker or can even be absent [71]. Factors such as nutrient availability, temperature, pH, and global regulatory factors, including ppGpp-mediated stringent response, control growth behaviour, emphasizing the requirement for quantitative methods to predict and control bacterial survivability under shifting conditions [76][132][198].

2.2.2 Phases of Bacterial Growth

Bacterial growth in batch cultures frequently follows a reproducible, sigmoidal path known as the bacterial growth curve (see Figure 2.2). This curve is split into four distinct phases: lag, exponential (log), stationary, and death [132]. Each phase mirrors underlying physiological and regulatory adaptations in response to environmental changes and resource availability. While the bacterial growth curve is widely observed across many species, the duration of each phase and the overall shape can change depending on the organism, the nutrient composition of the medium, and environmental conditions such as temperature, pH, oxygen availability, and antibiotic administration. The lag phase signifies a bout of metabolic adjustment as opposed to visible growth. Cells in this phase are metabolically operative, synthesizing enzymes and macromolecules needed for the exploitation of nutrients in a changing environment. Although no considerable increase in cell number is observed, this precursory stage is required for enabling vigorous population expansion. The duration of the lag phase is demonstrated to depend on the initial physiological state of the inoculum and the inherent features of the new growth medium [132]. In rapidly growing *E. coli*, a hindrance between nutrient exposure and DNA replication initiation continues to highlight the temporal complexity of the lag phase [78].

Subsequent to adaptation, cells shift into the exponential phase, where growth is at a constant, maximal rate. Under nutrient-rich and optimized conditions, *E. coli* can double approximately every 20 minutes. This phase is indicated by balanced growth, signifying that cell mass, volume, and macromolecular content increase proportionally. The increase in bacterial cell number density $N(t)$ is well-approximated by an exponential function during balanced growth,

$$N(t) = N_0 e^{\lambda t}, \tag{2.1}$$

where $N(t)$ is the population density at time t, N_0 is the initial population density, and λ is the specific growth rate constant [53][137].

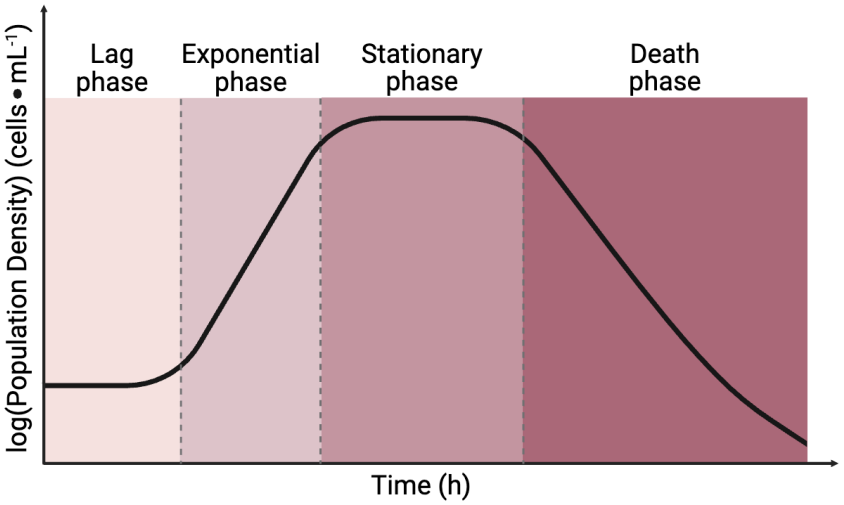


Figure 2.2: The canonical four phases of growth: lag, exponential (log), stationary, and death. Each phase is shown as log(population density) ($\log(\text{cells}\cdot\text{mL}^{-1})$) versus time. These phases highlight changes in resource allocation and physiological state that influence how bacteria respond to environmental changes and antibiotic exposure. Redrawn after Figure 1 from [132]. *Created with BioRender.com.*

Exponential growth holds during early phases when resource limitation and waste accumulation are negligible. As nutrient availability declines and waste materials accumulate, cell division decelerates and the culture enters the stationary phase. During this phase, the rate of cell death approximately equals the rate of division, leading to a stagnant population size. Physiologically, bacteria shift from active biosynthesis to stress-survival functions, inducing defences against oxidative damage, routes for scavenging scarce nutrients, and mechanisms that protect and repair DNA, proteins, and membranes [76][139]. Despite decreased division, cellular processes such as transcription and translation continue at diminished rates. Stationary-phase cells have been shown to remain metabolically active, correcting earlier assumptions that this phase illustrates a dormant state [121]. Prolonged nutrient depletion and byproduct accumulation to a toxic level eventually lead to cell death. In the death phase, the number of viable cells reduces as cell lysis, autolysis, or programmed cell death pathways are carried out. The bacterial growth curve describes the combined effects of cellular biosynthesis, regulation of nutrient utilization, reallocation of

resources toward protective measures under stress, and the population-level consequences of nutrient depletion and waste accumulation. Its ongoing relevance in microbiology stems from its power to combine physiological descriptions with quantitative models to understand microbial behaviour in controlled environments. Synchronized culture experiments have provided time-resolved insights into DNA replication initiation and cell cycle timing, demonstrating that replication remains precisely coordinated during exponential growth but becomes more asynchronous as cells transition to stationary phase [78].

Bacterial growth rate operates as a fundamental criterion of physiological performance, showcasing the integrated output of cellular metabolism, gene expression, and environmental awareness. While exponential growth under balanced conditions provides an idealized reference state, growth behaviour is driven by a range of external and internal factors. These include nutrient composition, temperature, pH, osmotic pressure, oxygen availability, and waste accumulation, all of which harmonize biosynthetic efficiency and impact the ability of cells to divide and prosper [115][139]. Under nutrient-packed and constant conditions, bacterial populations can reach balanced growth, where all cellular units, like DNA, RNA, proteins, and lipids, accumulate at relatively unchanged rates. During this phase, cells exhibit highly regulated phenotypes, with growth rate firmly coupled to ribosomal content. This approach reflects a wider regulatory principle, growth rate modulation in bacteria predominantly occurs through changes in ribosome concentration rather than adjustments in ribosome activity. Evolutionarily, this strategy is advantageous because ribosome activity is chemically constrained, whereas ribosome abundance can be tuned rapidly and efficiently through rRNA transcription. Modulating concentration also preserves translational fidelity and maintains tight coupling between metabolism and protein synthesis, allowing cells to adjust growth rate flexibly across varying nutrient conditions [139]. Apart from nutrient quality, environmental pressure such as heat shock, osmotic stress, and oxidative damage can interrupt balanced growth and trigger complete transcriptional responses. Pathways like catabolite repression and the stringent response alter gene expression variants to reallocate resources toward mitigating stress or energy preservation. For instance, during amino-acid starvation or entry into stationary phase, cells suppress ribosomal RNA synthesis and upregulate genes involved in amino-acid formation [167]. These transitions decrease metabolic expenditure and aid persistence during unfavourable conditions [115][139].

Physical conditions such as temperature, pressure, and pH strongly impact bacterial growth rate by affecting enzymatic activity, macromolecular stability, and membrane fluidity. Temperature, particularly, has a strong and predictable effect. Growth rate increases with temperature up to a specific optimum unique to an organism, beyond which proteins depreciate and membrane strength is compromised. Each species is defined by a

range of primary temperatures (minimum, optimum, and maximum) that set forth its viable thermal window [115]. In addition, pressure can either hinder or augment microbial activity depending on the organism's habitat. While most laboratory model organisms are pressure-sensitive, piezophilic bacteria located in deep-sea environments show elevated growth rates at high hydrostatic pressures, often exhibiting altered membrane composition and protein balance in preparation for these extreme conditions [140]. pH applies its effects notably through ionization of cellular components and interruption of proton gradients necessary for ATP synthesis. Most neutrophilic bacteria ensure internal pH homeostasis near neutrality even when placed in acidic or alkaline environments, but extreme shifts from this range weaken nutrient transport, enzyme function, and energy metabolism, leading to diminished or arrested growth [115][140].

Experimental setups such as batch and continuous culture continue to illustrate the dependence of growth rate on the environment. In batch cultures, exponential growth is transient, often stopped by nutrient depletion or toxin accumulation. Cells then transition into stationary phase, where population density stays stable, but metabolic activity may carry on at reduced levels. Conversely, chemostat cultures maintain cells in an outlined growth-limited state by managing nutrient input and waste removal, enabling accurate decoupling of growth rate from population size. These systems have proven critical for isolating the influence of specific nutrients or growth rates on macromolecular elements, enzyme activity, and gene regulation [115]. At the single-cell level, growth rate remains incredibly robust, even across multitudes of generations [139]. Microfluidic time-lapse experiments tracking individual *E. coli* cells revealed stable elongation rates and constant protein production under steady conditions. Although cell-to-cell variance and transient fluctuations persist, they are often buffered by intrinsic feedback mechanisms. Importantly, such studies give no evidence of aging-related growth deceleration in bacteria under favourable conditions. Instead, bacterial growth provides a form of physiological homeostasis, where the protein synthesis rate and elongation correct across divisions to ensure population-level consistency [220].

2.2.3 Quantitative Measures of Growth

Optical density (OD) is a widely used method for monitoring bacterial growth. When light is shone through a culture, it is scattered by the cells, and the spectrophotometer records the apparent absorbance, typically at 600 nm (OD_{600}). OD is the concentration of light-scattering particles, corresponding to the number of cells per unit volume. Within a limited range of low to moderate cell densities, OD increases approximately linearly with cell concentration, allowing estimation of the specific growth rate during the exponential

phase. At higher cell concentrations, multiple scattering and instrument geometry cause departures from linearity. Light scattered by one cell can be redirected into the detector by others, artificially inflating or flattening the OD signal. These deviations must be corrected using calibration curves specific to the spectrophotometer and growth conditions [96]. Calibration is essential whenever OD is to be related to actual cell numbers or biomass and must be redone if instrument geometry changes (for example, after replacing phototubes or switching cuvette types).

During exponential growth, bacterial cells enlarge in mass and replicate at regular intervals, distinguished by the specific growth rate λ, defined as

$$\lambda = \frac{1}{X}\frac{dX}{dt},$$

where X denotes biomass, OD, or cell number, depending on the experimental measure used. Growth rate λ is typically expressed in units of reciprocal time ($1/\text{hours}$, h^{-1}). The corresponding doubling time, or generation time τ_d (units of time, hours h), is the time necessary for the population to double and is given by

$$\tau_d = \frac{\ln(2)}{\lambda}.$$

Experimentally, these variables are estimated by measuring OD at standard intervals during exponential growth. Plotting the natural logarithm of OD against time yields a linear regime, the slope of which corresponds to λ. Under balanced exponential growth, the synthesis of major macromolecular components is coordinated so that cell composition remains steady while the population expands [26]. RNA content, particularly ribosomal RNA, rises sharply with the specific growth rate λ, providing the translational capacity required for rapid growth. Because faster-growing cells are larger, their total protein mass per cell increases with growth rate even though the protein concentration remains approximately constant [184][192]. In contrast, DNA content increases more flexibly with growth rate, highlighting the replication strategy described by the Cooper–Helmstetter model, in which multifork replication can occur at high growth rates [41]. These coordinated changes in macromolecular composition underpin the quantitative coupling between cell physiology and population-level growth kinetics.

2.2.4 Bacterial Growth Environments: Emphasis on Batch Culture

Bacteria can be cultivated in a variety of environments, ranging from closed systems such as batch cultures to continuous systems such as chemostats [132][147]. Batch cul-

ture is a closed system in which all nutrients are supplied at the start of growth. As cells consume nutrients and produce byproducts, the culture progresses through the characteristic lag, exponential, and stationary phases (Subsection 2.2.2), reflecting shifts in metabolism as nutrient levels decrease and waste products build up [139]. Although batch cultures are not steady-state systems, they are simple, reproducible, and closely copy natural environments where resources are intermittently available [162]. Batch culture remains the standard for physiological studies and for antibiotic-response studies, particularly for investigating how growth rate and metabolic state influence susceptibility to ribosome-targeting antibiotics such as tetracycline (which blocks aminoacyl-tRNA binding at the A-site of the 30S subunit) and chloramphenicol (which inhibits peptide bond formation at the 50S subunit) [71][189]. This experimental context pins the present work's focus on growth-rate-dependent responses to transient antibiotic stress.

2.2.5 Mathematical & Computational Models of Bacterial Growth

Phenomenological curve fits (such as classical logistic or Monod-style summaries) can be useful for quick description but lack mechanistic detail. In these approaches, the emphasis is on models that connect molecular processes to growth phenotypes. Structured and multi-scale models merge information across biological layers, from molecular interactions to metabolic control, offering a mechanistic view into how gene expression, enzymatic activity, and environmental signaling jointly shape bacterial physiology and growth behaviour. A coarse-grained model of *E. coli* transcriptional dynamics quantitatively links rRNA operon activity to ribosome synthesis, gene dosage, and growth rate, capturing constraints such as RNA polymerase availability, promoter affinities, and competition among rRNA operons [205]. Metabolic flux-based models operate on intracellular metabolite dynamics and network topology, illustrating adaptation to nutrient changes via redistribution of flux through central pathways and feedback between metabolites and regulators (for example, transitions between glycolysis and gluconeogenesis) [104]. Multi-scale models connect gene expression, proteome partitioning, and metabolic output, incorporating growth laws, genome-scale stoichiometry, and protein cost to simulate whole-cell responses. Under slow growth, proteome allocation shifts toward stress functions while translational capacity declines. Feedbacks from translation to transcription are accommodated to capture reciprocal control across time scales [47]. Modern work layers stochasticity and host context onto these frameworks. Hybrid ordinary differential equation (ODE)–stochastic models examine antibiotic stress with immune-system dynamics, revealing how variability in clearance or dosing timing can alter survival trajectories [159]. Stochastic single-cell models (such as Gillespie-based) capture heterogeneity, rare mutational events, and per-

sistence via phenotypic switching that deterministic models obscure [119]. Together, these mechanistic and probabilistic approaches extend beyond curve-fitting to provide predictive insight into physiology, evolution, and antimicrobial response.

2.3 Bacterial Physiology

Bacterial physiology encompasses the study of cellular processes that guide growth, metabolism, and adaptation to environmental changes. As single-celled organisms, bacteria are renowned for their ability to sense and respond quickly to shifts in nutrient availability, stress, and physical conditions. This physiological flexibility supports their success in diverse ecological niches and is a vital determinant of their growth dynamics, survival strategies, and interactions with antimicrobials. At its core, bacterial physiology displays an intricate balance between biosynthetic requirements and the allocation of limited cellular resources. Foundational studies have shown that bacterial growth is characterized by coordinated changes in macromolecular makeup, including DNA, RNA, proteins, and lipids, which are strongly linked to specific growth rates [141][184]. These adjustments help the cell's ability to maintain homeostasis across various growth phases, from rapid exponential growth to stationary and dormant conditions [30][132]. Comprehending these physiological principles provides necessary context for studying how bacteria adjust to stressors like nutrient depletion or antibiotic exposure. This foundational context promotes exploring bacterial growth physiology in detail.

2.3.1 Growth Physiology

Bacterial growth physiology constitutes the essence of microbial life, describing how cells synchronize molecular processes to sustain proliferation across varied environments. This area of study connects molecular biology, systems biology, and ecological microbiology, emphasizing how bacteria stabilize biosynthetic capacity, metabolic flexibility, and environmental recognition. Classical studies establish bacterial growth as a function of nutrient availability, with populations advancing through lag, exponential, stationary, and death phases. Each phase shows distinct physiological states and adaptive strategies that influence macromolecular composition and cellular activity [132][183]. During exponential growth, cells achieve balanced growth at which point DNA, RNA, proteins, and lipids all increase proportionally. This phase supports maximal division rates and is characterized by high ribosome content, allowing rapid protein synthesis [91][141]. Studies indicate a linear relationship between RNA content, particularly ribosomal RNA, and specific growth

rate, solidifying ribosomes as critical determinants of bacterial reproduction [26][184][189]. Further research exposed the regulation of ribosome synthesis, showing how growth-rate-dependent controls and feedback loops maintain stability [145][146].

2.3.2 "Growth Laws"

Growth laws are a central organizing principle of bacterial physiology, encapsulating the quantitative relationships between macromolecular composition, ribosome allocation, and growth rate. Early experimental work showed that bacterial macromolecular composition, particularly the RNA/protein ratio, increases approximately linearly with the specific growth rate λ, showing increased investment in translational capacity to maintain rapid biosynthesis [141][184][189]. Because the majority of cellular RNA in *E. coli* is ribosomal RNA, the RNA/protein ratio serves as a suitable proxy for ribosome content, which is a vital determinant of the cell's protein synthesis capacity [26][189]. Two verifiable regimes have been identified. In nutrient-limited growth, where metabolic capacity is constrained by the availability or quality of nutrients, cells devote a larger portion of their proteome to metabolic enzymes. As nutrient quality improves, a greater proteome fraction is allocated to ribosomes, allowing faster protein synthesis and thus an increase in growth rate. In translation-limited growth, where protein synthesis is inhibited by ribosome-targeting antibiotics such as tetracycline or chloramphenicol, or by slow-translation mutations, growth rate decreases because the pool of actively elongating ribosomes is reduced even though nutrients remain available. In this regime, cells often compensate by increasing ribosome content, but the slower peptide-elongation rate per ribosome constrains overall protein production and thus limits growth. These two empirical "growth laws" emphasize ribosomes as both the driver and the limiting factor for bacterial proliferation. They show that growth is determined not only by external nutrient supply but also by the efficiency of the translational capacity. The growth law framework provides a biological foundation for later quantitative models that link ribosome allocation, nutrient quality, and growth-rate-dependent susceptibility to ribosome-targeting antibiotics. The mathematical formulation of these relationships, including their linear slopes and geometric interpretation, is presented in Chapter 3 (see the discussion in Section 3.1 and the accompanying Figure 3.1).

2.3.3 Proteome Partitioning

Proteome partitioning is best understood in the context of the physiological constraints that shape protein expression. A central observation is that, across balanced growth conditions, the cytoplasmic protein concentration (protein density) remains approximately

constant, varying by less than ∼10% in *E. coli*, because cell volume scales proportionally with biomass production [184][189][192]. Because the total protein pool is effectively fixed, the protein mass fraction of any sector shows both its share of ribosomal synthesis capacity and its relative concentration. A major consequence of this constraint is that increasing the abundance of one sector forcibly reduces the resources available for others, giving rise to largely anticorrelated behaviour among proteome sectors. This viewpoint allows the bacterial proteome to be coarse-grained into a few broad functional sectors that highlight most of the physiology (see Figure 2.3). As the ribosomal sector expands to support rapid growth in nutrient-rich conditions, other sectors, like those involved in central metabolism, stress defence, or envelope maintenance, reduce. Oppositely, under nutrient limitation or stress, ribosomal mass fraction decreases as other sectors expand. This principle means that any large-scale shifts, such as inhibition of one sector by a ribosome-targeting antibiotic, indirectly remodels the others due to the protein density constraint [12][192][232].

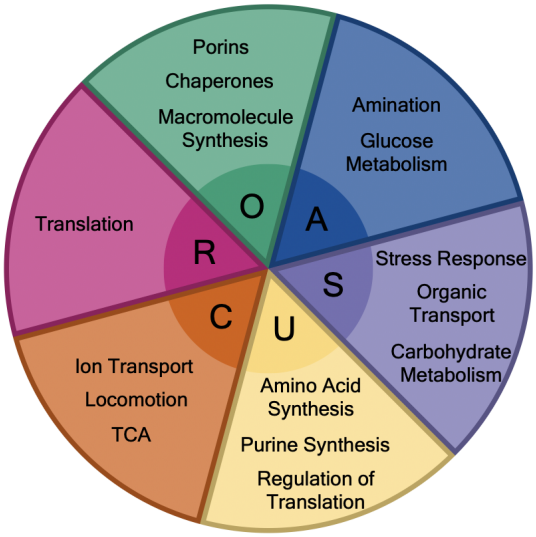


Figure 2.3: Coarse-grained partitioning of the *E. coli* proteome into major functional sectors. Because total protein density remains approximately constant, each mass fraction reflects its share of cellular capacity. Expansion of one sector necessarily reduces others, producing largely negative correlations. The schematic illustrates competitive allocation among translation machinery (R), core metabolism, including energy-intensive functions such as ion transport, the TCA cycle, and locomotion (C), amino-acid biosynthesis (U), envelope and stress-response functions (O, S), and other functions such as amination pathways involved in nitrogen assimilation (A). *Redrawn from* [136] *under the terms of the Creative Commons CC BY 4.0 license.*

Quantitative proteomics and modeling have shown that bacterial growth physiology can be expressed in terms of these proteome sectors, many of which vary linearly with growth rate [12][189][192]. This framework shows a fundamental resource allocation trade-off. Under nutrient-rich, rapid-growth conditions, ribosomal proteins dominate the proteome to maximize translational capacity, while under nutrient limitation or stress, allocation shifts toward metabolic, protective, or maintenance functions [136][207][231]. Importantly, slow-growing cells are not only scaled-down versions of fast-growing cells, they often hold a reserve of inactive ribosomes that can be quickly mobilized during nutrient upshifts, allowing quick adaptation in fluctuating environments [44][97]. By focusing on protein mass fractions and their complementary, often inverse, behaviour, this framework clarifies how proteome allocation constraints controls cellular adaptation. In particular, under nutrient limitation, the ribosomal sector shrinks while the metabolic sector expands to improve nutrient uptake and processing. On the other hand, under translation inhibition by antibiotics such as tetracycline, cells increase their ribosomal content in an attempt to compensate for reduced translational efficiency, reallocating resources away from metabolic functions. These reciprocal shifts illustrate the classic growth law trade-off between sectors [26][184][189]. These principles provide the conceptual basis for linking proteome dynamics to protein synthesis antibiotic susceptibility and for interpreting resource reallocation patterns.

Molecular regulatory networks further modulate these allocations. The alarmone ppGpp acts as a principal regulator of ribosome production, down-regulating translational mechanisms under stress. For example, nutrient limitation shifts resources toward metabolic uptake systems, or translation inhibition by antibiotics such as tetracycline drives increased ribosome synthesis at the expense of other proteome sectors, thereby redirecting resources toward the functions most needed for survival [76][198]. Coordination between RNA polymerase activity and ribosome production helps establish balanced expression of ribosome-associated growth machinery and protective stress-response factors such as chaperones, proteases, and oxidative-stress defence enzymes [125][178]. Post-translational machinery such as targeted protein degradation and chaperone-mediated folding aid in removing misfolded or surplus proteins and maintaining protein-quality homeostasis [206][226]. The concept of a "proteome reserve", which is an uncommitted pool of cellular capacity that can be mobilized during environmental shifts, has been proposed to explain the quick proteome remodeling observed in dynamic settings [133][150][214]. Such flexibility improves the robustness of bacterial physiology, enabling cells to cushion fluctuations in nutrient availability, antibiotic exposure, and translational demands [14][233]. Understanding these constraints has practical implications for biotechnology and synthetic biology, where excessive allocation to unnecessary proteins can interupt core physiological func-

tions and slow growth [23][40]. Incorporating knowledge of resource allocation limits into the blueprints of expression circuits and metabolic interventions has been shown to improve growth and productivity of engineered strains [57][157]. Overall, proteome partitioning provides a systems-level framework for understanding how *E. coli* and other bacteria modulate growth optimization and stress resilience. By integrating insights from high-throughput proteomics, quantitative modeling, and molecular regulation, this concept strengthens the interpretation of growth-rate-dependent physiology and serves as a bridge to understanding antibiotic-induced growth adjustments.

2.4 Antibiotics and their Cellular Targets

Antibiotics continue to be one of the most transformative innovations in medicine, crucially altering our ability to treat bacterial infections and control the spread of disease. These compounds target necessary bacterial processes, exploiting differences between prokaryotic and eukaryotic cells to selectively prevent microbial growth. Commonly, antibiotics have been classified based on their molecular targets, including cell wall synthesis, protein synthesis, DNA replication, and membrane strength [106][153]. Their development and clinical applications have been informed by decades of chemical and microbiological studies, which spells out mechanisms of action and resistance pathways. The rise of multidrug-resistant bacteria emphasizes the urgency of understanding antibiotic modes of action at both molecular and systems levels [101][223]. Advances in omics technology and biophysical modeling have contributed to a prolonged understanding of how antibiotics interact synergistically or antagonistically within the cellular environment [89][199]. This knowledge is essential for developing novel drugs and optimizing combination therapies that minimize resistance evolution.

2.4.1 Overview of Antibiotics and Mechanisms

Antibiotics employ their effects by disrupting vital bacterial functions, with many classes targeting macromolecular pathways. A major category includes inhibitors of protein synthesis, which bind to the bacterial ribosome and disrupt translation. Aminoglycosides, for example, cause misreading of mRNA, leading to defective proteins that can disrupt membrane durability and generate lethal effects [46][127]. Tetracyclines and macrolides halt elongation by blocking tRNA binding or preventing translocation, respectively [124][227]. These interactions utilize structural features unique to the prokaryotic ribosome, permitting selectivity over eukaryotic translation mechanisms [164]. An additional critical target

is cell wall synthesis. β-lactams, such as penicillins and cephalosporins, inhibit penicillin-binding proteins involved in peptidoglycan cross-linking, eventually compromising cell wall integrity and causing lysis [42][153]. Glycopeptides like vancomycin bind to peptidoglycan precursors, preventing polymerization and cross-linking.

DNA replication and transcription are targeted by quinolones and rifamycins, respectively. Quinolones hinder DNA gyrase and topoisomerase IV, enzymes required for supercoiling and segregation of bacterial chromosomes [106]. Rifamycins bind to RNA polymerase, obstructing transcription initiation. Finally, agents like polymyxins destabilize the bacterial outer membrane by interacting with lipopolysaccharides, a mechanism notably effective against Gram-negative microbes [153]. Recent studies have underlined how sub-lethal antibiotic exposures can induce stress responses (RecA, repair enzymes for example) and metabolic shifts that stimulate persistence and resistance [101]. Systems-level models suggest that antibiotics do not act in isolated incidents but within a complex cellular network where their effects can boost or impede one another [89]. This complexity highlights the need for a holistic understanding of antibiotic implementation to inform rational drug design and therapeutic strategies. Combined, these works provide a basis for exploring the cellular targets of antibiotics and their wider impact on bacterial physiology. They also pave the way for examining how resistance emerges and how combination therapies can be customized to circumvent them [199][223].

2.4.2 Major Antibiotic Targets

DNA Replication

Antibiotics that target bacterial DNA interrupt critical cellular processes such as replication, transcription, and repair, which leads to bacteriostasis or cell death. Among the most commonly studied are fluoroquinolones, including ciprofloxacin, which inhibit bacterial DNA topoisomerases like gyrase and topoisomerase IV. These enzymes play vital roles in alleviating DNA supercoiling and undoing knots that develop during replication and transcription. By stabilizing the transient enzyme-DNA cleavage complexes, fluoroquinolones confine these enzymes in a state that causes DNA double-strand breaks (DSBs), stopping replication fork progression, leading to irreversible chromosomal damage [80][148]. The action of fluoroquinolones triggers not only direct DNA damage but other general cellular stress responses (such as nucleotide enzymes, strand-exchange proteins). Accumulation of DSBs initiates the bacterial SOS response, a global regulatory system that induces DNA repair enzymes and stimulates cell cycle arrest. While this response can allow some cells to survive sub-lethal damage, it also increases error-prone repair, increasing mutation rates

and possibly accelerating resistance evolution [80]. Ciprofloxacin is notable for its delayed bactericidal activity, where treated cells typically continue elongation and DNA synthesis transiently before replication fork collapse leads to filamentation and lysis [54][148].

Biophysical models, such as the roadblock-and-kill mechanism, offer views into how poisoned gyrases act as physical barriers to the replication procedure. These models account for both replication-dependent and replication-independent DNA breakage, illustrating the importance of enzyme kinetics and DNA topology in determining antibiotic efficacy [148]. Experimental observations support these models, showing that gyrase inhibition can lead to lethal chromosomal fragmentation even in non-replicating cells. Beyond fluoroquinolones, other DNA-targeting antibiotics operate through distinct molecular strategies. Rifamycins, for instance, bind to the β-subunit of RNA polymerase, blocking the initiation of transcription and depleting critical mRNAs required for bacterial growth. Mitomycin C acts as a DNA crosslinker, forming covalent bonds between complementary DNA strands and thus preventing the separation needed for replication and transcription. Additional agents such as novobiocin prevent DNA gyrase activity allosterically, further demonstrating the variety of strategies to exploit bacterial nucleic acid metabolism [54]. Jointly, DNA-targeting antibiotics compromise the integrity of the bacterial genome and disturb gene expression, triggering immediate physiological apprehension and long-term consequences for population dynamics. These agents show the vulnerability of bacterial genetic systems and the likelihood for leveraging these weaknesses in the development of new cures for infection.

Protein Synthesis

Antibiotics targeting bacterial protein synthesis primarily target weaknesses in the ribosome, the molecule responsible for translating mRNA into polypeptides. The bacterial ribosome consists of two subunits, the small (30S) and large (50S), each containing unique functional centers critical for translation. Numerous antibiotic classes obstruct the ribosome's activities, influencing initiation, elongation, and termination phases of protein synthesis [124][227]. Tetracyclines, for instance, bind to the 30S subunit (see Figure 2.4) and prevent the accommodation of aminoacyl-tRNA at the A site, blocking peptide chain elongation [28][65]. Structural studies have shown how tetracyclines' binding site covers the tRNA path, physically inhibiting incoming tRNAs [164]. Ribosome-tetracycline interactions further show dynamic shifts in binding affinity influenced by ribosomal conformational changes [212]. Aminoglycosides, another major class, bind near the decoding center of the 16S rRNA inside the 30S subunit and causes misreading of mRNA codons. This misreading yields the incorporation of incorrect amino acids and production of useless or toxic proteins, leading to cell death [28][46]. Apart from translational errors, aminoglyco-

sides also induce membrane disruption as secondary effects, intensifying their bactericidal activity [228]. On the 50S subunit, macrolides, chloramphenicol, and lincosamides act with the peptidyl transferase center (PTC). Chloramphenicol obstructs peptide bond formation by binding to the PTC and challenges the aminoacyl moiety of incoming tRNAs. Semi-synthetic chloramphenicol analogs have been designed to improve binding affinity and reduce susceptibility to resistance mechanisms [208].

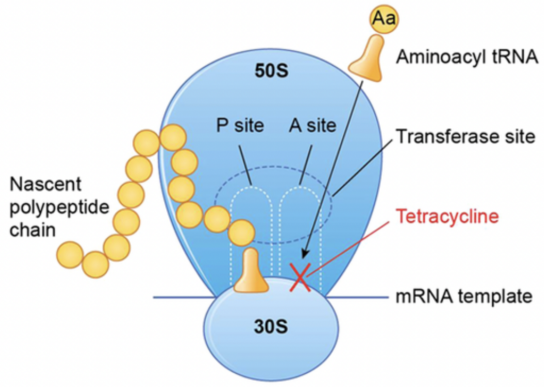


Figure 2.4: Mechanism of tetracycline inhibition of bacterial translation. Tetracycline binds to the 30S ribosomal subunit and blocks the A site, preventing aminoacyl-tRNA from accessing the mRNA template and halting elongation of the nascent polypeptide chain. *Reproduced from* [68] *under the terms of the Creative Commons CC BY 4.0 license.*

Macrolides such as erythromycin bind inside the ribosomal exit tunnel, hampering elongating nascent chains in a context-specific manner depending on the peptide sequence [230][235]. Latest structural studies have described how macrolide-induced stalling can be controlled by nascent peptide conformations [172]. In addition to closing off translation directly, several antibiotics disturb ribosome biogenesis. Oxazolidinones and pleuromutilins prevent subunit assembly by binding to immature ribosomal precursors, leading to collection of incomplete ribosomal particles and decreased numbers of functional ribosomes [35][36][116]. Antibiotic-induced ribosomal assembly defects have been associated to extensive changes in protein expression profiles, showing the interconnectedness of translation and bacterial physiology [195]. Aminoacyl-tRNA synthetases (aaRS), essential for charging tRNAs with their corresponding amino acids, are also antibiotic targets. Inhibitors of aaRS delay translational fidelity and compromise total protein synthesis [110]. Kinetic research of drug-ribosome interactions report that residence time on the ribosome is vital for determining antibiotic strength and resistance development [203]. Resistance mechanisms

to protein synthesis inhibitors are varied, including target site mutations, methylation of rRNA residues, efflux pumps, and enzymatic drug modifications. For example, tetracycline resistance often involves mutations in 16S rRNA or possession of ribosomal protection proteins such as $Tet(M)$, which removes tetracyclines from their binding site [179]. Similarly, methylation of 23S rRNA by Erm methyltransferases confers resistance to macrolides and lincosamides [228]. Altogether, antibiotics that target protein synthesis disrupt one of the most crucial and resource-intensive processes in bacteria. Their multifaceted actions, from preventing peptide elongation to ending ribosome biogenesis and aminoacyl-tRNA charging, highlight the centrality of the ribosome in bacterial survivability and make it a focal point in antibiotic development.

Cell Wall Synthesis and Membrane Disruptors

Antibiotics that target bacterial cell walls and membranes take advantage of critical vulnerabilities in the structural integrity and balance of bacterial cells. Many of these compounds, such as β-lactams and glycopeptides, act by stopping peptidoglycan synthesis, the process for maintaining cell shape and combatting osmotic pressure. β-lactam antibiotics, including penicillins and cephalosporins, connect to penicillin-binding proteins (PBPs), which are transpeptidases involved in the cross-linking of peptidoglycan strands. By deactivating PBPs, these drugs weaken the cell wall and cause cell death due to osmotic stress [54]. Glycopeptides like vancomycin, bind directly to the D-Ala-D-Ala termini of peptidoglycan precursors, preventing their mixing into the growing cell wall. Apart from the cell wall, antibiotics such as polymyxins directly reduce the integrity of bacterial membranes. Polymyxin B and E (colistin) interact with lipopolysaccharides and phospholipids in the outer membrane of Gram-negative bacteria, leading to increased flux and cell death. This mode of action makes them stronger against multi-drug resistant organisms, though their use is often restricted due to nephrotoxicity [59]. Membrane-targeting antibiotics can also inhibit lipid synthesis, such as daptomycin, which integrates into the cytoplasmic membrane of Gram-positive bacteria and causes quick depolarization.

Recent work has illustrated how these antibiotics not only kill bacteria but also prompt distinct morphological changes [43][54][202]. Particularly, cell wall synthesis inhibitors typically lead to spheroplast formation, while membrane disruptors can cause cell shrinkage or lysis. Quantitative analyses have shown that these treatments affect cellular parameters like surface area, volume, and aspect ratio, highlighting the disruption of structural homeostasis [43]. Furthermore, multidrug efflux pumps contribute to intrinsic and gained resistance to these classes of antibiotics. By actively emitting toxic compounds from the cell, efflux systems decrease intracellular drug concentrations and delay the onset of mem-

brane or cell wall damage. These pumps are normalized by complex networks responding to environmental and physiological cues, making them difficult targets for therapeutic intervention [202]. Combined, cell wall and membrane disruptors represent a critical arm against bacterial infections, particularly when targeting pathogens with robust ribosomal and DNA repair defence tactics. However, their efficacy is threatened by the development of resistance mechanisms, necessitating continued efforts to understand and counteract bacterial adaptation.

2.5 Proteomic Response to Stress

Bacteria routinely face environmental challenges such as nutrient limitation and antibiotic exposure that demand quick, coordinated adaptation. Key to this adaptation is proteome remodeling, in which cells shift biosynthetic capacity away from growth-associated processes, particularly ribosome synthesis, toward maintenance and survival. A classic example is the stringent response, mediated by ppGpp, which suppresses ribosomal RNA transcription and translation factors while up-regulating genes for amino-acid synthesis, nutrient scavenging, protein quality control, and oxidative-stress defence [76][167][198]. Proteomic analyses show lower ribosomal abundance alongside higher chaperones, ATP-dependent proteases such as Lon and ClpXP, and envelope-stress proteins that preserve structural integrity during starvation [63][222]. These reallocation strategies conserve energy and maintain a proteome reserve that supports rapid recovery once nutrients become available [66][133]. Although ppGpp upregulates oxidative-stress defences, this does not imply that cells growing exponentially in poor media are intrinsically more protected against oxidative stress. During slow but nutrient-sufficient growth on minimal media, ppGpp levels remain low, and the stringent response is not strongly activated, the proteome is simply rebalanced toward nutrient acquisition rather than stress protection. In contrast, true starvation induces high ppGpp accumulation and a qualitatively different physiological state in which oxidative-stress defences, protein quality control systems, and global metabolic downshifts are strongly expressed. Thus, slow growth on minimal media represents a balanced, nutrient-limited state, whereas starvation corresponds to an active stress-response program with different regulatory and proteomic signatures.

Translation-targeting antibiotics such as tetracycline and chloramphenicol trigger a related but distinct remodeling. By inhibiting peptide elongation, they decrease effective translational capacity and slow growth even in nutrient-rich conditions. Sub-lethal exposure causes compensatory upregulation of chaperones, folding catalysts, efflux pumps, and other stress response factors, while ribosomal protein synthesis is upregulated, as

cells attempt to compensate for reduced elongation rates [36][123][199]. The stringent response again redirects transcription from ribosomal promoters to stress response and metabolic pathways that maintain energy homeostasis [76][177][219]. High-resolution proteomics highlight that these reallocations differ by antibiotic class, reflecting whether the primary target is ribosomes, the cell wall or membrane, or DNA [223][228]. Together, these stress-driven reallocations showcase the resource allocation trade-offs at the center of bacterial growth physiology. Under nutrient limitation, a larger proteome fraction supports nutrient foraging and stress pathways. Under translation inhibition, cells upregulated rRNA and ribosomal protein synthesis, increasing ribosome content. However, slower elongation per ribosome limits growth despite this compensatory allocation. In both cases, survival requires prioritizing protecting survivability over biomass accumulation, a trade-off that connects directly to the growth law framework and sets the stage for the modeling approaches developed in the following chapters.

Chapter 3

Mathematical Background

3.1 Foundational Models and Their Limitations

"Growth laws", simple empirical relationships that link ribosome content and gene expression to growth rate, provide a quantitative framework for understanding how bacterial physiology constrains protein synthesis. Under nutrient-limited or translation-inhibited conditions, the ribosomal mass fraction r (often measured as the RNA/protein ratio) correlates linearly with the bacterial growth rate λ [189]. In *E. coli*, most of the RNA consists of rRNA assembled into ribosomes. Because approximately 85-90% of total cellular RNA is ribosomal RNA (rRNA) [140][189], and ribosomes are composed of rRNA and ribosomal proteins in a nearly fixed stoichiometric ratio of about 2:1 (RNA:protein by mass), the RNA/protein ratio serves as a reliable proxy for ribosome abundance and the ribosomal mass fraction. This proportionality holds across various nutrient and antibiotic conditions since differences in growth rate primarily alter the number of ribosomes synthesized, while the rRNA–protein composition of each ribosome remains constant (the Supplementary Information of [189] indicates that the mass ratio between ribosomal RNA and protein yields an approximately constant conversion factor of 0.76 μg protein per μg RNA, confirming that RNA/protein scales directly with ribosome content). Understanding how growth physiology affects gene expression thus requires assessing how cells allocate resources to ribosome synthesis at different growth rates. For exponentially growing *E. coli*, this relationship can be written as

$$r = r_{\min} + \frac{\lambda}{\kappa_T}, \tag{3.1}$$

where the minimum ribosomal mass fraction $r_{\min}$ is the intercept and translational capacity κ_T is the inverse slope (see Figure 3.1, brown arrow). The parameter κ_T is treated empirically as a proportional link between ribosome allocation and achievable growth rate. This correlation has been validated across multiple *E. coli* strains growing in nutrient-rich to moderately poor media.

Translation can also be gradually limited by sub-lethal concentrations of translation-inhibiting antibiotics such as tetracycline, which binds to the 30S ribosomal subunit, blocking binding of aminoacyl tRNA. Under these conditions, a second linear relationship between the ribosomal mass fraction r and the specific growth rate λ is observed [189]. This is expressed as

$$r = r_{\max} - \frac{\lambda}{\kappa_N}, \tag{3.2}$$

where the maximal ribosomal mass fraction $r_{\max}$ is the intercept and the nutritional capacity κ_N is the inverse slope (see Figure 3.1, maroon arrow). This linear dependence describes the translation-limited regime, in which antibiotics reduce elongation efficiency but cells continue to synthesize ribosomes. The parameter κ_N correlates with the growth rate achieved in drug-free conditions and represents the nutritional capacity of the cell [189]. More specifically, κ_N describes the lumped catalytic efficiency of the metabolic enzymes responsible for supplying amino acids and other precursors required for protein synthesis. In this way, nutrient limitation reduces nutritional capacity κ_N by lowering either the availability of substrates or the activity of metabolic transporters, thus constraining the flux of precursors to the translational machinery [190]. Although κ_N is defined through amino acid supply, it implicitly reflects the cell's underlying energy-generation strategy. Carbon sources that support efficient respiration provide higher energetic yield per substrate molecule and therefore enable greater metabolic throughput, whereas fermentative conditions limit precursor supply and reduce the effective κ_N. As a result, nutritional capacity κ_N captures the effective productivity of the metabolic sector of the proteome, linking nutrient quality to the achievable steady-state growth rate. Increasing ribosomal mass fraction r during translation inhibition demonstrates a compensatory response to reduced translational capacity, driven by alleviation of ppGpp-mediated repression of rRNA synthesis in response to intracellular amino acid accumulation [167]. Because the maximal ribosomal mass fraction $r_{\max}$ represents the upper bound of the RNA/protein ratio as translational efficiency approaches zero, its weak dependence on nutrient quality indicates a shared physiological limit for ribosome synthesis [189]. Together, these two growth regimes, nutrient limitation and translation inhibition, define a quantitative framework linking ribosome allocation, growth rate, and nutrient quality.

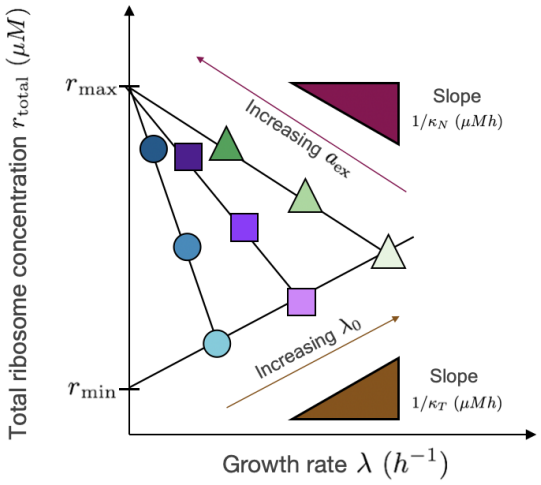


Figure 3.1: Linear constraints between ribosome concentration and growth rate. In balanced exponential growth, ribosomal mass fraction (RNA/protein ratio) increases linearly with growth rate. The slope reflects the inverse translational capacity (brown arrow). Under translation inhibition, a second linear branch appears with slope set by inverse nutritional capacity (maroon arrow). Nutrient types are indicated by marker shape (circles, squares, triangles, ordered by increasing drug-free growth rate λ_0), and darker shades of each shape denote higher antibiotic concentrations. Together, these relations illustrate how growth rate constrains gene expression and proteome allocation. See Figure 2A of [189].

Building on these empirical growth-law relationships, ribosome-targeting antibiotics act by binding to specific sites on the ribosome and inhibiting distinct stages of translation, with differing reversibility and physiological effect. Irreversible inhibitors such as streptomycin and kanamycin bind the 30S subunit and cause misreading and cell death, whereas reversible inhibitors such as tetracycline and chloramphenicol transiently block tRNA binding or peptide elongation on the 30S or 50S subunits. Because ribosome abundance and translational activity depend on the growth rate λ, the physiological state of the cell directly impacts antibiotic susceptibility. These dependencies are formalized in a dynamical model (3.3) (schematized in Figure 3.2) that incorporates membrane transport, reversible ribosome binding, and feedback between intracellular antibiotic concentration and growth inhibition

$$\begin{aligned} \dot{a} &= -\lambda a + f(r_u, r_b, a) + J(a_{\text{ex}}, a), \\ \dot{r_u} &= -\lambda r_u + f(r_u, r_b, a) + s(\lambda), \\ \dot{r_b} &= -\lambda r_b - f(r_u, r_b, a), \end{aligned} \tag{3.3}$$

where a is the intracellular antibiotic concentration (μM), r_u and r_b are unbound and bound ribosome concentrations (μM), and a_{ex} is the extracellular antibiotic concentration. The flux

$$J(a_{\text{ex}}, a) = P_{\text{in}} a_{\text{ex}} - P_{\text{out}} a$$

models membrane exchange, and the reversible binding term

$$f(r_u, r_b, a) = -k_{\text{on}}\, a\, (r_u - r_{\min}) + k_{\text{off}}\, r_b$$

captures ribosome-drug interactions, with dissociation constant $K_D = k_{\text{off}}/k_{\text{on}}$ [71].

At this stage the system is not yet closed, because the constitutive relations for the growth rate λ (h^{-1}) and the ribosome synthesis rate $s(\lambda)$ ($\mu\text{M}h^{-1}$) have not been specified. The original model closes the system by tying both quantities to steady-state growth laws. In the absence of antibiotic, the translation-capacity law fixes the unbound ribosome concentration at the drug-free growth rate λ_0, and the nutrient-capacity law determines how ribosome content varies with growth under inhibition [71][189]. These steady states define the total ribosome pool

$$r_{\text{total}} = r_u + r_b,$$

and the model enforces steady-state mass balance via

$$s(\lambda) = \lambda r_{\text{total}}.$$

To complete closure, the model assumes that unbound ribosomes remain growth-limiting under antibiotic exposure, extending the empirical linear relation between growth rate and unbound ribosome concentration into the inhibited regime. This yields the closure condition

$$\lambda = \kappa_T (r_u - r_{\min}), \tag{3.4}$$

where κ_T is the translational capacity and $r_{\min}$ is the minimal ribosomal mass fraction at zero growth. In this framework, λ_0 denotes the drug-free growth rate, $r_{\max}$ and $r_{\min}$ are the maximal and minimal ribosomal mass fractions observed across growth conditions, and $\Delta r = r_{\max} - r_{\min}$. Combining the translation-limited and nutrient-limited branches of the growth laws and enforcing these limits yields

$$r_{\text{total}} = r_u + r_b = r_{\max} - \lambda \Delta r \left(\frac{1}{\lambda_0} - \frac{1}{\kappa_T \Delta r} \right), \tag{3.5}$$

so that total ribosome concentration increases as growth slows (see Figure 3.1, maroon line). Substituting this into the steady-state balance $s(\lambda) = \lambda r_{\text{total}}$ gives

$$s(\lambda) = \lambda r_{\text{total}} = \lambda \left[r_{\max} - \lambda \Delta r \left(\frac{1}{\lambda_0} - \frac{1}{\kappa_T \Delta r} \right) \right], \tag{3.6}$$

which scales quadratically with λ and links ribosome accumulation to translational slowdown during antibiotic exposure. A full algebraic derivation of (3.5)–(3.6) is provided in the Supplementary Information of [71].

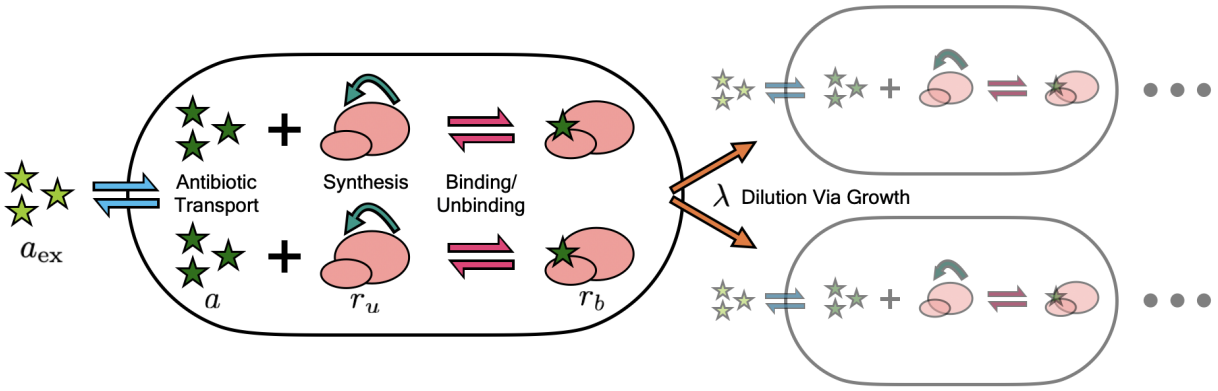


Figure 3.2: Mechanistic schematic of ribosome-targeting antibiotic interactions. The model tracks three intracellular variables: free antibiotic a (dark-green stars), unbound ribosomes r_u (peach ovals), and antibiotic-bound ribosomes r_b (dark-green star plus peach ovals). Extracellular antibiotic a_{ex} (light-green stars) enters and exits through membrane influx/efflux (cyan arrows), accumulates internally, and binds to r_u to form r_b (pink arrows). Ribosomes are synthesized at rate s (teal arrow), and all molecular species are diluted at the growth rate λ (orange arrows). Faded daughter-cell silhouettes illustrate exponential growth and dilution across generations.

Combining (3.3) with the empirical growth-law relationships links the steady-state synthesis rate, defined along the nutrient-limited branch (see Figure 3.1, maroon line), to the translation-limited branch (see Figure 3.1, brown line), which closes the system under the assumption that ribosomes remain growth-limiting during antibiotic inhibition. This closure results in a cubic steady-state relation between the normalized growth rate λ/λ_0 and the extracellular antibiotic concentration a_{ex}

$$0 = \left(\frac{\lambda}{\lambda_0}\right)^3 - \left(\frac{\lambda}{\lambda_0}\right)^2 + \left(\frac{\lambda}{\lambda_0}\right)\left[\frac{1}{4}\left(\frac{\lambda_0^*}{\lambda_0}\right)^2 + \frac{a_{ex}}{2\text{IC}_{50}^*}\left(\frac{\lambda_0^*}{\lambda_0}\right)\right] - \frac{1}{4}\left(\frac{\lambda_0^*}{\lambda_0}\right)^2. \tag{3.7}$$

This formulation captures how intracellular growth inhibition arises from the coupled dynamics of antibiotic binding, transport, and translation under the physiological constraints

imposed by the growth laws. Only two composite parameters govern this relationship

$$\lambda_0^* = 2\sqrt{P_{\text{out}}\kappa_T K_D}, \tag{3.8}$$

$$\text{IC}_{50}^* = \frac{\Delta r \lambda_0^*}{2P_{\text{in}}}. \tag{3.9}$$

Here, λ_0^* (3.8) represents the critical reversibility rate that delineates the transition between irreversible and reversible inhibition regimes, while IC_{50}^* defines a characteristic concentration scale for the extracellular drug. These two quantities provide normalization factors for the drug-free growth rate λ_0 and the external antibiotic concentration a_{ex}, allowing the cubic steady-state equation to be expressed in dimensionless form. When λ_0^* is small (the irreversible limit), growth decreases abruptly with increasing antibiotic concentration, reflecting the strong irreversibility of binding seen for streptomycin and kanamycin. By contrast, for larger λ_0^* (the reversible limit), inhibition occurs more gradually, consistent with the weaker, reversible binding kinetics of tetracycline and chloramphenicol. In both cases, the qualitative response arises from the same underlying cubic constraint, differing only in kinetic reversibility. Notably, λ_0^* and IC_{50}^* vary systematically across nutrient conditions, even though κ_T and Δr are universal constants, and the binding affinity K_D is largely nutrient-independent.

Although both quantities differ between glucose- and glycerol-grown cells, they remain essentially unchanged when amino acids or nucleotides are supplemented into the medium, as reported in [71]. This pattern suggests that susceptibility is not primarily controlled by intracellular precursors but instead by processes linked to the carbon source itself. In particular, switching from glucose to glycerol alters carbon flux, ATP yield, and the cell's energetic state, all of which influence membrane composition, proton motive force, and the activity of transporters mediating antibiotic influx and efflux. These factors directly modulate P_{in} and P_{out}, providing a mechanistic explanation for why carbon source, not supplementation with amino acids or nucleotides, shifts the effective reversibility rate and the characteristic concentration scale [71]. In quantitative terms, antibiotic susceptibility is described by the half-inhibition concentration, IC_{50}, defined as the extracellular antibiotic concentration that reduces the steady-state growth rate to half of the drug-free growth rate. In this way, the characteristic scale IC_{50}^* introduced in (3.9) provides the model-based reference from which IC_{50} can be interpreted. IC_{50} thus connects the measurable degree of inhibition to the kinetic parameters that define IC_{50}^* and to the physiological drug-free growth rate λ_0. Distinct scaling patterns are shown across antibiotics with differing binding reversibility. For streptomycin and kanamycin, IC_{50} increases with λ_0, meaning that fast-growing cells are less susceptible. For tetracycline and chloramphenicol, IC_{50} decreases with λ_0, such that fast-growing cells are more vulnerable [71].

An important insight from this analysis is that growth rate-dependent antibiotic susceptibility is determined by the ratio λ_0^*/λ_0. To obtain the half-inhibitory concentration IC_{50}, the cubic steady-state relation (3.7) is evaluated at $\lambda = \lambda_0/2$, where growth is reduced to half of the drug-free rate. Substituting $a_{\mathrm{ex}} = \mathrm{IC}_{50}$ into (3.7) and simplifying yields a closed-form universal susceptibility curve

$$\frac{\mathrm{IC}_{50}}{\mathrm{IC}_{50}^*} = \frac{1}{2}\left(\frac{\lambda_0}{\lambda_0^*} + \frac{\lambda_0^*}{\lambda_0}\right), \tag{3.10}$$

which links the measurable half-inhibition concentration IC_{50} to the drug-free growth rate λ_0 and critical reversibility rate λ_0^*. The cubic relation (3.7) arises from combining the quadratic dependence of the synthesis term $s(\lambda) = \lambda\, r_{\mathrm{total}}$ with the first-order dilution terms $-\lambda$ in the steady-state balances. Together these generate the $(\lambda/\lambda_0)^3$ and $(\lambda/\lambda_0)^2$ components, while linear mass-action binding and first-order transport contribute only through the composite parameters λ_0^* and IC_{50}^*, which set the coefficients of the linear and constant terms. Evaluating this steady-state balance identifies the antibiotic concentration at which inhibition and recovery fluxes are in equilibrium, when growth is halved. The resulting curve quantifies how susceptibility scales with both growth rate and inhibition reversibility.

Two limiting behaviours arise from (3.10). When the drug-free growth rate λ_0 exceeds the critical reversibility rate λ_0^* ($\lambda_0^* \ll \lambda_0$), the half-inhibition concentration IC_{50} increases with λ_0, meaning that fast-growing cells are less susceptible. This is consistent with irreversible inhibitors such as streptomycin and kanamycin, which bind to the 30S ribosomal subunit and cause mistranslation and ribosome inactivation. However, when the drug-free growth rate λ_0 is smaller than the critical reversibility rate λ_0^* ($\lambda_0^* \gg \lambda_0$), IC_{50} decreases with λ_0, meaning that fast-growing cells are more vulnerable. This is consistent with reversible inhibitors such as tetracycline and chloramphenicol, which transiently block translation by interfering with tRNA binding and peptide elongation on the ribosome [71]. Intuitively, the ratio λ_0^*/λ_0 captures the competition between the timescale of antibiotic binding reversibility and the timescale of cellular growth, reversible inhibitors act quickly but transiently, whereas irreversible inhibitors act more slowly yet persistently. The parameter IC_{50}^* thereby provides a growth-rate-independent scale for the external antibiotic concentration, with $a_{\mathrm{ex}} > \mathrm{IC}_{50}^*$ required for effective inhibition regardless of nutrient condition. The cubic approximation (3.7) arises from simplifying the full system under a quasi-steady-state assumption, where binding and unbinding occur rapidly relative to growth. In the reversible (antibiotics like tetracycline and chloramphenicol) limit ($\lambda_0^*/\lambda_0 \gg 1$), the cubic equation can be reduced and solved for λ/λ_0, yielding a Langmuir-type relationship between the normalized growth rate λ/λ_0 and extracellular antibiotic concentration (see

Section 3.2, (3.11)). Here, a_{ex} denotes the extracellular antibiotic concentration, and

$$\text{IC}_{50} = \frac{\text{IC}_{50}^{*}\lambda_0^{*}}{2\lambda_0}$$

defines the half-inhibitory concentration written inversely proportional to drug-free growth rate λ_0 (see the Supplementary Information of [71] for a full derivation). This formulation provides a quantitative link between molecular kinetics and growth inhibition, unifying the reversible and irreversible binding regimes under a single steady-state framework.

Following the steady-state formulation, the above modeling framework was extended to investigate dynamic antibiotic perturbations, where cells experience time-dependent rather than constant drug exposure [72]. In this refinement, the model included explicit antibiotic pulse-dosing phases. In this regime, a step pulse of antibiotic with intensity S and duration T (fixed total dose $S \times T$) was introduced. The model predicts only for the low-affinity, reversible (large λ_0^{*}) antibiotics like tetracycline and chloramphenicol, a transient growth rate overshoot ($\lambda > \lambda_0$) after antibiotic removal, arising from increased ribosome synthesis during inhibition and rapid unbinding once extracellular antibiotic is cleared. Dissociation of drug-ribosome complexes rapidly restores the pool of free ribosomes following the pulse. The magnitude of this overshoot depends nonlinearly on both pulse duration and nutrient quality. Media with lower drug-free growth rate λ_0 exhibit stronger upregulation of ribosomal synthesis $s(\lambda)$, amplifying the transient increase in growth rate [72]. Conversely, in the high-affinity, irreversible regime (small λ_0^{*}) for antibiotics like streptomycin and kanamycin, the model predicts no post-pulse growth rate overshoot. Instead, cells exhibit hysteresis and prolonged growth suppression due to the persistence of inactive, drug-bound ribosomes. This dissimilarity motivated restricting subsequent pulse-response analysis to the reversible case, which captures the short-term recovery dynamics relevant to tetracycline or chloramphenicol-based treatment. Importantly, the original model continued to assume that post-pulse growth was limited solely by the abundance of free ribosomes.

In reality, recovery is often constrained by amino acid availability or depletion of metabolic enzymes. In this original model, the initial rise in growth following antibiotic removal stems from the rapid unbinding of antibiotic, which transiently leaves an over-abundance of unbound ribosomes. If the closure condition described earlier (assuming unbound ribosomes remain growth-limiting under translation inhibition, see Figure 3.1, brown line) is applied, this surplus leads to a short-lived spike in growth rate [72]. However, the elevated ribosome pool must be balanced by renewed synthesis of anabolic and catabolic proteins to re-establish metabolic flux. This trade-off reflects proteome partitioning principles, where total protein concentration is conserved and increased ribosomal

synthesis comes at the expense of other functional sectors. In nutrient-rich conditions, ribosomal and anabolic fractions expand while catabolic proteins diminish, in nutrient-poor conditions, the reverse occurs. Accurate modeling of post-antibiotic recovery therefore requires coupling ribosome synthesis dynamics to proteome allocation laws [72].

Although an explicit proof is omitted, the model satisfies standard regularity conditions for local existence and uniqueness on each interval where the right-hand side is smooth. The ODE system is continuously differentiable with respect to its state variables within each growth regime (pre-pulse, pulse, and post-pulse). At the boundaries between regimes, the definition of the growth rate λ changes, making the right-hand side piecewise continuously differentiable rather than globally C^1. Because these switching times are externally prescribed by the pulse protocol and do not depend on the system state, solutions on each smooth interval can be uniquely extended and concatenated. Thus the overall trajectory is uniquely defined given initial conditions, and the model is well-posed for simulation, sensitivity analysis, and optimization in the subsequent chapters. The biologically constrained parameter ranges further ensure that solutions remain bounded and physiologically meaningful over all relevant time intervals [82].

3.1.1 Our Correction: New Growth Regime

While the original model (3.3) assumes that growth rate is determined entirely by the abundance of free ribosomes, a reasonable approximation under steady-state conditions, this assumption becomes overly restrictive during dynamic, non-equilibrium transitions such as antibiotic exposure and removal. Although ribosome abundance determines the potential rate of protein synthesis, additional physiological processes also constrain growth during recovery. Following release from translational inhibition, the supply of amino acids and the abundance of metabolic enzymes may become limiting even when ribosome levels remain elevated. This indicates that the transient growth rate after antibiotic removal is not governed solely by the instantaneous protein synthesis rate but instead depends on the coordinated rebalancing of biosynthetic and metabolic sectors. Synthesis of non-ribosomal proteins therefore plays a vital role in restoring balanced growth. Consequently, overshoots in predicted growth rate based solely on ribosome abundance are unlikely to occur in practice, emphasizing the need for models that incorporate broader physiological regulation beyond ribosome-limited translation.

In this thesis, the model is corrected to incorporate post-antibiotic growth limitation by metabolic capacity rather than ribosome concentration alone. Specifically, after antibiotic removal, ribosome synthesis continues even as growth remains suppressed due to reduced

amino acid pools and delayed proteome remodeling. In this regime, the concentration of metabolic proteins, and thus the supply rate of amino acids, becomes the growth-limiting side of the protein synthesis supply–demand balance, while the ribosome pool temporarily exceeds translational demand until metabolic flux is restored. To make this modification explicit, the corrected model adopts a phase-dependent growth constraint. Before the pulse, growth follows the translation-limited branch of the growth law (3.1)

$$\lambda = \kappa_T(r_u - r_{\min}),$$

and the system is closed using the steady-state balance

$$s(\lambda) = \lambda\, r_{\text{total}}$$

as in the original formulation. During the pulse, this same translational regime applies, with antibiotic transport and reversible binding modifying r_u and r_b through the terms in (3.3). After antibiotic removal, unbound ribosomes are no longer growth-limiting. Recovery therefore follows the nutrient-limited branch of the growth law (3.2)

$$\lambda = \kappa_N\big(r_{\max} - r_{\text{total}}\big),$$

reflecting the temporary limitation imposed by amino acid availability and metabolic enzyme abundance. The synthesis rate remains defined by the same steady-state closure condition in all phases. This piecewise specification resolves the artificial overshoot in the original model and preserves a consistent link between growth rate and ribosome pool even as the limiting process shifts from translation to metabolism.

This correction is illustrated in Figure 3.3, which compares the original and revised model predictions for growth rate dynamics during and after an antibiotic pulse. In the earlier formulation [72], recovery exhibits an unphysical growth rate overshoot above the drug-free steady-state growth rate due to the assumption that ribosomes remain growth-limiting after antibiotic removal. In contrast, when post-pulse growth is constrained by metabolic capacity, the overshoot in growth rate is eliminated, producing a physiologically realistic recovery trajectory consistent with balanced proteome reallocation.

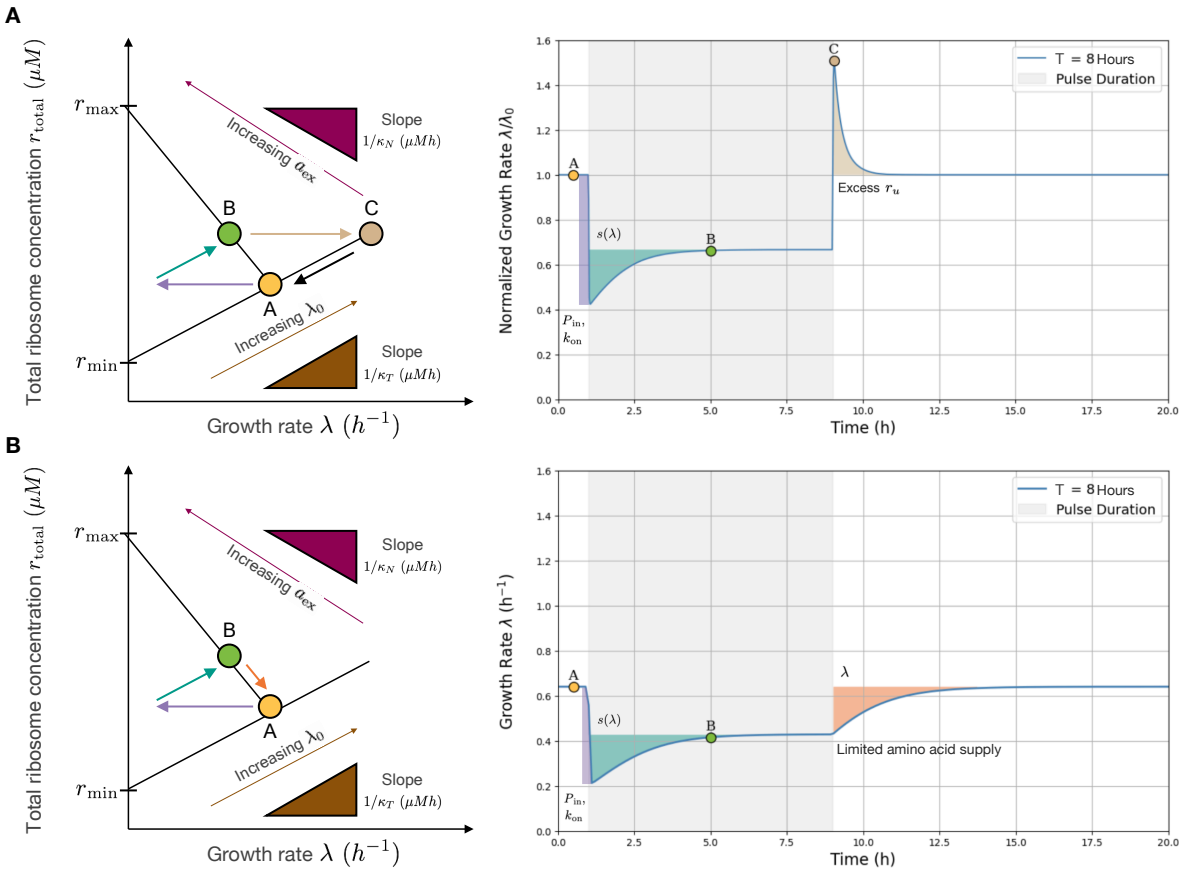


Figure 3.3: Modeled growth rate dynamics of *E. coli* under a ribosome-targeting antibiotic pulse. The drug-free steady-state growth rate λ_0 (A, yellow) drops sharply upon antibiotic addition (grey region, purple arrow) and partially recovers as new ribosomes are synthesized (cyan arrow), reaching a transient quasi-steady state (B, lime). (A) In the original model [72], post-pulse growth overshoots λ_0 (C, tan) due to the translation-limited assumption. (B) In the revised model, recovery is limited by metabolic capacity rather than ribosome abundance, removing the growth rate overshoot and producing a physiologically consistent triangular recovery.

3.2 Antibiotic Inhibition Modeling

Understanding how antibiotics inhibit bacterial growth is essential for modeling pharmacodynamic response. In the reversible limit of model (3.3), translation inhibition by antibiotics such as tetracycline and chloramphenicol is well approximated by a Langmuir-type binding function, which assumes reversible, non-cooperative interactions between antibiotic molecules and ribosomal targets. This captures how increasing extracellular antibiotic concentration progressively suppresses growth, described by

$$\lambda(a_{\text{ex}}) = \frac{\lambda_0}{1 + \left(\frac{a_{\text{ex}}}{\text{IC}_{50}}\right)}, \tag{3.11}$$

where λ_0 is the drug-free growth rate, a_{ex} the external antibiotic concentration, and IC_{50} the half-maximal inhibitory concentration, the point where growth is halved. The IC_{50} serves as a standardized measure of antibiotic efficacy, allowing comparison across compounds and nutrient conditions. This relation is mathematically equivalent to the Langmuir adsorption isotherm for single-site, non-interacting ligand binding [130][193], and is a special case of the Hill equation with coefficient $n = 1$ [174]. The Langmuir model is appropriate for tetracycline and other reversible inhibitors that bind ribosomes without cooperative effects [71]. This simplified form aligns with prior quantitative studies treating antibiotic action as saturable growth inhibition, where IC_{50} provides a natural metric for potency under different nutrient environments [71][174][189]. The formulation also permits direct extraction of IC_{50} from growth rate data, linking experimental inhibition curves to the kinetic model. Parameter estimation is performed by minimizing a weighted mean squared error cost function between measured and simulated growth rates (Section 3.4), and sensitivity analysis quantifies how IC_{50} influences recovery and ribosome dynamics (Section 3.3).

3.3 Sensitivity Analysis

Sensitivity analysis quantifies how small perturbations in model parameters affect specific outputs, helping to identify which parameters most strongly control system responses such as growth rate, recovery time, or macromolecular ratios [173][181]. It can be performed locally, by perturbing parameters near a nominal value, or globally, by sampling across a vast parameter space.

3.3.1 First-Order Sensitivity Analysis

A common method for computing local sensitivities is the finite-difference approximation [19]. Let $f(p)$ denote a model output as a function of parameter p. The analytical definition of the (absolute) sensitivity coefficient is

$$S_f = \frac{\partial f}{\partial p},$$

and it can be estimated numerically using the forward finite-difference approximation

$$S_f \approx \frac{f(p + \epsilon p) - f(p)}{\epsilon p}, \tag{3.12}$$

where ϵ is a small perturbation factor, typically 1-10% of the baseline parameter value. To capture relative rather than absolute changes, the logarithmic sensitivity is defined as

$$S_f^{\log} = \frac{\partial \ln f}{\partial \ln p} = \frac{p}{f}\frac{\partial f}{\partial p},$$

and is numerically approximated using

$$S_f^{\log} \approx \frac{\log f(p + \epsilon p) - \log f(p)}{\log(1 + \epsilon)}. \tag{3.13}$$

This representation is especially useful when parameters or outputs span multiple orders of magnitude, or when sensitivity is interpreted as a proportional effect [19]. The central-difference form

$$S_c = \frac{f(p + \epsilon p) - f(p - \epsilon p)}{2\epsilon p},$$

offers higher-order accuracy but is less stable for stiff systems, where small backward perturbations can drive the solver into unstable regions or amplify truncation errors. Forward differencing avoids this by evaluating in the stable direction of integration, maintaining robustness for ODE-based biological models [169].

3.3.2 One-at-a-Time Perturbation Strategy

Sensitivity analysis is often performed using a one-at-a-time (OAT) strategy, where a single parameter is perturbed while all others remain fixed. This allows independent evaluation of each parameter's effect on the model output [181]. The OAT method is computationally efficient and easy to interpret when parameters are weakly coupled, although it cannot capture parameter interactions that may arise in nonlinear systems.

3.3.3 Second-Order Sensitivity and Hessian Estimation

Beyond first-order sensitivities, second-order effects can be evaluated using the Hessian matrix, which quantifies the local curvature of the model output surface with respect to multiple parameters [22]. Each element of the Hessian is analytically defined as

$$H_{ij} = \frac{\partial^2 f}{\partial p_i \partial p_j}.$$

It is numerically approximated via a central finite-difference scheme as

$$H_{ij} \approx \frac{f(p_i + \epsilon_i, p_j + \epsilon_j) - f(p_i + \epsilon_i, p_j - \epsilon_j) - f(p_i - \epsilon_i, p_j + \epsilon_j) + f(p_i - \epsilon_i, p_j - \epsilon_j)}{4\epsilon_i \epsilon_j}. \quad (3.14)$$

Here, H_{ij} represents the mixed partial derivative of the model output with respect to parameters p_i and p_j, with perturbations ϵ_i and ϵ_j applied to each. The Hessian provides insight into parameter coupling, stiffness, and sloppiness directions in parameter space where the curvature of the cost function is high or low [173]. In this context, stiff directions correspond to parameter combinations that produce large changes in model output even for small perturbations, reflecting strong constraint by the data. Sloppy directions, however, correspond to combinations where large parameter variations yield little change in the output, highlighting weak identifiability or redundancy among parameters [73][173].

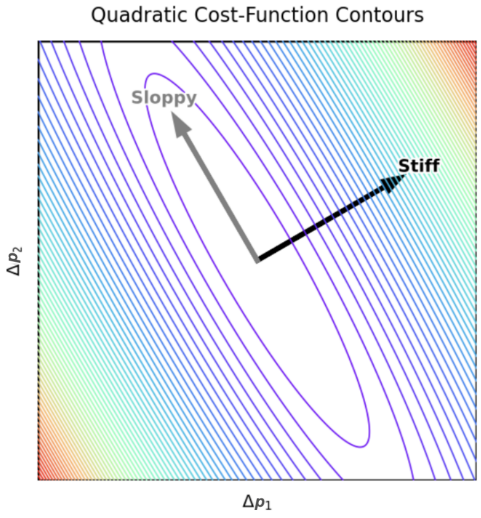


Figure 3.4: Contour plot of the quadratic cost approximation $Z(\Delta p) = \frac{1}{2}\,\Delta p^\top H\,\Delta p$. Level sets form ellipses whose principal axes follow the stiff and sloppy eigenvectors of H, with axis lengths scaling as $1/\sqrt{\lambda_i}$. Black and grey arrows mark the stiff and sloppy directions.

Analyzing the eigenvalues of the Hessian reveals how sharply outputs respond to parameter changes, informing identifiability and confidence estimation. Many complex biological models exhibit highly elongated, sloppy cost contours, with only a few stiff directions dominating system behaviour [73][170]. A visual representation of this concept is provided in Figure 3.4, where a toy model with known curvature structure highlights stiff and sloppy parameter directions through surface topology.

3.3.4 Composite Parameters and Coupled Effects

Some models include composite parameters that combine primary terms, such as the dissociation constant $K_D = k_{\text{off}}/k_{\text{on}}$ or the membrane permeability ratio $R_P = P_{\text{in}}/P_{\text{out}}$. Sensitivity to these quantities can be deduced from the sensitivities of their individual components. Using logarithmic derivatives, the relative sensitivity of a ratio $x = a/b$ is given by

$$S_x^{\log} = S_a^{\log} - S_b^{\log}.$$

Thus, for $K_D = k_{\text{off}}/k_{\text{on}}$

$$S_{K_D}^{\log} = S_{k_{\text{off}}}^{\log} - S_{k_{\text{on}}}^{\log},$$

and for $R_P = P_{\text{in}}/P_{\text{out}}$

$$S_{R_P}^{\log} = S_{P_{\text{in}}}^{\log} - S_{P_{\text{out}}}^{\log}.$$

These relationships clarify how opposing perturbations in the numerator and denominator can amplify or cancel one another, leading to ambiguous or decreased net effects when both terms vary simultaneously. Composite parameters such as K_D and R_P are more physiologically meaningful than their individual components because they encompass the balance between coupled processes that jointly determine effective antibiotic action. Specifically, K_D represents the equilibrium between antibiotic binding and unbinding to ribosomes, controlling the fraction of inhibited ribosomes. R_P combines the relative rates of antibiotic influx and efflux across the membrane, controlling intracellular accumulation. Analyzing sensitivities in terms of these composite parameters therefore provides clearer biological interpretation and highlights which coupled processes dominate the system's response to perturbations. Because both K_D and R_P represent quasi-steady-state ratios of fast underlying processes, they summarize effective equilibria that remain stable on the slower timescales relevant to growth and recovery dynamics.

3.4 Parameter Estimation and Model Fitting

Mathematical models in biology typically contain parameters that must be estimated from experimental data [53][137]. Parameter estimation is the process of identifying parameter values that minimize the discrepancy between model predictions and experimental data [19][169]. In this thesis, parameter estimation plays a central role in fitting growth dynamics, recovery times, and inhibition curves. A common approach defines an objective (or cost) function that quantifies the deviation between model outputs and experimental observations. The simplest and most widely used form is the mean squared error (MSE) objective function [19][169]

$$\mathrm{MSE}(\boldsymbol{p}) = \frac{1}{n}\sum_{i=1}^{n}\left(y_i^{\mathrm{exp}} - y_i^{\mathrm{model}}(\boldsymbol{p})\right)^2, \tag{3.15}$$

where y_i^{exp} are experimental measurements, $y_i^{\mathrm{model}}(\boldsymbol{p})$ are model predictions for a parameter vector $\boldsymbol{p}$, and n is the number of data points. Minimizing (3.15) yields the parameter set that best reproduces the observations. In cases where experimental uncertainty varies across replicates, a weighted least squares formulation can improve robustness. Each residual is scaled by a weight w_i, typically chosen as the inverse of the variance of y_i^{exp}

$$\mathrm{WMSE}(\boldsymbol{p}) = \frac{1}{n}\sum_{i=1}^{n} w_i\left(y_i^{\mathrm{exp}} - y_i^{\mathrm{model}}(\boldsymbol{p})\right)^2. \tag{3.16}$$

Weighted least squares are particularly valuable in biological data sets where variability differs across measurements or conditions, allowing more reliable points to carry greater influence [19]. Optimization can be carried out using gradient-based algorithms, such as BFGS, or derivative-free methods like Nelder-Mead, depending on model smoothness, dimensionality, and numerical cost [22][169]. Parameter bounds are often imposed to ensure biological plausibility of estimates. Parameter identifiability, whether a unique parameter set can be recovered from data, can be assessed using sensitivity and curvature analyses involving the Hessian matrix (see Subsection 3.3.3) [173][181]. Once optimal parameters are obtained, uncertainty is evaluated through relative error propagation and confidence intervals derived from standard deviations [19], as detailed in Chapter 4.

3.4.1 Information Criteria for Model Comparison

In later chapters, successive refinements of a mechanistic model for reversible antibiotic inhibition are compared using the Akaike Information Criterion (AIC) and the Bayesian

Information Criterion (BIC). These criteria select the model that provides the best trade-off between goodness of fit and complexity. For a model with residual sum of squares (RSS) and k free parameters evaluated on n data points, the criteria are

$$\mathrm{AIC} = 2k + n \ln\left(\frac{\mathrm{RSS}}{n}\right), \tag{3.17}$$

$$\mathrm{BIC} = k \ln(n) + n \ln\left(\frac{\mathrm{RSS}}{n}\right), \tag{3.18}$$

where smaller values indicate stronger support. Both measures penalize the inclusion of additional parameters, but BIC imposes a stronger penalty proportional to $\ln(n)$ and therefore favours simpler models when their performance is comparable. When the likelihood is Gaussian, as is appropriate for normally distributed experimental errors, minimizing AIC or BIC is equivalent to maximizing the penalized likelihood.

In this thesis, residuals from delay time, RNA/protein ratios, and inhibition curves are standardized by their experimental variances prior to computing RSS. This normalization removes scale differences between datasets and ensures that AIC and BIC comparisons reflect biological accuracy rather than fitting biases arising from measurement units. Because each model is evaluated on the same n and on identically normalized residuals, differences in AIC and BIC scores directly quantify whether added physiological structure (such as metabolic limitation or feedback synthesis) yields statistically meaningful improvement. A significantly lower criterion therefore indicates that the additional mechanism is required to explain the data rather than being a numerical artifact of over-parameterization [1][187].

Chapter 4

Materials & Methods

All experiments were performed in at least two independent biological replicates on different days (see Table 4.1, Table 4.2, and Table 4.3 for replicate details).

4.1 Quantities of Interest

The refined model aims to predict three critical physiological outputs that can be directly compared to experimental measurements. Together, these outputs, the delay time Δt, the RNA/protein ratio ρ, and the inhibitory concentration IC_{50}, form a minimal but physiologically complete set of constraints for the corrected model. Each quantity probes a distinct component of the system. IC_{50} constrains steady-state susceptibility and fixes the binding and transport kinetics that determine intracellular drug availability. Δt captures the total growth deficit caused by the pulse, incorporating both the biomass not accumulated during antibiotic inhibition and the physiological adjustment required after drug removal. ρ reports on proteome reallocation through the total ribosome concentration during and after the pulse. No single measurement provides enough information to constrain the model, but taken together they span steady-state susceptibility and the full dynamical response to a pulse, from inhibited growth to the subsequent return to balanced physiology. For this reason, these three quantities were selected as the core experimental targets used both for model comparison and for parameter estimation.

1. **Delay Time (Δt):** This quantity measures the effective "time lost" to growth following an antibiotic pulse, integrating the entire inhibition period into a single, robust

metric. Specifically, Δt is defined as the horizontal shift between the x-intercepts of linear fits to the $\log(\mathrm{OD}_{600})$ trajectories before and after the pulse. Both fits are constrained to have slope λ_0, the drug-free growth rate, guaranteeing that the pre- and post-pulse phases are compared under equivalent growth conditions. In practice, the log-transformed OD data are extrapolated, and the shift required to align the post-pulse trajectory with the pre-pulse trajectory defines Δt. The instantaneous growth rate $\lambda(t) = d[\ln(\mathrm{OD})]/dt$ changes strongly during recovery and is sensitive to noise. As a result, Δt provides a stable and biologically meaningful measure of recovery dynamics. Let $N(t)$ denote the population density (proportional to OD_{600}). In an untreated culture,

$$N_{\text{drug-free}}(t) = N_0 e^{\lambda_0 t},$$

while for a pulsed culture delayed by Δt,

$$N_{\text{pulse}}(t) = N_0 e^{\lambda_0 (t-\Delta t)}.$$

Taking logarithms gives

$$\ln N_{\text{drug-free}}(t) - \ln N_{\text{pulse}}(t) = \lambda_0 \Delta t,$$

showing that $\lambda_0 \Delta t$ represents the effective reduction in population caused by the pulse. An illustrative schematic is shown in Figure 4.1.

2. **RNA/Protein Ratio (ρ):** Serving as a proxy for ribosomal concentration, the RNA/protein ratio ρ was computed experimentally as the ratio of RNA mass to protein mass at each time point. In simulations, this is computed as the total ribosome concentration

$$\rho_{\text{sim}} = r_{\text{total}} = r_u + r_b.$$

Experimental error in ρ was computed by propagating relative uncertainty from independent RNA and protein measurements. To enable direct comparison between experiment and simulation, ρ values were normalized by their respective pre-pulse baselines, removing the unknown proportionality constant between ribosome concentration and RNA/protein ratio and allowing trends to be compared directly.

3. **Inhibitory Concentration (IC_{50}):** The inhibitory concentration IC_{50} quantifies the drug level required to reduce the growth rate by half relative to the drug-free condition. In this model, IC_{50} arises analytically from the steady-state susceptibility relation (see (3.10)), making it fully determined by the binding kinetics and transport parameters rather than treated as an independent fit parameter. Including IC_{50}

in the optimization therefore ensures consistency between the dynamic model and steady-state inhibition measurements obtained from the inhibition curve experiments described in Section 4.2.2.

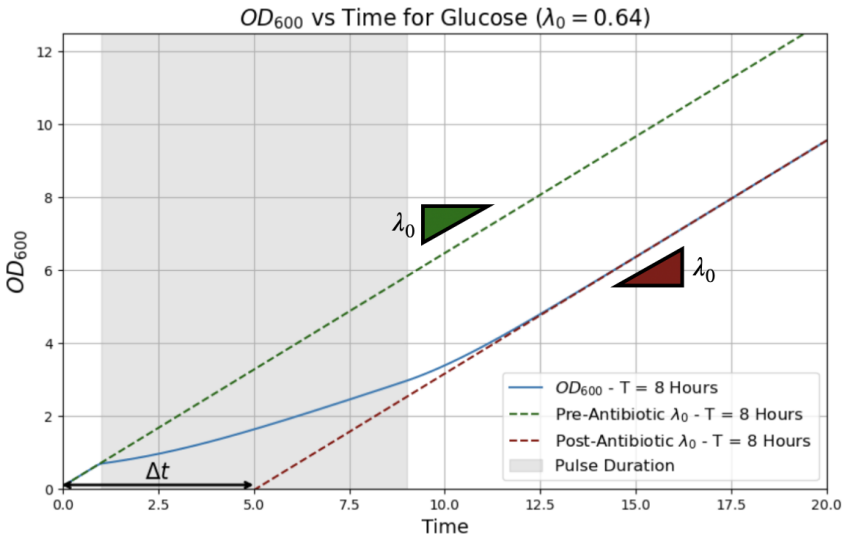


Figure 4.1: Illustration of delay time (Δt) determination from simulated OD_{600} trajectories (glucose, $\lambda_0 = 0.64\,h^{-1}$). For the derivation, Δt is computed from linear fits to the log-transformed OD_{600} data, as described in the text, but OD_{600} is plotted here for visual clarity. The antibiotic pulse (grey region) suppresses growth, after which the culture resumes exponential growth in parallel with the untreated reference. Dashed green and red guides indicate the pre- and post-pulse extrapolations with slope λ_0. The horizontal offset between their x-intercepts defines Δt, quantifying the effective time-equivalent loss in growth due to the pulse.

4.2 Experimental Design

4.2.1 Growth of Bacterial Culture

Bacterial Strain

All experiments displayed in this thesis were conducted using *Escherichia coli* K-12 strain MG1655. This wild-type, unmodified strain is commonly used in laboratory studies due to its well-characterized physiology.

Antibiotic Preparation

Tetracycline hydrochloride (Fisher Scientific, BP912-100) was used in all experiments. It is a reversible, low-affinity ribosome-targeting antibiotic. A concentrated stock solution was prepared at 108 mg in 10 mL sterile deionized water (22.5 mM), sterile-filtered, stored in a single 15 mL tube, and kept at −20°C protected from light to prevent photodegradation. Working solutions were freshly diluted from the frozen stock as needed, with the stock promptly refrozen after each use to preserve effectiveness. Inhibition curve experiments used final tetracycline concentrations ranging from 0 to 2.0 μM.

Growth Media

All experiments were performed using MOPS-buffered minimal media supplemented with either glucose or glycerol as the sole carbon source [138]. The medium was prepared per 100 mL using 10 mL of 10× MOPS buffer (Teknova, M2101), 1 mL of 0.132 M phosphate solution (primarily sodium phosphate [Na_2PO_4], with potassium phosphate used when sodium phosphate was unavailable), and 1 mL of 20% stock solution of either glucose (w/v) or glycerol (v/v), yielding a final carbon source concentration of 0.2%. Sterile deionized water was added to reach the final volume. The 10× MOPS stock was maintained as a 100 mL solution at −20°C and aliquoted into 10 mL portions. These aliquots were stored frozen and thawed immediately prior to use. The same medium formulation was used for all experiments, including those involving tetracycline treatment. Drug-free growth rates aimed to reproduce $\lambda_0^{\mathrm{GLU}} = 0.64\,h^{-1}$ for glucose and $\lambda_0^{\mathrm{GLY}} = 0.40\,h^{-1}$, based on values reported in [71].

4.2.2 Growth Experiments

E. coli MG1655 was streaked onto LB agar plates and incubated at 37°C for 15–20 hours. Plates were stored at 4°C and used within three weeks. For each experiment, cultures were grown in sterile 20 mm×150 mm glass test tubes sealed with plastic caps. All tubes were incubated in an Innova MaxQ 7000 orbital water bath shaker (Thermo Fisher Scientific) at 37°C with shaking at 250 rpm and tilted at an approximate 45° angle to support aeration. A single colony was inoculated into 2 mL of LB broth to establish a seed culture, which was incubated under the conditions described above for 4 hours. To ensure that all experiments began from steady-state exponential growth, cultures were grown for approximately 5–10 generations in the experimental media before measurements were collected. Log-transformed OD_{600} measurements were verified to be linear in time, and

cultures were maintained below $OD_{600} = 0.600$ to keep them well within the exponential regime and far from the onset of saturation.

Unless otherwise stated, all experiments followed this base culture protocol. Specific procedures for the inhibition, delay time, and RNA/protein quantification experiments are detailed below.

Inhibition Experiments

Six sterile 20 mm×150 mm glass test tubes were prepared, each containing 1 mL of MOPS minimal medium [138] supplemented with either glucose or glycerol as the sole carbon source and tetracycline at final concentrations of 0, 0.4, 0.8, 1.2, 1.6, or 2.0 μM. Once the LB seed culture reached visible turbidity, 100 μL of this seed was inoculated into each tube, which were then incubated overnight under standard conditions (37°C, 250 rpm, 45° tilt). The following morning, each overnight culture, measured to be at an $OD_{600} \approx 1.500$, was transferred into fresh 3 mL MOPS minimal medium containing the same tetracycline concentration as its corresponding overnight culture. Cultures were allowed to resume exponential growth for approximately 45-60 minutes until reaching a starting $OD_{600} \approx 0.070$. Optical density was then monitored at multiple time points spanning the exponential phase ($OD_{600} \approx 0.100$–0.600), ensuring measurements were taken within the linear growth regime. Growth rates for each antibiotic concentration were subsequently determined from the slope of the natural logarithm of OD_{600} versus time over this interval. Measured growth rates and inhibitory concentrations derived from these experiments are reported in Table 4.1.

Antibiotic Pulse Experiments

To investigate the cellular response to transient translational inhibition, cultures were subjected to a fixed-dose tetracycline pulse protocol derived from the model predictions described above. Experiments were performed in MOPS minimal medium supplemented with either glucose or glycerol as the sole carbon source [138]. Cultures were incubated at 37°C with shaking (250 rpm, 45° tilt). When $OD_{600} \approx 0.200$, tetracycline was added to initiate a finite antibiotic pulse. A constant normalized exposure intensity was maintained across all pulses using

$$a_{\mathrm{ex}} = \frac{K \cdot \mathrm{IC}_{50}}{T},$$

where T denotes the pulse duration, $\mathrm{IC}_{50}^{\mathrm{GLU}} = 1.75\,\mu\mathrm{M}$ and $\mathrm{IC}_{50}^{\mathrm{GLY}} = 1.45\,\mu\mathrm{M}$ are the inhibitory concentrations measured for glucose- and glycerol-grown cultures, respectively,

and K is an exposure constant (units of hours, h). Conceptually, K corresponds to the antibiotic area under the curve, expressed in units of IC_{50}

$$K = \frac{\text{AUC}}{\text{IC}_{50}}, \tag{4.1}$$

where $\text{AUC} = a_{\text{ex}}T$. Thus, K represents the effective inhibitory exposure scaled by the concentration required to halve growth, allowing pulse durations of different lengths to be compared on the same physiological basis. A single value of K was used within each carbon source condition to ensure that differences in cellular response reflect pulse duration rather than total exposure. Pulse durations were chosen based on model predictions for responsiveness to normalized antibiotic exposure (see Figure 4.2). For glucose-grown cultures, pulses of 2, 4, 5, 6, 8, and 10 hours were applied. For glycerol-grown cultures, durations of 4, 6, 8, and 10 hours were used.

Delay Time Pulse Experiments. Delay time measurements were conducted using the same 20 mm×150 mm glass test tubes and MOPS minimal medium described above [138]. In contrast to the inhibition experiments, overnight cultures were grown in 3 mL of drug-free medium. Once the LB seed culture reached turbidity, 200 μL of this seed was transferred to each 3 mL tube and prepared under standard incubation conditions (37°C, 250 rpm, 45° tilt). The following morning, overnight cultures, measured to be at an $OD_{600} \approx 1.500$, were diluted into 5 mL of fresh, drug-free MOPS minimal medium and allowed to resume exponential growth for 45–60 minutes, targeting a starting $OD_{600} \approx 0.070$. When $OD_{600} \approx 0.200$ was reached, tetracycline was added to administer a finite antibiotic pulse defined above, with $K = 4$ hours denoting the effective intensity consistent with [72]. During the pulse phase, OD_{600} measurements were recorded every 45 minutes. If cultures approached a maximal $OD_{600} \approx 0.600$ before the pulse ended, 1 mL of culture was transferred into 3 mL of fresh drug-free medium to maintain exponential conditions. At the end of the pulse, 1 mL of culture was removed, centrifuged at maximum speed (17,000×g) for 2 minutes, the supernatant discarded, the pellet resuspended in 1 mL of fresh drug-free medium, and this wash step repeated a second time to ensure thorough antibiotic removal. The washed cells were resuspended into 1 mL of drug-free medium and transferred to 3 mL of fresh drug-free medium to resume growth. OD_{600} measurements were obtained throughout both the pre- and post-pulse phases. The pre-pulse regime was monitored only up to $OD_{600} \approx 0.200$, at which point antibiotic was added, while post-pulse recovery was followed until $OD_{600} \approx 0.600$. These measurements captured growth in the linear regime, allowing delay time to be determined from the duration of suppressed growth following antibiotic removal. Experimental delay times were extracted using the

same definition introduced in Section 4.1 for each pulse condition, exponential fits were applied separately to the pre-pulse and post-pulse OD_{600} trajectories, and Δt was computed as the separation between the fitted intercepts of these two growth regimes.

The experimentally measured delay times for glucose- and glycerol-grown cultures across different pulse durations are listed in Table 4.2.

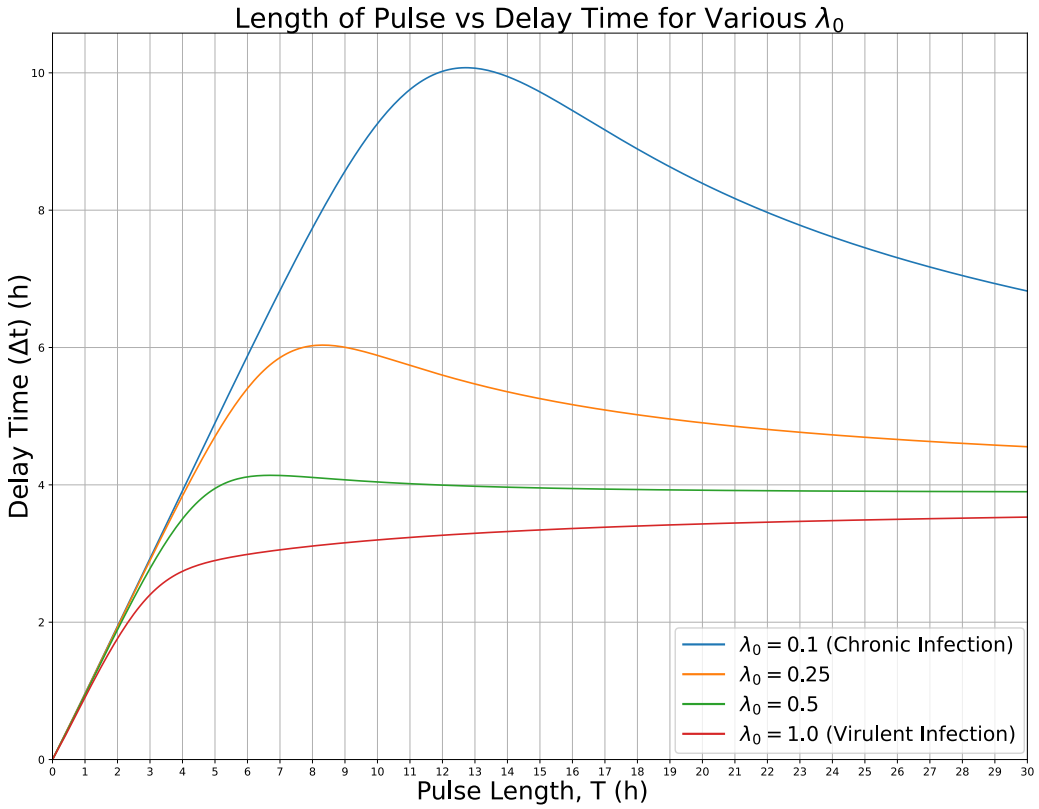


Figure 4.2: Hypothesized relationship between pulse length and delay time derived from simulations of the initially corrected model (see Subsection 3.1.1 and Subsection 4.2.3). Lower values of the drug-free growth rate (λ_0) represent slower-growing, chronic-like infections that require more extensive dosing to achieve clearance, whereas higher values of λ_0 correspond to fast-growing, virulent infections treatable on shorter timescales. This hypothesis motivated the choice of 2–10 h pulse durations in glucose and 4–10 h in glycerol for the experimental procedures described in Subsection 4.2.2.

RNA/Protein Quantification Experiments. RNA and protein quantification experiments were performed under the same culturing conditions described for the delay time measurements, using identical test tube pre-cultures and the same MOPS minimal medium supplemented with either glucose or glycerol [138]. Overnight cultures were grown drug-free, inoculated with 200 μL of LB seed culture, and prepared under standard incubation conditions (37°C, 250 rpm, 45° tilt). On the following day, the overnight culture, measured to be at an $OD_{600} \approx 1.500$, cultures were transferred into 125 mL sterile Erlenmeyer flasks containing 20 mL of fresh, drug-free MOPS minimal medium and allowed to resume exponential growth for 45–60 minutes to a starting $OD_{600} \approx 0.070$. When $OD_{600} \approx 0.200$ was reached, tetracycline was added to apply a finite antibiotic pulse following the same concentration rule defined above. During the pulse phase, OD_{600} measurements and parallel RNA/protein samples were taken every 45 minutes. For longer pulses, if a maximum $OD_{600} \approx 0.600$ was reached, 1 mL of culture was transferred into a new Erlenmeyer flask containing fresh medium to maintain exponential growth. At the end of the pulse, 1 mL of culture was removed, centrifuged at maximum speed (17,000$\times g$) for 2 minutes, the supernatant discarded, the pellet resuspended in fresh drug-free medium, and the wash repeated once more to ensure complete removal of antibiotic. The washed cells were then resuspended into 1 mL of drug-free medium and added to 15 mL of fresh medium in a clean flask to resume growth. Sampling for RNA and protein quantification was performed concurrently from the same cultures to ensure synchronized time points for total RNA/protein ratio calculations. Measurements were collected once pre-pulse, every 45 minutes during the pulse, and three times post-pulse. OD_{600} was tracked throughout, with the pre-pulse phase monitored up to $OD_{600} \approx 0.200$ and post-pulse recovery limited to $OD_{600} \approx 0.600$. Detailed descriptions of RNA and protein extraction, quantification, and normalization procedures are provided in Section 4.2.4 and Section 4.2.4.

Mean total RNA/protein ratios determined from these experiments are provided in Table 4.3.

4.2.3 Model-Based Rationale for Pulse-Dose Experiments

The physiological motivation and conceptual basis for this correction are presented in Subsection 3.1.1. Here the operational, phase-dependent equations exactly as implemented in all simulations is summarized. Bacterial growth and resource allocation are tightly regulated, with ribosomal content reflecting and constraining the achievable growth rate under given nutrient and translational conditions. In particular, the RNA/protein ratio r, often used as a proxy for ribosome mass fraction, shows a well-established linear relationship with the bacterial growth rate λ under nutrient-limited or translation-inhibited conditions

(see Figure 3.1) [189]. This coupling is described by two distinct empirical growth laws previously outlined in (3.1) and (3.2), where κ_T and κ_N represent the translational and nutritional capacities of the cell, respectively. To mechanistically capture the impact of antibiotics on bacterial physiology, a minimal model (3.3) was previously developed in which ribosomes bind reversibly to intracellular antibiotic [71]. The system tracks the intracellular antibiotic concentration a, the unbound ribosomes r_u, and antibiotic-bound ribosomes r_b, while the growth rate λ and ribosomal synthesis rate $s(\lambda)$ are constrained by physiological laws described in the previous chapter.

In a subsequent study, the steady-state framework developed previously [71] was extended to a dynamic regime incorporating time-dependent antibiotic exposure [72]. Specifically, a fixed total antibiotic dose $S \times T = 4 \times \mathrm{IC}_{50}$ is delivered by varying either the concentration S or duration T. The rationale for maintaining a fixed total dose stems from the pharmacodynamic distinction between concentration-dependent and time-dependent antibiotics. For concentration-dependent antibiotics such as aminoglycosides (for example, streptomycin, which binds to the small 16S rRNA, causing codon misreading and inhibition of protein synthesis), efficacy correlates with the peak concentration ($C_{\max}$), where brief high doses yield maximal killing efficiency. On the other hand, for time-dependent or reversible antibiotics such as tetracycline and chloramphenicol (for example, tetracycline limits amino acid formation by blocking the A-site), efficacy depends primarily on the area under the concentration–time curve (AUC) rather than the instantaneous concentration [105]. In such cases, bacterial inhibition is controlled by the cumulative exposure that determines the total time the intracellular antibiotic concentration exceeds the effective inhibitory level.

Holding $S \times T$ constant thus provides a managed framework to distinguish between concentration- and exposure-driven effects while certifying that total antibiotic burden remains equivalent across dosing regimens. This comparison allows systematic understanding of how bacteria respond to identical cumulative antibiotic exposures distributed over different temporal profiles, like short, high-intensity pulses versus long, low-intensity treatments. This isolates the physiological impact of exposure length from total antibiotic quantity, a contrast that is necessary for linking theoretical pulse-dose predictions to experimentally measurable outcomes such as delay time and recovery rate. Under this strategy, model predictions showed a temporary increase in growth rate after antibiotic removal, referred to as a "growth rate overshoot", caused by a transient surplus of free ribosomes following antibiotic dissociation when the system is closed under the ribosome-limited assumption described in (3.3). While this model captures key features of antibiotic inhibition, it assumes that ribosome content controls growth rate at all times, including after antibiotic removal. During post-antibiotic recovery, ribosomes are no longer growth-limiting, rather,

growth depends on proteome reallocation and metabolic rebalancing. To address this limitation, a corrected model was formulated that incorporates distinct growth constraints across three separate phases

1. **Pre-Pulse:** Before the antibiotic is applied, growth proceeds under the translational limitation regime $\lambda = \kappa_T(r_u - r_{\min})$, where synthesis follows (3.6).

2. **During Pulse:** The antibiotic is applied at a fixed extracellular concentration

$$a_{\text{ex}} = \frac{K \cdot \text{IC}_{50}}{T},$$

for a pulse duration of T (units of time, hours h), where K (units of time, hours h) represents the effective intensity of the applied dose. The product $K \cdot \text{IC}_{50}$ thus corresponds to the total antibiotic exposure, or area under the concentration–time curve (AUC) [105], maintained constant across simulations. Under this definition, the inhibited growth rate during the pulse is

$$\lambda_f = \frac{\lambda_0}{1 + K/T}.$$

This formulation provides a convenient way to express a_{ex} when the goal is to keep the AUC constant among simulations, thereby ensuring that dose intensity remains comparable across pulse durations while avoiding dependence on literature-specific scaling choices.

3. **Post-Pulse:** Once the antibiotic is removed ($a_{\text{ex}} = 0$), growth follows the kinetic regime $\lambda = \kappa_N(r_{\max} - r_{\text{total}})$, and synthesis obeys

$$s(\lambda) = \lambda\left(r_{\min} + \frac{\lambda}{\kappa_T}\right).$$

The synthesis rate is therefore expressed as a function of the available ribosome pool required to sustain a given metabolic flux.

This revised model eliminates the growth rate overshoot observed in the original model, better reflecting the physiological constraints of proteome reallocation during recovery. The experimental design of the antibiotic pulse-dosing protocol, particularly the measurements of RNA and protein, was motivated by these model predictions, with the goal of quantitatively capturing cellular recovery dynamics in response to translational inhibition.

4.2.4 RNA and Protein Quantification

RNA Quantification

Total RNA was quantified using perchloric acid-based extraction [15]. At each time point, 1.5 mL of culture was collected in a 2 mL microcentrifuge tube and centrifuged at maximum speed (17,000×g) for 1 minute at 4°C. The supernatant was saved to correct for loss during final RNA quantification. The cell pellet was resuspended in 750 μL of cold 0.7 M $HClO_4$ and vortexed vigorously to ensure full lysis. After centrifugation (17,000×g) for 5 minutes at 4°C, the supernatant was discarded, while avoiding disturbing the pellet. The pellet was then incubated in 300 μL of 0.3 M KOH at 37°C for 60 minutes with occasional mixing to hydrolyze the RNA.

Following hydrolysis, 100 μL of cold 3 M $HClO_4$ was added to the extract, vortexed briefly, and centrifuged at maximum (17,000×g) for 3 minutes. The resulting supernatant (400 μL) was transferred to a fresh 2 mL tube. The remaining pellet was washed twice using 550 μL of cold 0.5 M $HClO_4$, collecting 550 μL and 560 μL supernatants, respectively, and combining both with the initial 400 μL supernatant to a combined volume of 1.5 mL. The combined extract was gently vortexed and centrifuged at maximum (17,000×g) for 5 minutes to remove any remaining precipitate. RNA abundance was determined by measuring the absorbance of the clarified supernatant at 260 nm. Final RNA concentration was calculated using the equation

$$\mathrm{RNA}\left(\frac{\mu\mathrm{g}}{\mathrm{mL}\cdot\mathrm{OD}_{600}}\right) = \frac{A_{260}\times 31}{\mathrm{OD}_{600}-\mathrm{OD}_{600}^{\mathrm{supernatant}}}, \tag{4.2}$$

where the factor 31 derives from the molar extinction coefficient for RNA in *E. coli* (10.5 $\mathrm{mmol}^{-1}\cdot\mathrm{cm}^{-1}$) and an average molecular weight of 324 per nucleotide.

Protein Quantification

Total protein content was measured using the Biuret method [79]. At each time point, 1.5 mL of culture was collected into a 2 mL microcentrifuge tube and centrifuged at maximum speed (17,000×g) for 1 minute. The supernatant was discarded into a waste tube (W2B), set aside to correct for loss. The pellet was washed with 1 mL of cold phosphate-buffered saline (PBS), gently resuspended, and centrifuged at maximum (17,000×g) for 2 minutes. The supernatant was collected into a second waste tube (W1), also set aside to correct for loss. To recover the protein sample, the pellet was resuspended in 200 μL of PBS, then transferred to a clean, labeled sample tube. An additional 500 μL of PBS was

added to the original waste tube, vortexed briefly to wash residual material, and transferred to a third waste tube (W2A).

For protein quantification, 100 μL of 3 M NaOH was added to each sample, vortexed, and incubated at 100°C for 5 minutes. Samples were cooled to room temperature, and 100 μL of 1.6% $CuSO_4$ solution was added. After vortexing briefly and standing at room temperature for 5 minutes, samples were centrifuged for 3 minutes at maximum speed (17,000×g). Protein concentration was determined by measuring absorbance at 555 nm and referencing a bovine serum albumin (BSA) calibration curve (using a stock solution of 2 mg/mL). A correction for sample loss and dilution was applied

$$p\left(\frac{\mu\text{g}}{\text{mL}\cdot\text{OD}_{600}}\right) = \frac{\text{sample conc. (mg/mL)}}{\text{OD}_{600} - \text{OD}_{600}^{\text{W1}} - \text{OD}_{600}^{\text{W2A}}} \times \frac{1000}{7.5}, \tag{4.3}$$

where the denominator accounts for cell loss during centrifugation steps (W1 and W2A supernatant tubes), and 7.5 reflects the dilution factor based on sample preparation.

Protocol Modifications for Low-OD Samples

For RNA and protein samples collected when the culture density was too low for standard processing ($\text{OD}_{600} < 0.5$), the sample volume was doubled to ensure adequate biomass. Two 1.5 mL aliquots of culture were collected and centrifuged separately. One pellet was resuspended in 1.0 mL of PBS, and the contents were transferred into the second tube to combine both pellets. The resulting mixture (containing approximately twice the cell content) was then processed following the standard RNA or protein quantification protocols above. OD corrections were adjusted to account for both collection volumes and the combined waste measurements.

4.2.5 Experimental Data Summary

The following tables summarize the experimental measurements used for model calibration and validation. Each dataset reflects the mean of at least two independent biological replicates. Inhibition curve growth measurements in Table 4.1, delay times are shown in Table 4.2, and RNA/protein ratios in Table 4.3.

Carbon Source	Tetracycline (μM)	Growth rate $\lambda \pm \sigma$ (h^{-1})	$IC_{50} \pm \sigma$ (μM)	Repeats
▼ Glucose	0.0	0.62±0.01	1.01±0.06	3
	0.4	0.46±0.02		3
	0.8	0.35±0.01		3
	1.2	0.33±0.02		3
	1.6	0.18±0.02		3
	2.0	0.15±0.09		3
▼ Glycerol	0.0	0.40±0.02	1.31±0.15	3
	0.4	0.32±0.02		3
	0.8	0.23±0.02		3
	1.2	0.23±0.01		3
	1.6	0.13±0.04		3
	2.0	0.12±0.04		3

Table 4.1: Inhibition curve growth rate data at multiple tetracycline concentrations.

Carbon Source	T (h)	Delay $\Delta t \pm \sigma$ (h)	Repeats
■ Glucose	2	2.58±0.01	3
	4	3.47±0.00	2
	5	3.66±0.00	2
	6	4.44±0.02	2
	8	3.61±0.01	2
	10	3.11±0.02	2
■ Glycerol	4	2.88±0.01	2
	6	2.72±0.01	2
	8	2.86±0.01	2
	10	3.03±0.01	2

Table 4.2: Delay time measurements across pulse durations T for glucose and glycerol.

Carbon Source	Phase	t (h)	RNA/P $\pm$ σ (unitless)	Repeats
● Glucose	Pre-Pulse	0.50	1.000±0.20	3
	Pulse	1.75	1.396±0.35	3
	Pulse	2.50	1.489±0.40	3
	Pulse	3.25	2.150±0.65	3
	Pulse	4.00	2.161±0.92	3
	Pulse	4.75	2.164±0.74	3
	Post-pulse	5.50	3.205±1.10	3
	Post-pulse	6.00	2.530±1.53	3
	Post-pulse	6.50	1.538±0.50	3
● Glycerol	Pre-Pulse	0.50	1.000±0.24	2
	Pulse	1.75	1.571±0.29	2
	Pulse	2.50	1.949±0.37	2
	Pulse	3.25	1.907±0.41	2
	Pulse	4.00	2.410±0.66	2
	Pulse	4.75	2.743±0.90	2
	Post-pulse	5.50	2.926±1.00	2
	Post-pulse	6.00	2.437±0.96	2
	Post-pulse	6.50	2.024±0.70	2

Table 4.3: Normalized RNA/Protein ratios measured across experimental phases for a pulse of length $T = 4\,h$, with timepoints (from experiment start $t = 0\,h$), for glucose and glycerol conditions. All experimental data are normalized via their pre-pulse value (at $t = 0.5\,h$).

4.3 Mathematical Methods

With the experimental design established, the next objective is to develop a mathematical structure that is able to capture the dynamics of bacterial growth under antibiotic pulse dosing. The modeling approach reflects the physiological features built into the experimental design, including nutrient-dependent growth rates, translation inhibition, and recovery following antibiotic removal. This section details the model development, numerical methods, and parameter estimation procedures used to quantitatively connect the model with experimental measurements of optical density, RNA, and protein content. These methods provide the basis for the analyses presented in Chapter 5.

The pulse-dose experiments described in Subsection 4.2.3 were guided by a dynamical model of ribosome–antibiotic interactions constrained by empirical growth laws. While the full rationale and formulation of the model have been presented as part of the experimental design, this section focuses on the computational implementation of the model. The following subsections detail the model implementation, numerical solvers, optimization procedures for model fitting, sensitivity analyses, and error propagation methods used to compare model projection with experimental data.

4.3.1 Physiological Constraints and Model Assumptions

The mathematical model used in this thesis tracks the intracellular dynamics of reversible ribosome–antibiotic binding and antibiotic transport, governed by the ODE system in (3.3). Growth rate λ and ribosome synthesis $s(\lambda)$ are constrained by the two empirical linear growth laws introduced in Section 3.1, the translation-limited branch $\lambda = \kappa_T(r_u - r_{\min})$ (3.1) and the nutrient-limited branch $\lambda = \kappa_N(r_{\max} - r_{\text{total}})$ (3.2). The steady-state mass balance closure linking synthesis to growth

$$s(\lambda) = \lambda\left(r_{\min} + \frac{\lambda}{\kappa_T}\right)$$

is given in (3.6) and determines $s(\lambda)$ during each phase of the pulse experiment. In the original formulation [71], the system is closed by assuming that growth rate is always proportional to the abundance of unbound ribosomes r_u. This assumption remains valid during the pre-pulse and pulse phases, where growth follows the translation-limited law (3.1). However, during post-antibiotic recovery this closure is no longer physiologically appropriate.

As shown in Subsection 3.1.1, once the antibiotic is removed the cell no longer operates in a translation-limited regime. Although the free ribosome pool remains elevated, growth cannot immediately accelerate because amino acid supply limits the achievable synthesis rate. Accordingly, the model switches to the nutrient-limited growth law (3.2) immediately after $a_{\text{ex}} = 0$, while synthesis remains governed by the same mass balance relation (3.6). This phase-specific assignment of λ and $s(\lambda)$ creates the piecewise but continuous model used in all simulations. It eliminates the unphysical growth rate overshoot generated by the original translation-limited closure and aligns model behaviour with experimental observations of proteome reallocation during recovery.

4.3.2 Model Simulation

The corrected model (described in Subsection 4.2.3) was numerically implemented to simulate growth rate dynamics under pulse-dose antibiotic exposure. The system of differential equations (3.3), which tracks the intracellular antibiotic concentration $a(t)$ and ribosomal pools $(r_u(t), r_b(t))$, was solved using Python's `solve_ivp` from `scipy.integrate` with the BDF method. The BDF (backward differentiation formula) is a family of implicit, multi-step stiff solvers well suited for problems in which fast and slow processes coexist. In this model, rapid binding/unbinding of ribosomes and antibiotic influx/efflux occurs on much shorter timescales than proteome reallocation and growth rate adjustment, producing stiffness in the ODE system. BDF therefore provides stable, accurate integration across long pulse durations and across the instantaneous regime shifts imposed by the piecewise growth laws. Integration tolerances were set to $\texttt{rtol} = 10^{-6}$ and $\texttt{atol} = 10^{-9}$. Growth rate $\lambda(t)$ was assigned according to the ribosome-limited law $\lambda = \kappa_T(r_u - r_{\min})$ before and during the pulse interval and the nutrient-limited law $\lambda = \kappa_N(r_{\max} - r_{\text{total}})$ after antibiotic removal, following the corrected framework in Subsection 4.2.3.

To compare model output with experimental OD_{600} data, the time-dependent growth rate was converted into simulated optical density. Assuming OD is proportional to biomass and biomass follows exponential growth, the logarithm of OD obeys

$$\ln[\text{OD}(t)] = \ln[\text{OD}_0] + \int_0^t \lambda(t')\, dt'.$$

Thus, numerical integration of $\lambda(t)$ determines the log-OD trajectory up to an additive constant. These simulated log-OD curves were then used to compute the model-predicted delay time Δt by applying linear fits to the pre- and post-pulse log-OD segments (both constrained to slope λ_0) and evaluating the difference between their x-intercepts, matching the method used for experimental quantification. The model simulates the total ribosome concentration $r_{\text{total}}(t) = r_u + r_b$, which is compared to experimentally measured RNA/protein ratios following the normalization procedure described in Section 4.1. Each simulation requires specification of the pulse duration T, the extracellular antibiotic concentration $a_{\text{ex}} = \frac{K \cdot \text{IC}_{50}}{T}$, and a parameter set $(k_{\text{off}}, k_{\text{on}}, P_{\text{in}}, P_{\text{out}})$. These parameters were varied to explore their influence on growth rate behaviour and the quantities of interest (Δt, ρ, and IC_{50}). IC_{50} was computed directly from the steady-state susceptibility relation (3.10) and included in all optimization and sensitivity procedures (Subsection 4.3.4, Subsection 4.3.5), ensuring that susceptibility remained analytically linked to the kinetic and physiological structure of the model.

4.3.3 Parameter Initialization and Bounds

The four variable parameters in the model were the ribosome–antibiotic dissociation rate (k_{off}), association rate (k_{on}), and the cellular inward and outward permeability rates (P_{in}, P_{out}). These four quantities dictate both intracellular antibiotic accumulation and ribosome binding dynamics. Initial guesses for these parameters were based on values from [72]. During iterative rounds of optimization, these initial guesses were refined based on previously obtained optimal parameter sets. When convergence stalled or optimization became trapped in suboptimal regions or at range endpoints, initial guesses were perturbed using Gaussian noise to promote broader exploration of the parameter space.

Parameters were constrained within logarithmic bounds, whose values were referred from the supplementary data of [71], originally derived from literature ranges for tetracycline

$$\begin{aligned} 10^2 \le k_{\text{off}} \le 10^6, &\qquad (h^{-1}) \\ 10^1 \le k_{\text{on}} \le 10^4, &\qquad (\mu\text{M}h)^{-1} \\ 10^1 \le P_{\text{in}} \le 10^4, &\qquad (h^{-1}) \\ 10^1 \le P_{\text{out}} \le 10^4. &\qquad (h^{-1}) \end{aligned}$$

In cases where optimizers failed to converge or produced boundary-biased results, these bounds were widened further. In all optimization runs, the four core parameters were varied independently. Additionally, it was assumed that k_{off} and k_{on} were invariant across carbon sources, while P_{in} and P_{out} were allowed to differ between glucose ($P_{\text{in}}^{\text{GLU}}$, $P_{\text{out}}^{\text{GLU}}$) and glycerol ($P_{\text{in}}^{\text{GLY}}$, $P_{\text{out}}^{\text{GLY}}$) conditions. The fixed physiological parameters used in all simulations were the minimum ribosome concentration $r_{\min} = 5.4\,\mu$M, the maximum ribosome concentration $r_{\max} = 54.4\,\mu$M, their difference $\Delta r = r_{\max} - r_{\min} = 49.0\,\mu$M, translational capacity $\kappa_T = 0.058\,(\mu\text{M}h)^{-1}$, and drug-free growth rates $\lambda_0 = 0.64\,h^{-1}$ for glucose and $\lambda_0 = 0.40\,h^{-1}$ for glycerol. The nutrient capacity κ_N (with units $(\mu\text{M}h)^{-1}$) was computed from λ_0 using the following expression

$$\kappa_N = \left[\Delta r \left(\frac{1}{\lambda_0} - \frac{1}{\kappa_T \Delta r}\right)\right]^{-1}.$$

The parameters $r_{\min}$, $r_{\max}$, and κ_T were obtained by combining per-cell data with cell-volume measurements to estimate ribosome concentration as a function of growth rate. Linear regression of ribosome concentration versus growth rate yielded the intercepts $r_{\min}$ and $r_{\max}$ and the inverse slope $1/\kappa_T$, consistent with (3.1) [189]. Ribosome abundance data were taken from Table 3 of [26], and cell-volume data from the supplementary material

of [12]. Drug-free growth rates λ_0 for both glucose and glycerol, and the subsequent calculation of κ_N follow from [71]. These values fall within the physiological range reported in those studies and ensure biological consistency across nutrient conditions.

4.3.4 Sensitivity Analysis

The general modality for sensitivity and Hessian analysis is described in Chapter 3.3. Here the exact finite-difference implementation used in this thesis is specified. Sensitivities were computed using the logarithmic form

$$S_i = \frac{\partial \ln f(\boldsymbol{p})}{\partial \ln p_i} = \frac{p_i}{f(\boldsymbol{p})} \frac{\partial f(\boldsymbol{p})}{\partial p_i}, \tag{4.4}$$

where f represents a model output and p_i the perturbed parameter. Each parameter was perturbed individually by $\epsilon = 0.1\%$ around its baseline value. Second-order sensitivities were assessed through the Hessian, defined as

$$H_{ij} = \frac{\partial^2 \ln f(\boldsymbol{p})}{\partial \ln p_i \, \partial \ln p_j} = \frac{\partial S_i}{\partial \ln p_j}. \tag{4.5}$$

The Hessian was estimated numerically using central finite differences with a perturbation size of $\epsilon = 0.1\%$, chosen to be small enough to approximate local linearity while large enough to suppress numerical noise. Although central differencing can amplify instability in stiff ODE sensitivity calculations, it remains stable and accurate here because it is applied to the cost function gradients rather than to direct model integrations. Eigenvalues of the resulting matrices were analyzed to evaluate stiffness and parameter identifiability. Applications of this framework to specific outputs and parameters are presented in Section 5.5.

4.3.5 Optimization Procedures

The refined model incorporates multiple variable parameters, including the binding kinetics of the antibiotic ($k_{\text{off}}, k_{\text{on}}$). It also includes permeability rates into and out of the cell, ($P_{\text{in}}^{\text{GLU}}, P_{\text{out}}^{\text{GLU}}$) and ($P_{\text{in}}^{\text{GLY}}, P_{\text{out}}^{\text{GLY}}$), all of which must be estimated to best fit the experimental data. Optimization was performed to minimize discrepancies between experimental and simulated quantities of interest (Δt, ρ, and IC_{50}) measured for both glucose and glycerol conditions. The cost function used for optimization was defined as the sum of weighted

mean squared errors (WMSE, (3.16)), where weights were derived from experimental uncertainty along replicates

$$\text{Cost} = \text{WMSE}(\Delta t) + \text{WMSE}(\rho) + \text{WMSE}(\text{IC}_{50}).$$

Each term in the cost function was determined using inverse-variance weighting. For RNA/protein ratio, standard deviations were calculated by propagating relative error from the independently measured RNA and protein concentrations. Delay time standard deviations were determined directly from variability in biological replicates. For inhibition curve fitting, normalized growth rates at each tetracycline concentration were computed as λ/λ_0, with propagated uncertainty as done with RNA/protein ratio measurements. This ensured that data points with higher confidence contributed more strongly to the optimization.

Each term in the cost function was weighted using inverse-variance weighting based on experimental uncertainty, ensuring that data with higher reliability contributed more strongly to parameter estimation. For the RNA/protein ratio ρ, standard deviations were computed by propagating the relative errors in RNA and protein concentrations

$$\sigma_\rho = \rho \sqrt{\left(\frac{\sigma_{\text{RNA}}}{\text{RNA}}\right)^2 + \left(\frac{\sigma_{\text{P}}}{\text{P}}\right)^2}.$$

Uncertainty in the normalized RNA/protein ratio (ρ_i/ρ_0, where $i \in [0, 6]$ denotes a phase-dependent timepoint and index 0 represents the pre-pulse measurement) was computed using

$$\sigma_{\rho_i/\rho_0} = \left(\frac{\rho_i}{\rho_0}\right) \sqrt{\left(\frac{\sigma_{\rho_i}}{\rho_i}\right)^2 + \left(\frac{\sigma_{\rho_0}}{\rho_0}\right)^2}.$$

For inhibition curve fitting, normalized growth rate was calculated as λ/λ_0, and the corresponding propagated standard deviation was given by

$$\sigma_{\lambda/\lambda_0} = \left(\frac{\lambda}{\lambda_0}\right) \sqrt{\left(\frac{\sigma_\lambda}{\lambda}\right)^2 + \left(\frac{\sigma_{\lambda_0}}{\lambda_0}\right)^2}.$$

The optimization procedure was carried out using the Nelder–Mead simplex algorithm via `scipy.optimize.minimize`, as it provided consistent convergence and flexibility in handling the non-convex nature of the cost function. Initial parameter guesses were selected based on literature values reported in [72], with additional guidance from model sensitivity analysis. To minimize the risk of convergence to local minima or maxima, the optimizer was run multiple times with randomized initial guesses drawn from Gaussian

perturbations centered on previous best-fit values. Parameter bounds were defined logarithmically, following the experimentally justified ranges stated above. These bounds were widened repeatedly if the optimizer failed to converge or if output quantities showed poor fits against experimental data. For all optimization runs, k_{off} and k_{on} were assumed to be shared between glucose and glycerol, while P_{in} and P_{out} were allowed to vary independently between carbon sources (($P_{\text{in}}^{\text{GLU}}, P_{\text{out}}^{\text{GLU}}$) and ($P_{\text{in}}^{\text{GLY}}, P_{\text{out}}^{\text{GLY}}$)). Together, these constraints defined the complete optimization framework used to generate all model fits presented in subsequent sections.

Chapter 5

Results

5.1 Overview of Modeling Goals and Strategy

Pulsed antibiotic treatments disrupt bacterial growth and recovery, with recovery times varying across nutrient environments and drug exposures. While the original model (3.3) reproduced steady-state inhibition trends, it predicted an unexpected post-pulse growth rate overshoot inconsistent with physiological constraints. The model assumes that ribosomes remain the sole growth-limiting factor throughout the pulse. However, once ribosome levels increase, amino acid supply and metabolic precursor availability become limiting, preventing continued translational control during post-antibiotic recovery. This discrepancy motivated the introduction of physiological refinements and direct experimental validation. The revised mathematical model thus aims to reproduce realistic recovery dynamics and evaluate its predictions against growth and proteomic measurements. To preserve clarity and biological realism, a bottom-up revision approach was used, adjusting only model elements contradicted by data or established physiology. The model is evaluated against three experimentally measured readouts. These include the delay time (Δt), which quantifies recovery duration across all pulse lengths and carbon sources, the RNA/protein ratio (ρ), which provides a coarse-grained estimate of ribosome allocation and is measured before, during, and after each pulse, and growth-inhibition curves, which quantify effective antibiotic potency through IC_{50} values measured over six tetracycline concentrations. Each dataset contains two biological replicates per condition, with full experimental procedures described in Section 4.2. Together, these measurements define both the structure and parameterization of the model and form the basis for the fitting and sensitivity analyses presented in this chapter.

The model evolved through successive refinements, motivated by discrepancies between simulation and experiment and guided by sensitivity analyses. First, the post-pulse translational growth constraint was replaced with a metabolic one, illustrating that after antibiotic removal, amino acid availability and metabolic enzyme levels, rather than unbound ribosome abundance, limit growth recovery. This correction prevented simulated growth from exceeding the drug-free rate and aligned the model with physiological resource allocation principles. Then phase-dependent growth switches were incorporated to represent transitions between translation-limited and metabolism-limited regimes, ensuring that synthesis rate and growth responded dynamically to internal state variables rather than remaining fixed at steady-state values. Each refinement was introduced to address quantitative mismatches between simulation and experiment and to reproduce the experimentally observed trajectories more accurately.

5.2 Initial Corrections and Experimental Characterization

As described in Subsection 3.1.1, the first model correction eliminated the implausible post-pulse growth overshoot by replacing the limiting factor from translational capacity $\kappa_T(r_u - r_{\min})$ (3.1) to metabolic capacity $\kappa_N(r_{\max} - r_{\text{total}})$ (3.2) once the antibiotic was removed. This adjustment ensured that the recovery trajectory did not exceed the drug-free growth rate, maintaining consistency with known physiological limits (see Figure 3.3). Preliminary simulations confirmed the effectiveness of this change in constraining post-pulse behaviour (see Figure 5.1A, D). To examine how growth recovery depends on nutrient quality and pulse length, pulse-dose antibiotic experiments were conducted with *E. coli* grown in MOPS minimal medium supplemented with either glucose or glycerol. Tetracycline, the ribosome-targeting antibiotic, was administered during mid-exponential phase across a range of pulse durations, and OD_{600} was continuously monitored to track growth across all phases of the antibiotic pulse (see Subsection 4.2.2). Δt was computed as the horizontal displacement between the pre-pulse and post-pulse growth trajectories, measured at the OD threshold where exponential regrowth resumed. Growth recovery time increased with pulse duration for both carbon sources, following a nonlinear trend that saturated for pulses longer than approximately 8 hours. While the original steady-state model (3.3) generated only qualitative recovery behaviour, the optimized corrected model, incorporating the metabolic growth constraint, quantitatively captured recovery across nutrient conditions.

Experimentally, cells grown on glycerol appeared to recover faster than those grown on glucose, whereas the original formulation predicted the opposite trend. This apparent discrepancy arises because the total inhibitory exposure, proportional to the product $K \cdot \mathrm{IC}_{50}$, differs across nutrient conditions. Under glycerol growth, the smaller IC_{50} value produces a lower effective pulse area, yielding a milder inhibitory challenge. When the exposures are normalized to equivalent pulse areas, the model correctly reproduces slower recovery for glycerol-grown cells, consistent with their reduced metabolic capacity. To complement the growth recovery data, inhibition curves were measured for *E. coli* grown in glucose and glycerol minimal media. These revealed IC_{50} values of 1.01 μM and 1.31 μM, respectively, obtained by fitting growth-rate trajectories across a range of tetracycline concentrations. These measured values are slightly lower than those reported previously (1.75 μM for glucose and 1.45 μM for glycerol) [71]. All experimental pulse concentrations were calculated using the literature IC_{50} values to ensure methodological consistency with prior studies. The discrepancy observed afterward likely reflects minor differences in strain background, media composition, or antibiotic stock calibration, resulting in slightly greater effective inhibition in our experimental system. For this reason, model simulations were scaled to the reference IC_{50} values from [71], while comparisons and parameter fitting were performed relative to the experimentally measured inhibition curves.

ρ measurements were also obtained at defined pulse durations to characterize internal physiological states during and after antibiotic challenge. As a proxy for ribosome abundance, ρ increased during the pulse in both nutrient conditions, reflecting the accumulation of inactive, drug-bound ribosomes as antibiotic entered the cell and sequestered active ribosomes. Following this peak, ρ gradually declined toward its steady-state level as translation resumed and ribosome synthesis rebalanced toward pre-pulse proportions. These experimental observations provided quantitative benchmarks for model validation and guided parameter refinement during fitting, ensuring that simulated inhibition curves, Δt, and ρ dynamics aligned with experimental behaviour across both pulse and recovery phases.

5.3 Model Fitting and Optimization Framework

5.3.1 Early Fitting Attempts and Challenges

Initial model fitting efforts aimed to reproduce the experimental Δt, ρ, and IC_{50} data across both carbon sources. The inhibition curve fits were reasonably close to the measured values (see Figure 5.1B, E). However, while steady-state inhibition was reproduced, the

resulting physiological dynamics diverged from experimental observations. Even with an optimal parameter set, the model consistently overestimated delay times at intermediate pulse lengths (see Figure 5.1G), while the predicted RNA/protein ratio ρ reproduced qualitative trends but exhibited slower rise and decay dynamics than observed experimentally (see Figure 5.1C, F). The dominant discrepancy therefore arose from the delay time behaviour, indicating that while the model captured steady-state inhibition accurately, it did not reproduce the transient redistribution of ribosomes that governs recovery kinetics.

To better understand the behaviour of Δt, the relationship between recovery time and pulse duration was derived analytically. This analysis demonstrates that the model inherently predicts a saturating recovery limit as exposure length increases. Let $N(t)$ denote the bacterial population, which is proportional to the measured optical density (OD_{600}). For exponential growth, the time derivative of the logarithmic population, $X(t) = \ln N(t)$, equals the instantaneous growth rate,

$$\frac{dX}{dt} = \lambda(t).$$

Thus, $X(t)$ provides a convenient linear representation of exponential growth, with slope $\lambda(t)$. For a drug-free condition where $\lambda(t) = \lambda_0$, the trajectory is

$$X_{\text{drug-free}}(t) = X_0 + \lambda_0 t,$$

where X_0 is the logarithmic initial density. During antibiotic exposure, the instantaneous growth rate $\lambda(t)$ becomes time-dependent and reduced relative to λ_0. Over a pulse of duration T, the inhibited trajectory accumulates growth according to

$$X_{\text{pulse}}(T) = X_0 + \int_0^T \lambda(t)\, dt.$$

After antibiotic removal, the population resumes drug-free growth at rate λ_0 but lags behind the unperturbed reference trajectory by a constant horizontal offset, Δt, corresponding to the recovery delay. This alignment can be expressed as

$$X_{\text{pulse}}(t) = X_{\text{drug-free}}(t - \Delta t), \qquad t \geq T.$$

At the moment of antibiotic removal ($t = T$), the difference between the perturbed and unperturbed trajectories satisfies

$$X_0 + \int_0^T \lambda(t)\, dt = X_0 + \lambda_0 (T - \Delta t).$$

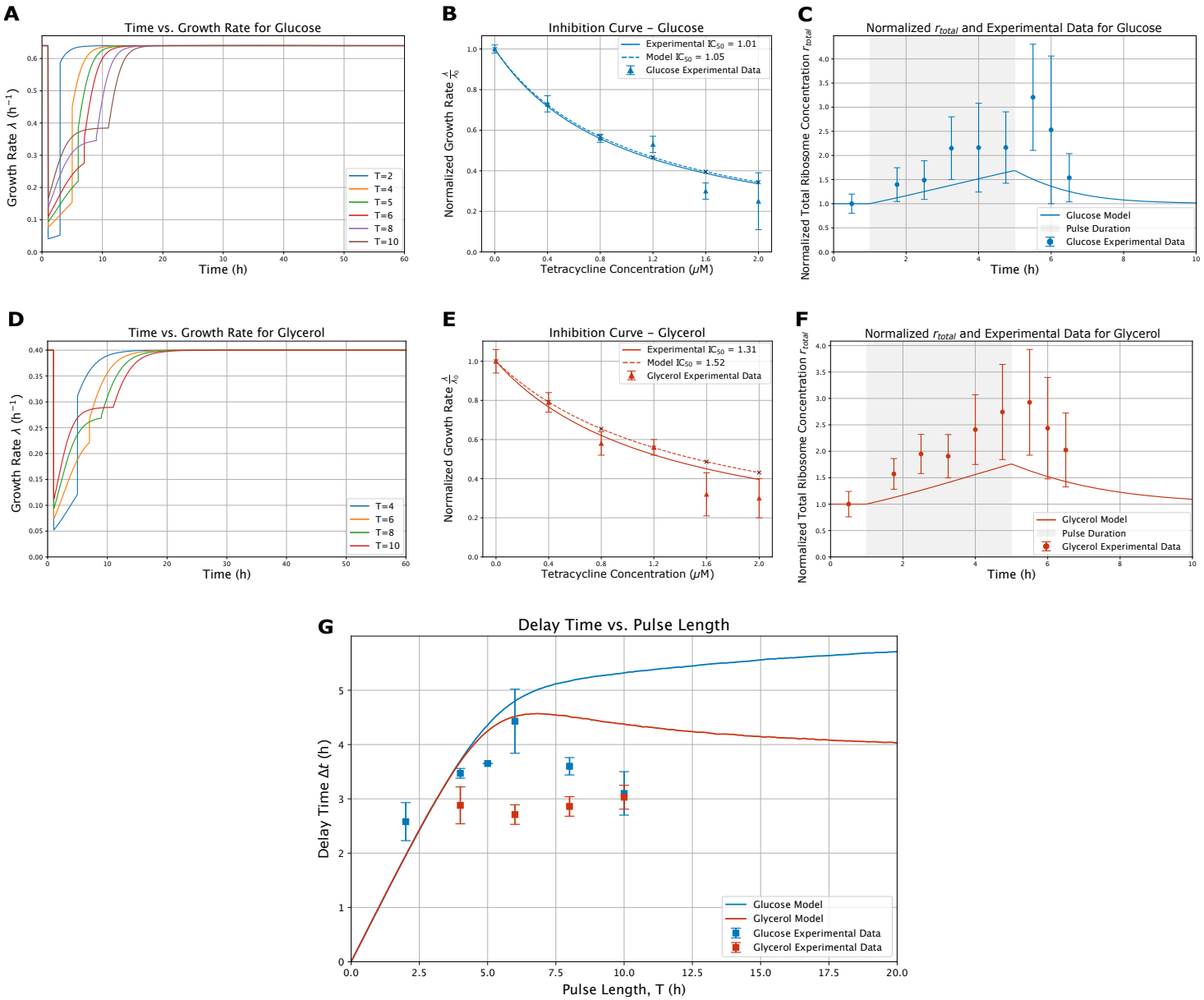


Figure 5.1: Initial corrected model fits to experimental data for glucose and glycerol conditions. (A–C) Glucose; (D–F) Glycerol. Each panel compares simulated and measured growth, inhibition, and RNA/protein ratio trajectories across pulse durations ($T = 2$–$10\,h$), respectively. (G) Δt as a function of pulse length shows nonlinear saturation beyond $8\,h$. The corrected model removed the post-pulse overshoot and reproduced steady-state inhibition but continued to overestimate Δt and partially mimic ρ dynamics, with the rise during antibiotic exposure occurring too slowly and the post-pulse decline also proceeding too slowly compared to experimental trajectories. This motivated further model refinements.

Rearranging gives the general expression for the delay time

$$\Delta t = \frac{1}{\lambda_0} \int_0^T [\lambda_0 - \lambda(t)]\, dt. \tag{5.1}$$

This integral represents the cumulative growth deficit that accumulates during antibiotic exposure relative to unperturbed conditions. It assumes that OD_{600} is proportional to cell density within the measured range, and that post-pulse growth resumes with the same slope λ_0, so Δt corresponds directly to the horizontal separation between the two growth trajectories (see Figure 4.1).

To evaluate the asymptotic behaviour of $\Delta t(T)$, $\lambda(t)$ is approximated as piecewise constant. The steady-state growth rate switches between three regimes, λ_0 before the pulse, λ_f during the pulse, and λ_0 again after antibiotic removal, representing distinct physiological states. This piecewise exponential assumption is justified because, for sufficiently long pulses, the short transient adaptation and recovery phases (see Figure 5.2) become negligible compared with the time spent at the inhibited steady-state rate λ_f. The system thus undergoes an abrupt transition between these regimes while remaining effectively exponential during the inhibited phase. During a pulse of length T, the inhibited steady-state growth rate λ_f follows

$$\lambda_f = \frac{\lambda_0}{1 + K/T},$$

which is consistent with the Langmuir-type inhibition relationship introduced earlier (3.11), describing steady-state growth suppression as a reversible binding process between intracellular antibiotic and ribosomes. Here, K (units of time, hours h) represents the effective antibiotic perturbation timescale that sets the degree of inhibition for a given total pulse duration. Substituting this constant inhibited rate into the general delay time expression (5.1) gives

$$\Delta t(T) = T \left(1 - \frac{\lambda_f}{\lambda_0}\right).$$

Replacing λ_f/λ_0 with $1/(1 + K/T)$ yields

$$\Delta t(T) = \frac{KT}{T + K}.$$

At long pulse durations, this expression approaches a finite limit

$$\lim_{T \to \infty} \Delta t(T) = K. \tag{5.2}$$

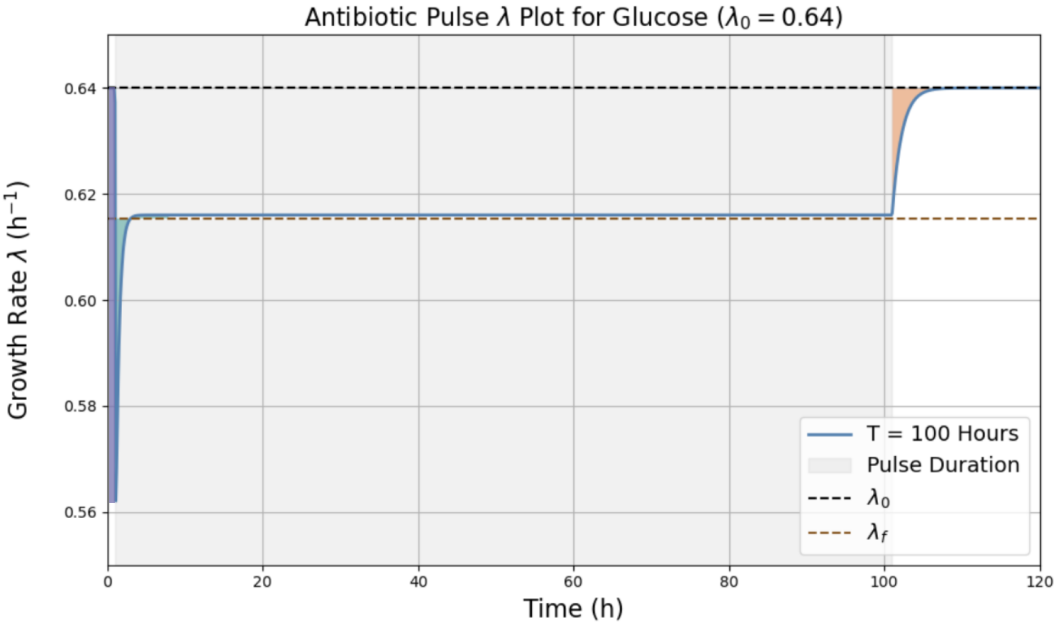


Figure 5.2: Piecewise growth regimes during a long pulse. Simulated growth rate $\lambda(t)$ under glucose conditions transitions through adaptation (purple, pre-pulse), inhibited steady state (teal, during pulse) where $\lambda(t) \to \lambda_f$, and recovery (orange, post-pulse) returning to λ_0. The grey band marks the pulse duration. Dashed lines indicate the drug-free growth rate λ_0 (black) and the inhibited growth rate λ_f (light brown). For sufficiently long pulses, the brief adaptation and recovery intervals are negligible relative to the time spent near λ_f, justifying the piecewise exponential approximation used to derive the delay time relation (5.1) and its saturation limit (5.2).

This result shows that Δt asymptotically saturates as pulse length increases. Physically, this arises because once ribosomes are maximally inhibited, extending the pulse further no longer increases the recovery deficit. The population can only fall as far behind as allowed by the steady-state inhibited growth rate λ_f. The constant K therefore defines the effective intensity of the applied pulse and sets the upper limit for Δt, representing the longest possible delay achievable under complete translational inhibition.

Early model fits reproduced the qualitative rise-to-saturation trend but systematically overestimated Δt for intermediate pulse durations. For ρ, the experimental trajectories showed a steady increase during the pulse, reflecting the accumulation of total ribosomes as antibiotic binding reduced translational activity. This was followed by a transient dip after

antibiotic removal as active translation resumed before returning to baseline. In contrast, the initially corrected model predicted only a small rise in ρ and failed to fit the transient post-pulse dip, omitting the dynamics observed experimentally. These discrepancies showed that the steady-state formulation of ribosome synthesis (3.6) could not reproduce the observed temporal structure of recovery because it enforced an instantaneous balance between synthesis and dilution, lacking an explicit kinetic term to represent rapid feedback when antibiotic concentration or translational demand changed. Thus, the model exhibited artificially slow dynamics, preventing it from responding on the timescale observed experimentally. Together, these results demonstrated that although the base model could fit inhibition curves through IC_{50}, it lacked the regulatory flexibility required to capture both the intermediate-pulse Δt and the transient rise-and-dip pattern of ρ. To identify the underlying source of this limitation, a local sensitivity analysis was performed to determine which processes most strongly influenced recovery dynamics (see Subsection 5.3.2). Full numerical results are provided in Table 5.1.

Parameter	Symbol	Glucose	Glycerol
Antibiotic Unbinding Rate	k_{off} (h^{-1})	6545.07	6545.07
Antibiotic Binding Rate	k_{on} $((\mu\text{M}h)^{-1})$	1400.38	1400.38
Antibiotic Influx Permeability (Into Cell)	P_{in} (h^{-1})	2433.26	2186.85
Antibiotic Efflux Permeability (Out of Cell)	P_{out} (h^{-1})	122.74	99.79

Table 5.1: Optimal parameters for the initial revised model under glucose and glycerol conditions.

5.3.2 Sensitivity Analysis of the Initially Corrected Model

To assess whether the structure of the initially corrected model limited its ability to reproduce the observed delay time RNA/protein trajectories, a local sensitivity analysis was performed. Sensitivities were computed using the finite-difference approach defined in Subsection 3.3.1, with each parameter perturbed by $\pm 10\%$ relative to its optimized value under glucose and glycerol conditions. The four kinetic and transport parameters, k_{on}, k_{off}, P_{in}, and P_{out}, were also recast into two composite parameters for interpretability, the dissociation constant $K_D = k_{\text{off}}/k_{\text{on}}$, which characterizes antibiotic affinity, and the permeability ratio $R_P = P_{\text{in}}/P_{\text{out}}$, which describes transport balance across the cell membrane.

For *E. coli* grown on glucose, the delay time exhibited moderate sensitivity to both K_D and R_P, with normalized indices on the order of $|S| \approx 0.005$–0.01 (Table 5.2). This outcome

aligns with the expectation that recovery time depends primarily on intracellular antibiotic accumulation and ribosome binding kinetics. In contrast, the peak RNA/protein ratio was effectively insensitive to all four parameters, with $|S| < 10^{-4}$ across all perturbations. A comparable pattern was obtained under glycerol growth, Δt remained weakly dependent on K_D and R_P ($|S| \approx 0.002$–0.01), whereas the peak ρ remained unchanged to within numerical precision ($|S| < 10^{-3}$).

Parameter	Symbol	Carbon Source	Sensitivity of Δt	Sensitivity of Peak ρ
Antibiotic Dissociation Constant	K_D	Glucose	0.006	$< 10^{-4}$
Cellular Permeability Ratio	R_P	Glucose	0.010	0.001
Antibiotic Dissociation Constant	K_D	Glycerol	0.003	$< 10^{-3}$
Cellular Permeability Ratio	R_P	Glycerol	0.008	0.006

Table 5.2: Representative normalized sensitivities of the delay time (Δt) and peak RNA/protein ratio (ρ) to the derived parameters $K_D = k_{\text{off}}/k_{\text{on}}$ and $R_P = P_{\text{in}}/P_{\text{out}}$, using $\pm 10\%$ perturbations around the optimized values. Values are reported for both glucose and glycerol conditions.

The negligible sensitivity of ρ to any of the core parameters demonstrates that the initially corrected model lacks the regulatory mechanism responsible for the transient rise and fall in total ribosome content observed experimentally. In this formulation, ribosome synthesis is defined through the steady-state relation $s = s^{SS}$, which enforces an instantaneous balance between synthesis and dilution. Consequently, the model cannot dynamically modulate ribosome production when translational activity or intracellular antibiotic concentration changes. Overall, these findings indicate that the inability of the initially corrected model to reproduce the experimentally observed ρ trajectories arises from a missing time-dependent regulation in ribosome synthesis rather than from parameter underestimation within the existing steady-state formulation.

5.3.3 Enhancing the Fitting Framework

Initial optimization efforts revealed persistent challenges in aligning the model with experimental data. Δt trajectories were systematically overestimated, ρ was only partially reproduced, and convergence showed little sensitivity to initial parameter values. These shortcomings motivated the development of a more stable and flexible fitting framework, designed to better reconcile the experimental targets and improve reproducibility. Two key modifications were introduced to strengthen numerical stability and biological consistency.

Weighted Cost Function. Each target variable (Δt, ρ, and IC_{50}) exhibited distinct variability, with IC_{50} generally being the most reliably fit quantity at this stage of model formulation. To account for this heterogeneity, the objective function was reformulated as a weighted mean squared error, applying relative multipliers to individual data sets. In practice, weights ($10\times$, $25\times$, or $50\times$) were adjusted to emphasize underfit or overfit variables Δt or ρ, without overfitting well-captured inhibition data. This weighting balanced the optimizer's focus across competing data types, improved convergence stability, and yielded more robust and reproducible parameter estimates.

Gaussian Perturbations. Even with weighting, convergence remained dependent on the chosen initial conditions. To improve exploration of parameter space, Gaussian perturbations were applied around the initial guesses, and optimization runs were repeated across randomized starting points. This stochastic approach allowed the optimizer to escape local minima and approach consistent global optima. Across multiple runs, parameter variability narrowed, confirming improved robustness and reproducibility of fitted results.

Together, these refinements produced a stable and reproducible fitting framework that reliably converged across initial conditions. Despite these improvements, the initially corrected model still showed little sensitivity of the peak RNA/protein ratio to any kinetic or transport parameter (see Subsection 5.3.2), indicating that the observed discrepancies in Δt and ρ could not be corrected by further parameter optimization alone. The fits presented in Figure 5.1 reproduced the general trends in growth inhibition but continued to overestimate Δt and underestimate ρ, revealing a structural limitation rooted in the steady-state ribosome synthesis formulation. Experimentally, the transient peak in ρ reflects an active regulatory response, translational inhibition triggers a temporary increase in ribosomal RNA synthesis through transcriptional feedback and ppGpp-mediated control, followed by suppression once growth resumes. Because this feedback is absent from the steady-state synthesis law $s = s^{SS}$, the model enforces instantaneous balance between synthesis and dilution and therefore fails to dynamically adjust ribosome production during antibiotic stress or recovery. This limitation reduces the quantitative accuracy of the fits, as the model fails to reproduce the experimentally observed rapid adaptive response in ribosome synthesis. These results motivated the next refinement, in which the synthesis rate was reformulated to include explicit time dependence and proportional feedback. The resulting formulation, presented in the following section, enabled the model to reproduce the transient rise and fall in ρ and to capture the correct scaling of delay time with pulse duration.

5.4 Mathematical Model with Proportional Feedback Synthesis

The initial correction to the steady-state model, described in Subsection 3.1.1 and validated in Section 5.2, successfully corrected the post-pulse overshoot in growth rate by introducing a metabolic growth limitation after antibiotic removal. However, while this adjustment restored realistic recovery growth, the model continued to exhibit slower-than-observed adaptation of ribosome synthesis. The steady-state synthesis formulation responded too gradually to rapid shifts in antibiotic inhibition and nutrient flux, leading to delayed recovery of ρ and incomplete agreement with the experimental Δt dynamics. To address this limitation, a proportional feedback controller was introduced to the synthesis rate. In this formulation, ribosome synthesis responds to the instantaneous imbalance between the nutrient-limited and translation-limited growth regimes

$$\Delta\lambda(t) = \lambda_N(t) - \lambda_R(t), \tag{5.3}$$

where

$$\lambda_R(t) = \kappa_T(r_u - r_{\min}), \tag{5.4}$$

$$\lambda_N(t) = \kappa_N(r_{\max} - r_{\text{total}}), \tag{5.5}$$

corresponding to the translation-limited and nutrient-limited regimes, respectively. A positive imbalance ($\Delta\lambda > 0$) indicates translation limitation and triggers increased synthesis, while a negative imbalance ($\Delta\lambda < 0$) indicates nutrient limitation and suppresses synthesis. This feedback increases the responsiveness of the synthesis rate to fast intracellular changes, enabling smoother and faster adaptation during both the pulse and recovery phases. The synthesis rate follows

$$s(t) = \begin{cases} s_A^{SS}(T)\,\big[\,1 + \alpha_A\,\Delta\lambda(t)\,\big], & \text{during pulse,} \\ s_0^{SS}\quad\;\big[\,1 + \alpha_0\,\Delta\lambda(t)\,\big], & \text{post-pulse,} \end{cases} \tag{5.6}$$

where $s_A^{SS}(T)$ and s_0^{SS} are the steady-state synthesis anchors during and after a pulse of length T, respectively. These quantities are obtained from the steady-state synthesis relation (3.6) by substituting the corresponding growth rates

$$s_A^{SS} = \lambda_f \left[r_{\max} - \lambda_f\,\Delta r \left(\frac{1}{\lambda_0} - \frac{1}{\kappa_T \Delta r} \right) \right],$$

$$s_0^{SS} = \lambda_0 \left[r_{\max} - \lambda_0\,\Delta r \left(\frac{1}{\lambda_0} - \frac{1}{\kappa_T \Delta r} \right) \right].$$

Here, λ_f represents the inhibited steady-state growth rate during the antibiotic pulse, and λ_0 is the uninhibited, drug-free growth rate. The parameters α_A and α_0 are proportional gain coefficients (units of time, hours h), with distinct phase-specific values fitted for each carbon source (α_A^i and α_0^i, where $i \in \{\text{GLU}, \text{GLY}\}$). During optimization, proportional gains were allowed to vary within physiologically reasonable bounds

$$\begin{aligned} \alpha_0^{\text{GLU}},\ \alpha_A^{\text{GLU}} &\in [0.05,\ 15.0], \qquad (h) \\ \alpha_0^{\text{GLY}},\ \alpha_A^{\text{GLY}} &\in [0.05,\ 20.0] \qquad (h). \end{aligned}$$

These limits were selected to ensure convergence while spanning the physiologically relevant timescales of ribosome synthesis and recovery observed experimentally (on the order of hours). To maintain physiological consistency across transitions, the proportional feedback formulation was paired with a minimum growth law, guaranteeing that instantaneous growth is governed by the most limiting process

$$\lambda(t) = \min\{\lambda_R(t),\ \lambda_N(t)\}. \tag{5.7}$$

This constraint prevents the feedback controller from producing unphysical growth beyond translational or metabolic limits, while allowing dynamic switching between limitation regimes as amino acid supply and ribosome demand evolve through the pulse and recovery phases. This updated synthesis formulation substantially improved agreement with experimental data. The predicted Δt remained consistent with observations, ρ trajectories exhibited stronger correspondence with measured values, and inhibition data aligned closely with experimental measurements across both carbon sources. Overall, the incorporation of proportional feedback yielded improved fits and biologically realistic pulse and recovery dynamics (see Figure 5.3). Minor deviations remain between the fitted model and experimental trajectories. These discrepancies are revisited in Chapter 6. Full numerical values are provided in Table 5.3.

Parameter	Symbol	Glucose	Glycerol
Antibiotic Unbinding Rate	k_{off} (h^{-1})	33234.61	33234.61
Antibiotic Binding Rate	k_{on} $((\mu\text{M}h)^{-1})$	776.33	776.33
Antibiotic Influx Permeability (Into Cell)	P_{in} (h^{-1})	1705.54	1665.16
Antibiotic Efflux Permeability (Out of Cell)	P_{out} (h^{-1})	10.25	10.84
Proportional Gain (During Pulse)	α_A (h)	1.00	0.774
Proportional Gain (Post-Pulse)	α_0 (h)	1.44	2.60

Table 5.3: Optimal parameters for the proportional feedback controller under glucose and glycerol conditions.

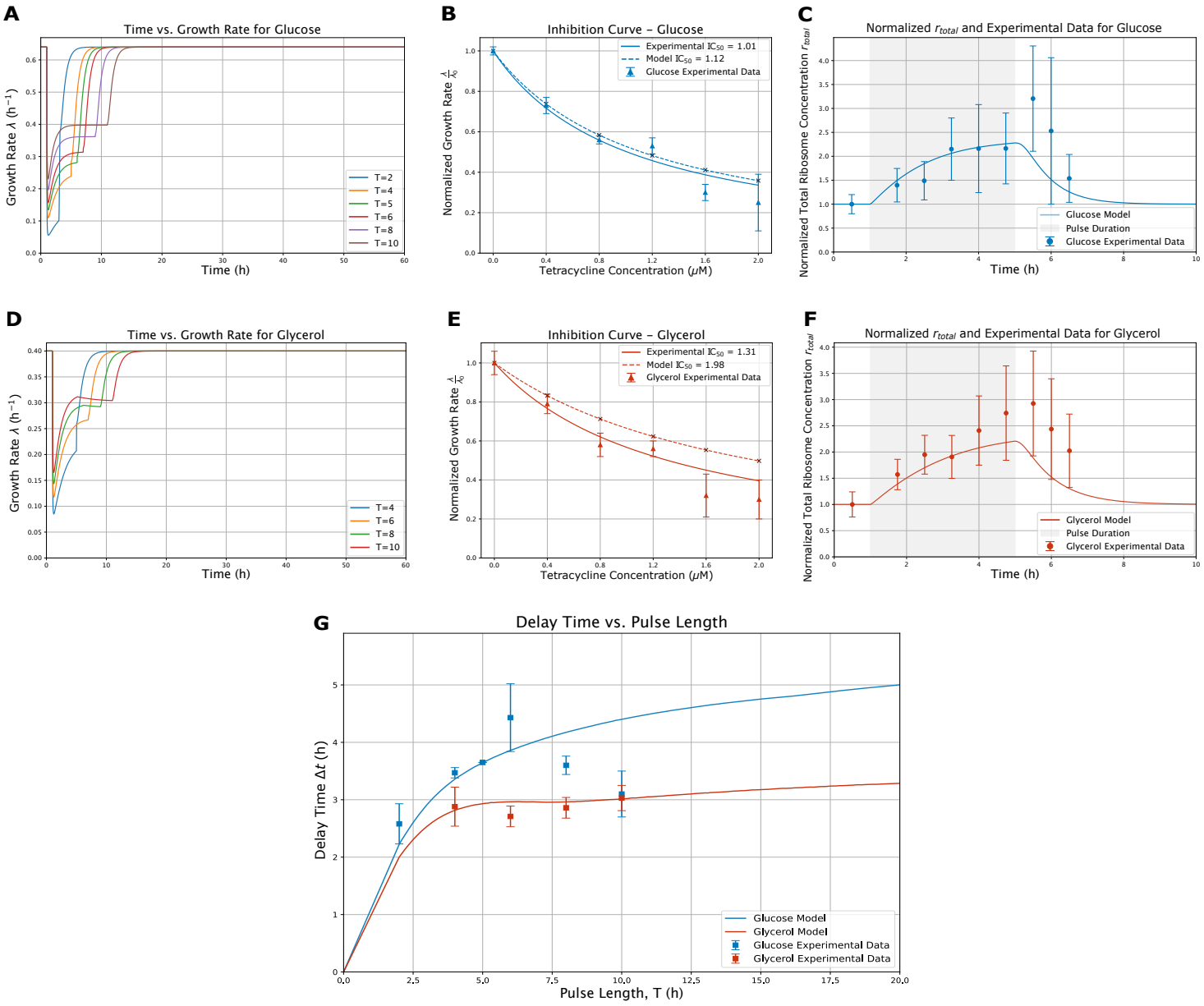


Figure 5.3: Model fits incorporating proportional feedback on synthesis under glucose and glycerol conditions. (A–C) Glucose; (D–F) Glycerol. (G) Δt as a function of pulse length. Incorporating proportional feedback improved agreement with experimental data across both carbon sources, accurately reproducing Δt saturation and the transient rise and relaxation of ρ during pulse and recovery. Minor deviations in post-pulse relaxation remain, but overall the model captures realistic pulse–recovery dynamics consistent with experimental observations.

5.4.1 Mechanistic Interpretation of the Proportional Feedback

The proportional feedback formulation establishes a mechanistic link between elongation rate (ε), ppGpp signaling (g), and ribosome synthesis (s). At its core is the flux imbalance (5.3), which quantifies the mismatch between nutrient-limited and translation-limited growth. Deviations in $\Delta\lambda$ modulate ppGpp levels through the associated change in elongation rate ($\Delta\varepsilon$), repress rRNA transcription, and adjust ribosome synthesis to restore balance. The feedback structure can be summarized conceptually as

$$\Delta\lambda \;\longrightarrow\; \Delta\varepsilon \;\longrightarrow\; g(\varepsilon) \;\longrightarrow\; s(g) \;\longrightarrow\; s(t) = s^{SS}_{\text{phase}}[1 + \alpha_{\text{phase}}\Delta\lambda(t)]\,.$$

Following the Jacob–Monod operon framework for transcriptional repression [85], the repressed rRNA transcription rate can be expressed as

$$\eta_m(R) = \eta^0_m \frac{1 + f_R\left(\frac{R}{K_R}\right)^n}{1 + \left(\frac{R}{K_R}\right)^n}, \tag{5.8}$$

where R denotes the repressor concentration, K_R is the repression threshold, n the Hill coefficient, and $f_R \in [0, 1]$ the fold-change between fully unbound and fully bound states. To specialize (5.8) to ppGpp-mediated ribosome synthesis, identify $R \equiv g$ and η_m with the coarse-grained synthesis drive s. Under strong repression ($f_R = 0$) and non-cooperative control ($n = 1$), this relation simplifies to a hyperbolic repression law. These assumptions show the near-complete inhibition of rRNA transcription at high ppGpp and the approximately first-order response observed experimentally, yielding a parsimonious form consistent with standard Hill-type control [85][232]. This relation simplifies to a hyperbolic repression law

$$s(g) = \frac{s_{\max}}{1 + g/K_R}, \tag{5.9}$$

where $s_{\max}$ is the maximal derepressed synthesis rate and K_R the characteristic repression strength. Experimental evidence indicates that intracellular ppGpp levels vary inversely with elongation rate [232]

$$g(\varepsilon) = c\left(\frac{\varepsilon_{\max}}{\varepsilon} - 1\right), \tag{5.10}$$

where c is a proportionality constant and $\varepsilon_{\max}$ the maximal elongation rate. Substituting (5.10) into (5.9) gives the synthesis rate as a function of elongation

$$s(\varepsilon) = \frac{s_{\max}}{1 + \frac{c}{K_R}\left(\frac{\varepsilon_{\max}}{\varepsilon} - 1\right)}. \tag{5.11}$$

At steady state (pre-pulse), the elongation rate equals ε_0, and the corresponding synthesis rate and ppGpp concentration are

$$s_0 = \frac{s_{\max}}{1 + g_0/K_R},$$
$$g_0 = c\left(\frac{\varepsilon_{\max}}{\varepsilon_0} - 1\right).$$

To derive a tractable linearized feedback form, expand (5.11) around the steady-state elongation rate ε_0 for small deviations $\varepsilon = \varepsilon_0(1 + \delta)$, where $\delta = (\varepsilon - \varepsilon_0)/\varepsilon_0$

$$s(\varepsilon) \approx s_0 + \left.\frac{ds}{d\varepsilon}\right|_{\varepsilon_0} \varepsilon_0\, \delta. \tag{5.12}$$

The derivative is obtained using the chain rule

$$\frac{ds}{d\varepsilon} = \frac{ds}{dg}\frac{dg}{d\varepsilon},$$
$$\frac{ds}{dg} = -\frac{s_{\max}}{K_R}\frac{1}{(1 + g/K_R)^2},$$
$$\frac{dg}{d\varepsilon} = -c\,\frac{\varepsilon_{\max}}{\varepsilon^2}.$$

Evaluating at the baseline ($g = g_0$, $\varepsilon = \varepsilon_0$) yields

$$\left.\frac{ds}{d\varepsilon}\right|_{\varepsilon_0} = \frac{c\,\varepsilon_{\max} s_{\max}}{K_R}\frac{1}{\varepsilon_0^2}\frac{1}{(1 + g_0/K_R)^2}. \tag{5.13}$$

Substituting (5.13) into (5.12) gives the linearized synthesis rate

$$s(\varepsilon) \approx s_0 + \left[\frac{c\,\varepsilon_{\max} s_{\max}}{K_R}\frac{1}{\varepsilon_0}\frac{1}{(1 + g_0/K_R)^2}\right]\delta. \tag{5.14}$$

To couple the elongation rate deviation δ to the growth–flux imbalance, we define

$$\delta = \beta\,\Delta\lambda, \qquad \Delta\lambda \equiv \lambda_N - \lambda_T, \tag{5.15}$$

where β quantifies the sensitivity of elongation rate to the supply–demand imbalance $\Delta\lambda$. Substituting (5.15) into (5.14) yields the proportional form

$$s(t) \approx s_0 + \tilde{\alpha}\,\Delta\lambda(t), \tag{5.16}$$
$$\tilde{\alpha} = \beta\,\frac{c\,\varepsilon_{\max} s_{\max}}{K_R}\frac{1}{\varepsilon_0}\frac{1}{(1 + g_0/K_R)^2}. \tag{5.17}$$

For simulations, this relationship is implemented multiplicatively around a steady-state anchor for each growth phase (pulse or post-pulse)

$$s(t) = s^{SS}_{\text{phase}}[1 + \alpha_{\text{phase}}\Delta\lambda(t)]\,, \tag{5.18}$$

where the proportional coefficient is defined as

$$\alpha_{\text{phase}} = \frac{\tilde{\alpha}}{s^{SS}_{\text{phase}}}. \tag{5.19}$$

The coefficient α_{phase} (units of time, hours h) and represents the effective proportional gain governing how strongly ribosome synthesis responds to transient growth–flux imbalances.

Fitted results show moderate proportional gains during the pulse phase ($\alpha_A^{\text{GLU}} = 1.0\,h$, $\alpha_A^{\text{GLY}} = 0.77\,h$) and larger gains during recovery ($\alpha_0^{\text{GLU}} = 1.44\,h$, $\alpha_0^{\text{GLY}} = 2.6\,h$), indicating enhanced corrective feedback post-pulse, particularly under slower-growth conditions. This proportional controller reproduces the experimental recovery dynamics in both Δt and ρ. Higher gains yield faster return to steady state and sharper ρ peaks, while lower gains produce more gradual recovery. These findings confirm that proportional feedback on synthesis reproduces the essential regulation underlying the observed pulse–recovery trajectories, bridging molecular ppGpp-mediated control and macroscopic growth behaviour. The proportional feedback extends beyond numerical fitting and carries direct physiological meaning. It encapsulates how *E. coli* continuously balances amino acid supply and translational demand through regulatory feedback mediated by ppGpp. When amino acid pools are depleted and uncharged tRNAs accumulate, ppGpp concentration rises, repressing rRNA transcription and reducing ribosome synthesis. As amino acid levels recover, ppGpp levels fall, relieving repression and restoring synthesis. This dynamic feedback constitutes a graded, proportional form of control, ensuring that proteome resources are continuously redistributed to match metabolic conditions.

Within this framework, the flux imbalance $\Delta\lambda$ represents the instantaneous difference between nutrient supply (λ_N) and translational demand (λ_R). When supply exceeds demand ($\Delta\lambda > 0$), amino acid pools rise, ppGpp falls, and ribosome synthesis is upregulated. When demand exceeds supply ($\Delta\lambda < 0$), ppGpp increases, repressing synthesis until balance is restored. The proportional gain α determines the strength of this corrective response, maintaining stability across rapid transitions between nutrient- and antibiotic-limited growth. This process constitutes a continuous form of proteome reallocation rather than a discrete regulatory switch. The cell continually adjusts ribosomal and metabolic protein fractions to preserve the linear relationship between ribosomal mass fraction and

growth rate described by the bacterial growth laws [189], even under transient, non-steady-state conditions. The proportional feedback thus unifies steady-state growth laws and dynamic regulatory responses within a single quantitative rule, growth control as a stable, negative feedback process. By coupling ribosome synthesis directly to amino acid flux, the mechanism stabilizes proteome composition and enables smooth adaptation during both nutrient limitation and antibiotic stress.

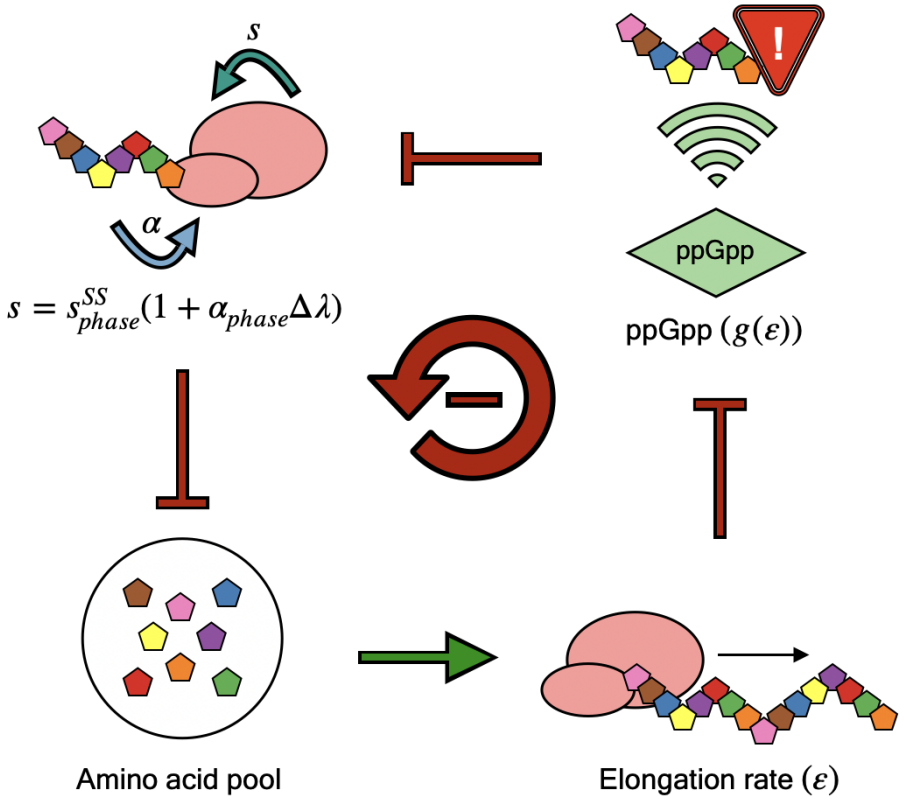


Figure 5.4: Schematic of the proportional feedback controller linking amino acid supply, translational demand, ppGpp signaling, and ribosome synthesis. Increased amino acid availability raises the elongation rate (ε), whereas slowed elongation triggers ppGpp accumulation ($g(\varepsilon)$). Elevated ppGpp represses ribosome synthesis, while synthesis consumes amino acids, reducing supply. These interactions form a stable negative feedback loop. When supply exceeds demand, ppGpp falls and synthesis accelerates; when demand exceeds supply, ppGpp rises and synthesis slows. This behaviour follows the proportional law $s = s^{SS}(1 + \alpha\,\Delta\lambda)$, where $\Delta\lambda = \lambda_N - \lambda_R$ and α is the feedback gain, ensuring continuous adaptation of ribosome synthesis during nutrient or antibiotic perturbations.

5.5 Sensitivity and Hessian Analysis

To evaluate how parameter modifications influence model outputs, local sensitivity and Hessian analyses were performed using the finite-difference formulations outlined in Subsection 4.3.4. For the sensitivity analysis, the pulse-phase ribosomal fraction ρ was selected as the output of interest. This quantity was chosen because it provided the dominant constraint for tuning the synthesis rate. In the initial model, the steady-state behaviour of ρ was overly constrained across the pulse and post-pulse phases, preventing accurate reproduction of experimental trajectories. The updated proportional formulation introduced sufficient variability to capture these dynamics more realistically, while allowing direct assessment of how small perturbations in the feedback controller affect overall model stability and fit quality. For the Hessian analysis, the total cost function was used as the scalar output, combining IC_{50}, Δt, and ρ through a weighted mean squared error as described in Subsection 4.3.5. This approach identified how parameter interactions influence the overall fit quality rather than individual observables, and the Hessian captured both curvature and cross-sensitivity of the cost function in parameter space. Because antibiotic binding and cellular transport occur on rapid timescales of minutes and act together, the four base parameters ($k_{\mathrm{off}}, k_{\mathrm{on}}, P_{\mathrm{in}}, P_{\mathrm{out}}$) were grouped into composite ratios $K_D = k_{\mathrm{off}}/k_{\mathrm{on}}$, $R_P^{\mathrm{GLU}} = P_{\mathrm{in}}^{\mathrm{GLU}}/P_{\mathrm{out}}^{\mathrm{GLU}}$, and $R_P^{\mathrm{GLY}} = P_{\mathrm{in}}^{\mathrm{GLY}}/P_{\mathrm{out}}^{\mathrm{GLY}}$. This quasi-equilibrium reduction shows that binding and transport equilibrate quickly relative to the slower physiological dynamics of recovery. The proportional gains (α_A, α_0) were retained explicitly, as they act on longer regulatory timescales and maintain consistency with the dynamic synthesis update across pulse and recovery phases.

5.5.1 Local Sensitivity of Pulse-Phase RNA/Protein Ratio

The sensitivity results for the proportional feedback controller of synthesis rate (described in Section 5.4) are shown in Figure 5.5. Under glucose conditions, the pulse-phase ratio ρ is most sensitive to K_D, indicating that small perturbations in the balance between antibiotic binding and unbinding strongly affect the depth of the response during the pulse. A smaller K_D (stronger binding) increases the fraction of antibiotic-bound ribosomes, enhancing inhibition and elevating ρ, whereas a larger K_D (weaker binding) reduces occupancy and weakens the pulse response. Under glycerol, sensitivity shifts toward R_P, showing that transport asymmetry dominates control when synthesis is already slowed. Increasing R_P (favoring influx) raises intracellular antibiotic levels and strengthens inhibition, while decreasing R_P (favoring efflux) lowers accumulation and reduces the inhibitory effect.

The proportional feedback gains influence ρ in distinct ways. As expected for a pulse-specific output, the recovery-phase gain α_0 has negligible sensitivity, since varying α_0 does not alter ρ during the pulse. In contrast, the pulse-phase gain α_A is influential, and its effect reverses between media. In glucose, a higher α_A increases the pulse rise in ρ, whereas in glycerol, the same increase suppresses it. This difference reflects the shift between translation-limited and supply-limited regimes. In glucose, stronger proportional drive during the pulse amplifies synthesis in response to $\Delta\lambda > 0$, increasing ρ. In glycerol, that same increase in α_A intensifies competition for limited precursors, reducing ρ. Together, these results show that pulse-phase ρ adaptation is governed primarily by binding strength (K_D) in glucose and by transport balance (R_P) in glycerol. Within the pulse, sensitivity is dominated by the medium-dependent action of α_A, while α_0 remains negligible because it regulates only post-pulse recovery.

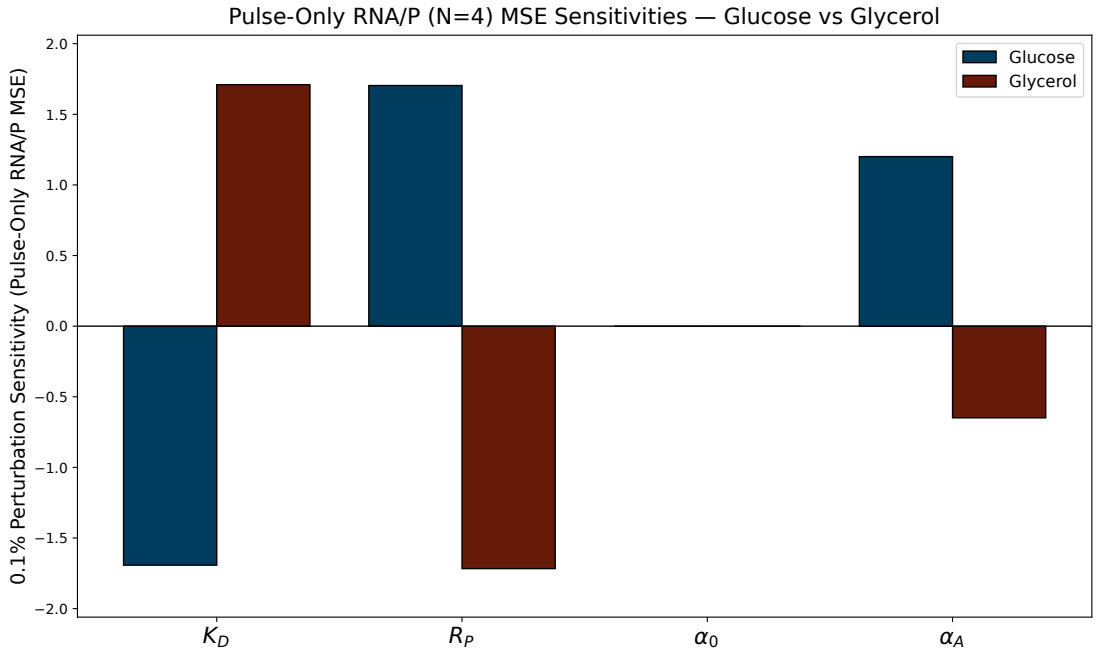


Figure 5.5: Local sensitivity of the pulse-phase RNA/protein ratio (ρ) to parameter perturbations. Under glucose conditions, ρ is most sensitive to the dissociation constant K_D, whereas in glycerol conditions sensitivity shifts toward the transport ratio R_P. This reflects that translational inhibition dominates when nutrient quality is high, while transport balance governs inhibition in nutrient-poor media. The recovery-phase gain α_0 is negligible in this analysis because it does not affect ρ during the pulse.

5.5.2 Hessian Eigenvector Analysis

Hessian analysis measures the curvature of the total cost function with respect to parameter variation. Directions associated with large eigenvalues correspond to stiff parameter combinations, where even small perturbations cause large increases in model error. Directions with small eigenvalues are sloppy, meaning that wide parameter ranges yield nearly indistinguishable fits. Distinguishing between stiff and sloppy directions reveals which parameter combinations are strongly constrained by the data and which remain flexible. Figure 5.6 shows all seven eigenvectors of the Hessian, ordered by eigenvalue magnitude. Each histogram depicts the normalized contribution of each parameter to the corresponding eigenvector basis. The pattern across eigenvectors illustrates how parameter groupings align with the principal directions of curvature in the cost landscape. The stiffest direction is dominated by K_D and R_P, confirming that antibiotic binding and transport are the most tightly constrained processes in the model. Adjusting either parameter substantially alters inhibition levels and recovery trajectories, emphasizing their physiological relevance. By contrast, the sloppiest eigenvector is dominated by α_0^{GLY}, indicating that the recovery-phase proportional gain in glycerol contributes little to the global fit. Perturbations in this parameter have minimal effect on the weighted mean squared error, reflecting that post-pulse behaviour in the slower-growth medium is only weakly constrained by experimental data. Together, these results indicate that the stiff directions enforce consistency in drug–ribosome interaction and transport balance, while the sloppy directions capture regulatory flexibility in the slower recovery dynamics of glycerol. The eigenstructure indicates that flexibility lies primarily within the proportional feedback sector, whereas the binding and transport parameters remain tightly constrained by experimental data.

5.5.3 Model Comparison Across Successive Refinements

To summarize the evolution of the model framework, Figure 5.7 compares three formulations, the original model (3.3), the metabolic-limitation correction, and the proportional feedback synthesis model, each evaluated across the pre-pulse, pulse, and recovery phases. Each formulation was developed to address a specific mechanistic limitation identified in the preceding model. In the original model (3.3), growth was assumed to be translation-limited throughout all phases, with synthesis defined solely by the steady-state relation $s = s^{SS}(\lambda)$. This assumption caused the system to return instantaneously to the translation-limited regime after the pulse, producing an unpredicted overshoot in growth rate λ. The metabolic-limitation correction introduced a physiological switch in the post-pulse phase, replacing $\kappa_T(r_u - r_{\min})$ with $\kappa_N(r_{\max} - r_{\mathrm{total}})$ once translation

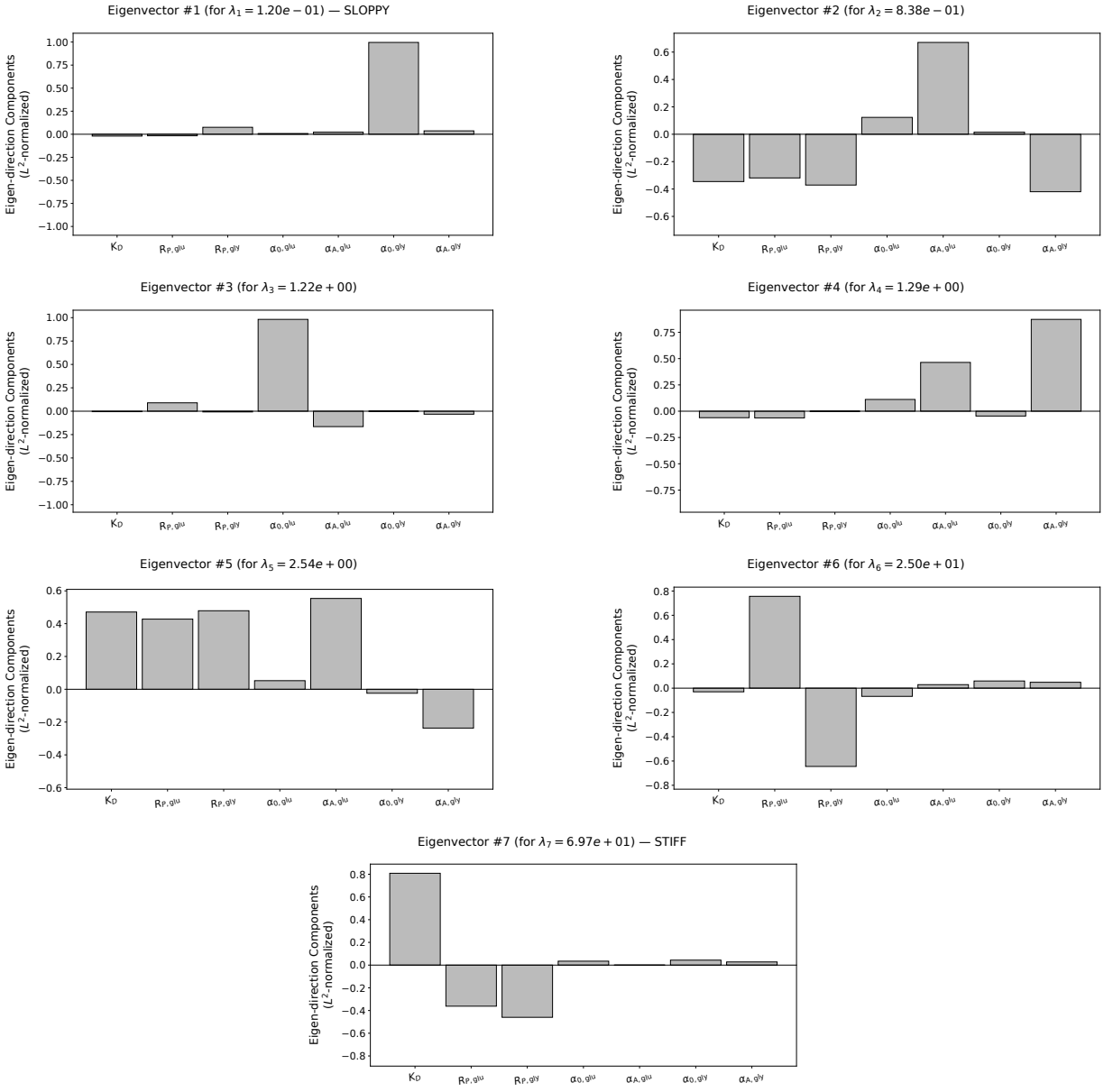


Figure 5.6: Eigenvector component histograms from Hessian analysis of the proportional-response model. Each panel corresponds to one of the seven eigenvectors, ordered by associated eigenvalue magnitude. Bars show the normalized contribution of each parameter direction to the eigenvector basis, illustrating stiff versus sloppy parameter combinations. Collectively, the spectra reveal the anisotropic structure of parameter sensitivity in the cost landscape, with only a subset of directions tightly constrained by the data.

resumed. This removed the overshoot but led to slower recovery dynamics, since ribosome synthesis remained constrained by a static steady-state balance. The final proportional feedback formulation incorporated dynamic regulation of synthesis through the term $s(t) = s^{SS}_{\text{phase}}[1 + \alpha_{\text{phase}}\Delta\lambda(t)]$, allowing ribosome production to respond in real time to the flux imbalance. This mechanism accelerated the recovery rate and reproduced the experimentally observed Δt saturation and ρ recovery behaviour across both carbon sources.

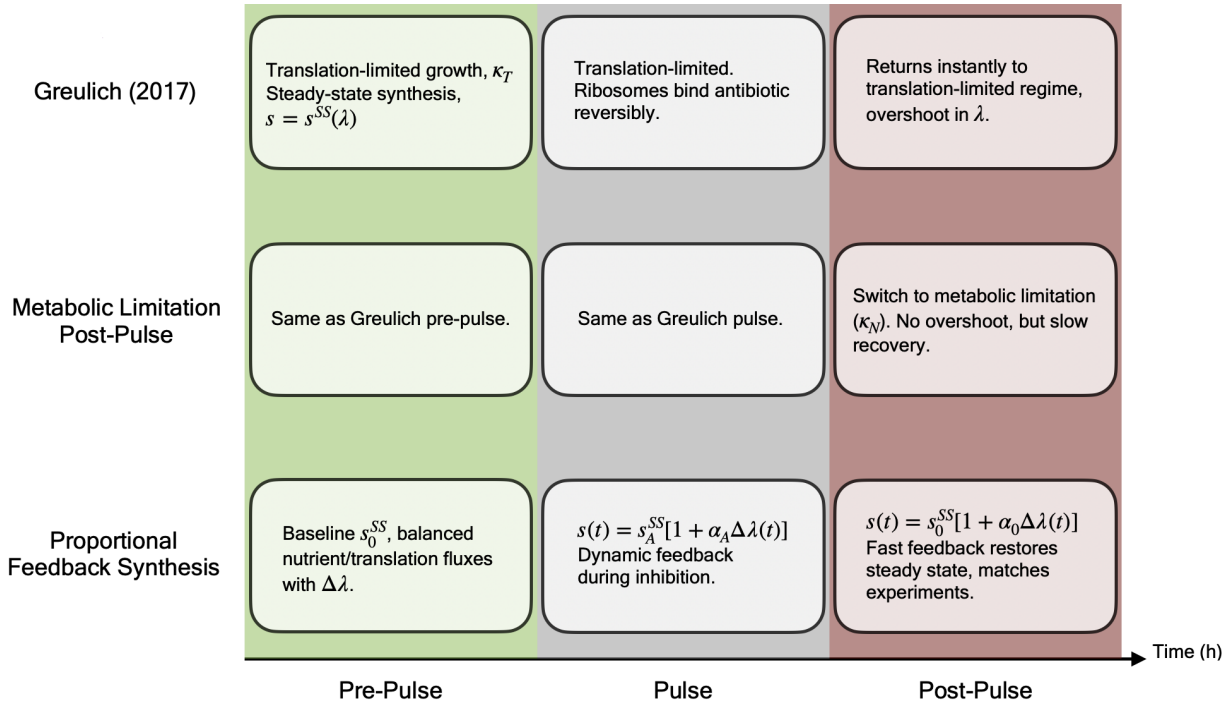


Figure 5.7: Conceptual comparison of the three model formulations across pre-pulse, pulse, and post-pulse phases. Each cell summarizes the limiting process and synthesis regulation for the corresponding regime. The original model (3.3) assumes translation-limited growth throughout, leading to post-pulse overshoot. The metabolic-limited model switches to nutrient limitation after antibiotic removal, eliminating overshoot but slowing recovery. The proportional feedback model introduces time-dependent synthesis control based on the flux imbalance $\Delta\lambda$, producing rapid recovery consistent with experiment.

Information-criterion analysis further corroborates the mechanistic progression shown in Figure 5.7, as summarized in Table 5.4 [1][187]. Because all residuals were normalized by experimental variances, the comparison reflects biological accuracy rather than scale differences across datasets. The original formulation (3.3) is overwhelmingly rejected by both AIC and BIC because its assumption of persistent translation limitation forces rapid

post-pulse recovery and negligible Δt, directly contradicting the saturating experimental Δt. Introducing post-pulse metabolic limitation drastically reduces the mismatch, confirming that nutrient-limited recovery is essential to remove the unphysical growth-overshoot artifact. However, the metabolic model still imposes a static synthesis rate and cannot reproduce the time-dependent compensation evident in Δt and ρ data, resulting in poor performance despite its correct limiting regime. The final proportional feedback controller attains the lowest AIC and BIC scores, even though it contains more free parameters. This outcome reflects a biological, not numerical, advantage, dynamic ribosome synthesis is required to match both the immediate inhibited growth state and the metabolically constrained recovery trajectory. Thus, information criteria identify the same mechanistic necessity revealed by experiment, recovery dynamics depend not only on metabolic limitation but also on feedback-mediated proteome reallocation during the transition back to balanced growth.

Model	k (Parameters)	AIC	BIC
Original Greulich	4	2347.94	2354.70
Metabolic Correction	6	2048.15	2058.28
Proportional Feedback	10	1804.42	1821.31

Table 5.4: AIC/BIC comparison of the three successive formulations using standardized residuals across Δt, ρ, and IC_{50}. Lower AIC and BIC values indicate greater evidence in favour of the model. Although the proportional feedback formulation contains more parameters ($k = 10$), it achieves the minimum criterion values, indicating that dynamic synthesis regulation is required to reproduce both inhibited and recovery dynamics.

Together, these refinements define a coherent mechanistic progression from purely steady-state inhibition dynamics to a dynamically regulated, physiologically responsive model of antibiotic stress and recovery. By integrating metabolic limitation and proportional feedback, the final formulation reconciles both steady-state inhibition and transient recovery behaviour within a unified quantitative framework.

Chapter 6

Discussion

6.1 Foundations and Model Evolution

This thesis extends the steady-state framework describing reversible binding of ribosome-targeting antibiotics and the associated inhibition of bacterial growth [71], together with its subsequent dynamic formulation for pulse-dose conditions [72]. These models established how intracellular antibiotic transport, binding kinetics, and ribosomal activity determine steady-state growth and transient inhibition. However, they did not fully capture how bacterial physiology adapts once antibiotic is removed. This work advances this formulation by incorporating time-dependent feedback and growth-limiting processes that more accurately represent *E. coli* dynamics under transient exposure. In doing so, the steady-state and pulse-based frameworks are integrated into a dynamic mathematical model capable of reproducing recovery kinetics, proteome reallocation, and nutrient-dependent adaptation. Two principal refinements were critical to this development. First, the post-pulse growth-limiting regime was corrected to illustrate metabolic limitation rather than translational limitation after antibiotic removal. In the original formulation, continued translation-limited growth following the pulse produced an unphysical overshoot in growth rate.

Reassigning the limitation to nutrient supply resolved this artifact and restored physiological consistency. Once ribosomes are released from antibiotic inhibition, growth becomes limited by metabolic resource availability rather than by protein synthesis capacity. Second, a proportional feedback controller on the ribosome synthesis rate was incorporated to regulate adaptation dynamically across both pulse and recovery phases. This controller links synthesis to the instantaneous flux imbalance between translational and nutrient limitation, allowing ribosome production to adjust continuously in response to intracellular

changes. The addition of this feedback does not fully replace the steady-state or pulse-dose formulations but extends them, merging reversible binding and transport kinetics within a regulatory framework that reproduces the experimentally observed adaptation timescale. Together, these refinements produce a consolidated mathematical model that combines steady-state constraints, metabolic realism, and dynamic regulatory control. The result is a physiologically interpretable model that reconciles antibiotic inhibition, ribosome recovery, and nutrient dependence within a single system.

6.2 Physiological Correction: Post-Pulse Metabolic Limitation

The first refinement to the steady-state pulse model corrected the post-pulse growth-limiting process. In the original formulation, growth remained translation-limited after antibiotic removal, which produced an artificial acceleration in ribosome synthesis and an unphysical growth rate overshoot in the recovery phase. This behaviour was inconsistent with experimental results, where growth rate never exceeds its pre-pulse steady state. Once translational inhibition is lifted, *E. coli* no longer lacks active ribosomes. Instead, the limiting factor becomes the supply of metabolic precursors, particularly amino acids that fuel protein synthesis and energy metabolism. Replacing translation-limited control with nutrient-limited control during recovery restored this physiological balance. After a pulse, unbound ribosomes reaccumulate more rapidly than amino acid pools are replenished. As a result, growth becomes limited by the cell's capacity to synthesize and supply amino acids, not by the availability of translational machinery. This shift ensures that recovery proceeds gradually toward steady state without surpassing it, producing realistic growth trajectories that match experimental observations in both glucose and glycerol media.

This correction also provides a clearer interpretation of the delay time Δt that separates antibiotic removal from the onset of exponential recovery. In the revised model, Δt reflects the effective loss of biomass accrued during the inhibited period, which must be caught up in the exponential regime. It also reflects the additional recovery time required for proteome reallocation and amino acid replenishment as the cell transitions from the antibiotic-suppressed state back to balanced growth. The saturation of Δt with longer pulse durations arises naturally from this mechanism. Once amino acid synthesis and metabolic flux become the rate-limiting factors, additional exposure time no longer increases recovery delay, resulting in a plateau. This behaviour aligns with the measured delay time curves, which show diminishing returns beyond extended pulse lengths. By redefining the growth-limiting process in terms of amino acid supply rather than ribosome

availability, the model captures the full physiological origin of Δt. It reflects both biomass deficit during the pulse and metabolic recovery afterward. This correction formed the foundation for the introduction of a dynamic synthesis feedback law, which explicitly links amino acid availability, translational demand, and ribosome production.

A key implication of nutrient-limited recovery is that, immediately after antibiotic removal, the cell transiently maintains a ribosome pool larger than what can be productively engaged in elongation. This unused translational capacity does not incur a substantial energetic penalty on its own. Idle ribosomes consume little ATP when not polymerizing peptides, and the major energetic cost in translation arises from elongation rather than from maintaining ribosomal proteins. However, a sustained mismatch between ribosome abundance and metabolic flux can impose indirect costs. Excess ribosomes tie up amino acids and chaperone capacity, and incomplete utilization of the translational apparatus can increase biosynthetic inefficiency and proteostasis stress. Such imbalances increase reliance on protein quality-control pathways and can amplify oxidative burden, a known contributor to stress-induced mutagenesis in bacteria [101]. Although the present experiments operate on short post-pulse timescales, where these effects are expected to be transient and largely buffered, this highlights how even reversible ribosomal inhibitors can reshape the cellular economy of amino acids and protein quality control without causing lethal damage [12].

A natural question is whether valuable information is lost by defining Δt solely from the clean exponential regimes and excluding the full transient trajectory. The early recovery phase immediately after antibiotic removal contains rich physiological signatures, including rapid changes in elongation rate, proteome reallocation, amino-acid pool dynamics, and the non-monotonic synthesis behaviour captured by the corrected model. These transient features can, in principle, inform regulatory mechanisms and recovery timescales. From an experimental standpoint, however, this regime is highly sensitive to noise, resolution limits, and variability in OD measurements at low biomass. Instantaneous growth rate, computed as $\lambda(t) = d[\ln(\mathrm{OD})]/dt$, is especially unstable because finite-difference estimation amplifies measurement error. Using Δt as a time-shift metric avoids these instabilities and provides a robust, model-agnostic measure that integrates the full inhibitory cost of the pulse. The transient dynamics remain mechanistically important and are resolved within the model, but they are not used directly as experimental observables because Δt is stable, comparable across media, and more tightly linked to long-term physiological recovery rather than short-term variability.

Although the proportional feedback model substantially improves agreement with all three datasets, the remaining deviations in Figure 5.3 reflect physiological processes that are not represented in the minimal framework. The model relaxes the RNA/protein ratio ρ more rapidly than observed experimentally, which suggests that metabolic recovery and

amino acid repletion may lag behind the return of full translational capacity. Small mismatches in inhibition curves and in the saturation of Δt may also arise from variability in permeability across individual cells, heterogeneous intracellular drug accumulation, or modest differences in baseline growth rate across replicates. These discrepancies point to missing regulatory detail rather than a flaw in the core growth-law structure. They indicate where additional mechanisms, including nonlinear ppGpp synthesis and degradation, explicit amino acid pool dynamics, or ribosome rescue pathways, could refine future models. Importantly, the observed mismatches do not alter the central physiological interpretation of the corrected model, which links recovery dynamics to metabolic limitation rather than to ribosome scarcity.

Although ppGpp is the molecular regulator of ribosome synthesis in both the pulse and recovery phases, the physiological context in which it operates is completely different. During the pulse, translation is suppressed by antibiotic binding, elongation rate collapses, and ppGpp rises because ribosomes are unable to polymerize peptides efficiently. The bottleneck is therefore translational, even in glucose, where large ribosomal reserves and high metabolic capacity amplify the relative drop in elongation rate. Under these conditions, a strong increase in ribosome synthesis is observed experimentally, and glucose requires a larger feedback gain α_A to reproduce this sharp compensatory response. Once the antibiotic is removed, the limiting process shifts. Elongation rate rises rapidly, ribosomes are no longer inhibited, and amino acid supply becomes the dominant constraint. In this phase, ppGpp responds primarily to metabolic shortage rather than to translational arrest. Cells growing in glycerol already operate with lower metabolic reserves and display a stronger ppGpp signal during recovery. As a result, glycerol requires a larger recovery gain α_0 to match the stronger corrective response and slower return to steady state. In glucose, abundant metabolic resources reduce the ppGpp signal after the pulse and only a mild adjustment in synthesis is required. Thus, a single molecular regulator produces two distinct dynamical behaviours, because it senses different imbalances in each phase. During the pulse, ppGpp reflects a collapse in translational flux. During recovery, it reflects a shortage of metabolic precursors. The separate gains α_A and α_0 are therefore not arbitrary parameters but expressions of the nutrient-dependent physiological asymmetry that ppGpp is responding to in each regime.

6.3 Physiological Role of the Proportional Feedback Controller

The refined mathematical model extends the metabolic correction by introducing a proportional feedback controller that regulates ribosome synthesis according to the instantaneous imbalance between nutrient supply and translational demand. In this framework, synthesis adjusts continuously in response to the flux imbalance $\Delta\lambda$, which quantifies the mismatch between the nutrient-limited and translation-limited growth regimes. When amino acid supply cannot meet translational demand, $\Delta\lambda$ becomes negative and the feedback suppresses ribosome synthesis. On the other hand, when translational activity falls behind nutrient flow, $\Delta\lambda$ becomes positive and synthesis is proportionally elevated. This formulation couples amino acid availability directly to ribosome production. Instead of treating synthesis as fixed or stepwise, the model describes a smooth, graded regulation that continuously restores balance between metabolic supply and translational demand. The effective feedback gain α defines the responsiveness of this control, larger values accelerate recovery and stronger correction, while smaller values dampen it and yield slower return to steady state.

Mechanistically, this feedback captures the interplay between elongation rate, amino acid flux, and ribosome synthesis. Reduced amino acid supply slows elongation and increases intracellular ppGpp concentration, which represses rRNA transcription and limits ribosome production. As amino acid levels recover, ppGpp decreases, lifting repression and allowing synthesis to resume. The proportional feedback controller expresses this same physiological behaviour in compact form, representing the cell's graded response to nutrient–translation imbalance. In doing so, it provides a comprehensive quantitative description of the metabolic coupling that stabilizes recovery following antibiotic stress. This continuous feedback explains the model's agreement with experimental Δt and ρ trajectories. During the pulse, elevated $\Delta\lambda$ drives compensatory ribosome synthesis that mirrors the accumulation of unbound ribosomes. After the pulse, as amino acid supply again becomes limiting, $\Delta\lambda$ reverses sign, and synthesis proportionally slows to prevent overshoot. The coordinated action of these two growth laws captures the experimentally observed recovery kinetics across carbon sources and clarifies how bacterial physiology dynamically regulates ribosome production under alternating nutrient and antibiotic stress.

6.4 Therapeutic Implications and Optimal Pulse Duration

The results of this work extend beyond reproducing growth dynamics and connect directly to how antibiotic pulse strategies can be optimized. Within the model, Δt quantifies the duration of suppressed growth following antibiotic removal and therefore serves as a measure of overall treatment efficacy [72]. For bacteriostatic antibiotics such as the tetracycline used in this thesis, Δt reflects a temporary reduction in population expansion rather than lethal killing. In this setting, the product $\lambda_0 \Delta t$ represents the cumulative loss of potential growth relative to an untreated culture, capturing the overall physiological burden imposed by the pulse. The dependence of Δt on pulse length reveals a clear saturation pattern that can guide dosage design. The "shoulder" or "elbow" on the $\Delta t(T)$ curve separates two regimes. For shorter pulses, recovery is rapid and a substantial fraction of the exposure is effectively wasted. Beyond this shoulder, Δt approaches a plateau where additional antibiotic contact yields diminishing returns. Optimal therapeutic efficiency therefore lies near this transition, where inhibition is nearly complete yet excessive exposure and unnecessary toxicity are avoided [72].

The optimal pulse duration T^* provides a quantitative marker for this transition. As shown in Figure 6.1, Δt increases steeply with pulse length before approaching a plateau, indicating that the inhibitory burden becomes saturated. In the model, this saturation reflects the characteristic timescale

$$K = \frac{\mathrm{AUC}}{\mathrm{IC}_{50}},$$

which represents the dosing intensity, given by the total antibiotic exposure (AUC, area under the concentration–time curve) scaled by the concentration required to halve growth (IC_{50}). Biologically, K represents the effective inhibitory exposure required to reach half-maximal delay, analogous to the role of kinetic constants such as K_m or IC_{50} in classical pharmacological models. For short pulses ($T \ll K$), Δt grows nearly linearly, while for long pulses ($T \gg K$), the response saturates with $\Delta t \to K$. The pulse duration at which the $\Delta t(T)$ curve bends therefore satisfies $T^* \approx K$. This point marks the transition between the responsive and saturated regimes of inhibition.

For glucose, the optimal pulse lies near $T^*_{\mathrm{GLU}} \approx 7\,h$, while for glycerol the curve saturates earlier at $T^*_{\mathrm{GLY}} \approx 4.5\,h$, consistent with slower metabolic turnover and reduced recovery capacity. Physiologically, T^* marks the timescale at which the cell can no longer meaningfully distinguish between a longer pulse and an infinite one. Inhibition is maximized,

and further dosing provides diminishing benefit while increasing toxicity risk. Conversely, pulses shorter than T^* result in incomplete inhibition, allowing rapid recovery once the drug is removed and thereby diminishing overall treatment efficacy. The model therefore identifies T^* as the critical balance between under- and over-dosing, defining an optimal pulse length that maximizes suppression while minimizing unnecessary exposure. While these insights provide a quantitative framework for optimizing pulse duration in controlled *in vitro* settings, translation to clinical contexts must also account for host pharmacokinetics and pharmacodynamics, which influence drug distribution, clearance, and effective intracellular exposure times [42][72][106][114].

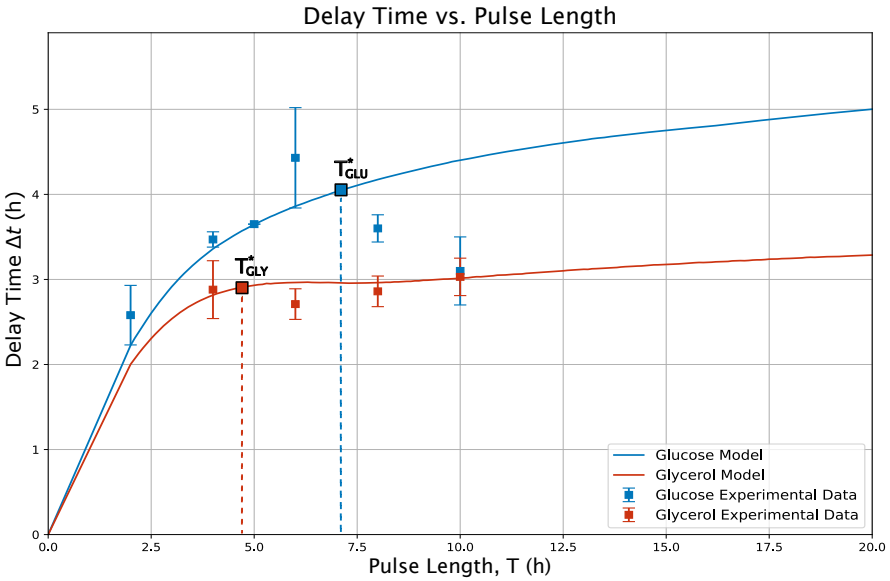


Figure 6.1: Optimal pulse duration inferred from delay time saturation. The delay time Δt increases with pulse length T before approaching a plateau. The shoulder point (T^*) marks the transition between responsive and saturated inhibition, indicating the most effective pulse duration. For glucose, $T^*_{\mathrm{GLU}} \approx 7\,h$; for glycerol, $T^*_{\mathrm{GLY}} \approx 4.5\,h$. Pulses shorter than T^* under-treat, whereas longer pulses provide diminishing additional inhibition.

Incorporating PK/PD structure would replace the idealized, rectangular antibiotic pulses used in this thesis with a time-dependent extracellular concentration profile shaped by absorption, tissue penetration, and drug clearance [42][106]. Pharmacokinetics determines how quickly the antibiotic reaches and leaves the infection site, while pharmacodynamics links these concentrations to intracellular drug accumulation and inhibitory effect [42]. Together, PK and PD would smooth the sharp on/off transitions of the *in*

vitro pulse, typically lowering peak intracellular concentrations but extending periods of subinhibitory exposure [114]. This would shift the apparent value of T^* and could require longer or repeated pulses to achieve an equivalent inhibitory burden [72]. Thus, while the model identifies an optimal pulse duration under controlled laboratory conditions, *in vivo* optimization demands coupling the bacterial physiology described here with host-specific PK/PD constraints.

6.5 Limitations & Challenges

Every modeling framework necessarily balances tractability with biological plausibility. The proportional-response model developed in this thesis successfully integrates nutrient- and translation-limited laws, but several limitations should be acknowledged. These arise from structural assumptions in the model, experimental constraints, computational challenges, and the scope of biological application. Each of these considerations also highlights avenues for future extension.

6.5.1 Model Structure

A key simplification is the coarse-grained treatment of proteome allocation. The present model reduces cellular physiology to the balance between ribosome synthesis and nutrient-limited growth, implemented via a proportional feedback controller. This abstraction captures the essence of proteome reallocation, but does not explicitly monitor all possible individual proteome sectors (see Figure 2.3) as described in recent studies [12][136]. In particular, the stringent response mediator (ppGpp) is not modeled explicitly, but rather approximated through a linearized feedback on synthesis. While this effectively reproduces the observed dynamics, it omits potentially nonlinear regulation and crosstalk with other cellular pathways [76][198]. Similarly, the binding and transport processes were condensed into ratios (K_D, R_P) that assume quasi-equilibrium, negating possible kinetic delays or energy dependencies. Another simplification is the assumption that ribosome synthesis and nutrient-limited growth can be cleanly separated into two regulatory axes. In actuality, these processes are interconnected through shared pools of precursors, metabolites, and transcriptional factors. These simplifications limit the scope of mechanistic interpretation, though they ensure a model structure that is both decipherable and fit to data.

6.5.2 Experimental Constraints

The experimental validation of the model relied on batch-culture assays with *E. coli* MG1655 exposed to tetracycline pulses. While this procedure provided reproducible growth curves, inhibition profiles, and ρ, it does not encompass the complexity of continuous-culture conditions such as chemostats or morbidostats [209]. The range of pulse lengths was also necessarily limited to experimentally feasible timescales. Measurements of ρ were bulk averages across populations, masking heterogeneity at the single-cell level, where subpopulations can display distinct proteomic responses [50][55]. Furthermore, growth rates were determined from OD-based measurements as opposed to direct growth rate measurements, which may mask changes in metabolism or morphology with changes in true biomass accumulation.

A practical constraint in this design was the choice to measure OD_{600} in glass culture tubes rather than in microplate readers. Plate readers offer high throughput, automated sampling, and fine temporal resolution, yet in minimal media they are susceptible to evaporation, path-length variability, and well-to-well differences in aeration, which introduce substantial noise into optical-density measurements. In practice, replicate variability in plate-reader growth curves routinely exceeded $\pm 50\%$, and derivative-based growth rate estimates were too noisy for reliable comparison with model predictions. Glass-tube cultures, by contrast, provided larger working volumes, improved aeration at 250 rpm, and produced smoother OD trajectories that were essential for Δt determination and synthesis-rate inference. Thus, for model fitting, experimental resolution rather than throughput was the critical requirement. Plate readers remain valuable for large-scale screening, and future work could pair their throughput with improved calibration and noise-reduction strategies. These design choices were deliberate to balance feasibility and resolution, but they restrict the extent to which the model can isolate fine-scale physiological variability. Incorporating single-cell assays or time-resolved proteomics would provide crisp constraints and a more detailed map between proteome reallocation and growth recovery.

6.5.3 Computational Challenges

Parameter estimation presented both technical and conceptual challenges. Although optimization achieved consistent fits across experimental datasets, the Hessian analysis revealed substantial anisotropy in parameter relationships. Stiff directions, dominated by cellular transport and recovery gains, were tightly constrained by the data, whereas sloppy combinations involving binding and influx allowed large uncertainties without large cost penalties. This highlights the general difficulty of inferring all kinetic parameters uniquely

from limited experimental observations [73]. Optimization itself was computationally demanding due to the nonlinear structure of the model, requiring cautious choice of bounds, initialization, and weighting of cost function components. Multi-objective trade-offs also complicated parameter estimation. Δt, ρ, and inhibition curves were all fit simultaneously, and perfect agreement across datasets was neither possible nor biologically reasonable. These considerations highlight the practical roadblocks to comprehensive parameterization, notably for models that attempt to integrate multiple regimes of physiology.

6.5.4 Scope of Applicability

The present model is limited in scope to a specific bacterial system and antibiotic. The results pertain to *E. coli* under glucose or glycerol conditions exposed to tetracycline pulses. Extrapolation to other organisms, nutrient contexts, or antibiotic classes requires caution. High-affinity ribosome-targeting antibiotics, such as aminoglycosides, can produce qualitatively different inhibitory dynamics compared to tetracycline [71][72], and non-ribosomal antibiotics (such as DNA replication inhibitors, cell-wall or membrane disruptors) act through distinct physiological constraints that lie outside the current framework. Taken together, these limitations highlight deliberate trade-offs that allowed the development of a tractable, experimentally anchored, and physiologically interpretable model. Recognizing these boundaries clarifies both the strengths and weaknesses of the present work, while providing a basis for future directions.

6.6 Future Directions and Broader Implications

Building upon the corrected steady-state and pulse-based framework developed in this thesis, several avenues emerge for extending the mathematical model and broadening its physiological and therapeutic scope. The adjustments introduced here, transitioning to nutrient-limited recovery and implementing synthesis feedback through the flux imbalance $\Delta\lambda$, form a general structure that can now be tested, parameterized, and generalized across diverse conditions. The following directions outline both experimental and theoretical opportunities to refine and expand this model toward wider biological and clinical applicability.

6.6.1 Model Extensions

Experimental Regimes to Stress-Test the Model.

Two practical directions are chemostat or morbidostat dosing to disconnect nutrient shifts from drug pulses and systematic analysis across transport flux and binding affinity to delineate regimes where Δt plateaus, inhibition consistency, and ρ dynamics most tightly constrain parameters. These procedures would directly sharpen the stiff and sloppy structure uncovered by the Hessian analysis and guide which sectoral extensions add the most explanatory power. Incorporating automated, high-frequency measurement systems could enable direct estimation of instantaneous growth rate, provided that experimental noise and signal drift are appropriately controlled.

Adding an Explicit ppGpp Module.

While the mathematical model implicitly captures ppGpp-mediated feedback, a small dynamical module for ppGpp (production by *RelA*/*SpoT*, dilution or turnover, and coupling to RNA/protein allocation) would let the fitted gains α_{phase} be rationalized in terms of biophysical parameters. This would also enable future work to test whether observed medium-specific differences in α align with measured stringent-response sensitivities [76].

From One-Sector to Multi-Sector Proteome Models.

A natural next step is to replace the dual ribosomal and non-ribosomal sectors with a set of coarse-grained proteome sectors (see Figure 2.3). This would allow explicit reallocation during and after pulses, enable carbon-source-dependent balances, and better isolate supply versus demand constraints when ρ illustrates medium-specific features. Multi-sector formulations can remain low-dimensional while still capturing empirically observed proteome reallocation and efficiency trade-offs, and would more precisely connect transient dosing responses to steady-state growth-law structure [12][129][136]. If additional sectors were incorporated, the dynamic allocation could be encoded through a set of time-dependent proteome fractions whose evolution is constrained by two principles, global conservation of total proteome mass (sector fractions must sum to one) [189], and sector-specific growth laws that describe how each fraction expands or contracts in response to translational demand, metabolic flux, or stress signals such as ppGpp [76][129][136]. In this framework, increases in one sector, such as amino-acid biosynthesis during recovery or envelope stress during inhibition, necessarily draw resources from others. Allocation rules can be written

so that sector growth responds to internal signals (elongation rate, nutrient flux, ppGpp, energy state), allowing sectors to re-equilibrate dynamically during a pulse and recovery. This approach preserves the coarse-grained character of the current model while introducing explicit representation of the trade-offs that drive proteome remodeling under nutrient limitation and antibiotic stress.

Accounting for Fidelity Costs in Protein Synthesis Inhibitors.

While aminoglycosides have previously been modeled within reversible or irreversible binding frameworks [71], their dominant physiological consequence is not depletion of active ribosomes, but reduced translational fidelity that generates nonfunctional or toxic proteins. Extending the present framework to these drugs would therefore require representing the burden of mistranslation rather than modifying binding kinetics alone. A fidelity-aware extension could incorporate an error-dependent reduction in productive protein synthesis, capturing the accumulation of misfolded proteins, the increased demand on proteostasis systems such as chaperones and proteases, and the energetic cost of degrading faulty products [101][7]. These costs act as an additional physiological load rather than direct inhibition of ribosome availability. Consequently, mistranslation would be best encoded as a penalty on productive elongation and on metabolic efficiency, providing a natural extension to multi-sector proteome allocation and to the proportional feedback regulation developed in this thesis.

Generalizing Beyond Ribosome-Targeting Antibiotics.

An important extension is to broaden the framework to other classes of antibiotics. Within protein synthesis inhibitors, the current ribosome-centered model could be adjusted to drugs that target other steps of translation, such as initiation or elongation factors, where the limiting step is not ribosome availability but auxiliary components of the translation cycle [108][228]. In these cases, the same feedback principle would apply, but the controlled process would shift from ribosome synthesis to the synthesis or activity of the relevant factor. For antibiotics that act outside of protein synthesis, such as DNA replication inhibitors (fluoroquinolones) or cell-wall and membrane disruptors (β-lactams and polymyxins), the modeling would require a more fundamental reformulation. Here, the growth-limiting process is no longer translational but instead defined by DNA replication capacity or envelope integrity [9][183][223]. While the feedback principle could still be retained, linking supply–demand mismatches to corrective responses, the variables and feedback rules would differ. For example, in DNA-targeting drugs, the imbalance would

arise between replication demand and nucleotide supply, whereas in cell-wall inhibitors, it would stem from synthesis capacity versus mechanical stress tolerance. In this way, the present work provides a conceptual scaffold for generalization across antibiotic classes. The feedback concept is preserved as the overall idea, while the identity of the growth-limiting process changes according to drug mode of action. Extending the model in this direction would deepen its applicability to various antibiotic strategies and connect stress-specific limitations to general rules of bacterial adaptation [12][76].

Eukaryotic Generalization and Synthetic-Biology Relevance.

Because flux-sensing feedback and resource allocation appear in budding yeast and other eukaryotes, a modified version of the model could be explored in simple eukaryotic systems with appropriate adjustments to transcriptional control and compartmental transport. In parallel, similar resource-allocation constraints link to burden and retroactivity in synthetic circuits. The feedback framework offers a compact methodology to embed host-aware regulation in circuit design or to interpret how antibiotic pulses perturb macromolecular capacity during expression loads [34][129].

6.6.2 Physiology-Informed Antibiotic Strategies

While this thesis focuses on batch-culture experiments with *E. coli* under pulse antibiotic exposure, future work could explore how bacterial physiology and antibiotic response inform broader dosing strategies and resistance mitigation. Antibiotic dosing strategies have evolved from empirical frameworks to precision approaches informed by pharmacokinetics (PK), pharmacodynamics (PD), and system-wide bacterial physiology. The goal remains to optimize therapeutic effectiveness, limit host toxicity, and slow or prevent resistance development. This shift underscores an increasing recognition of how bacterial stress responses and population dynamics shape treatment outcomes. PK describes drug absorption, distribution, metabolism, and excretion in the host, while PD captures the antibiotic's effects on bacterial growth and viability [42][106]. Time-dependent antibiotics, such as β-lactams, require concentrations above the minimum inhibitory concentration (MIC) for extended periods, whereas concentration-dependent antibiotics, such as aminoglycosides, are most effective when peak concentrations considerably exceed the MIC [20][210]. These insights guide strategies such as extended infusions and high-dose, short-duration therapies.

Advances in experimental design have also driven innovation. Devices such as morbidostats maintain bacterial cultures under dynamically adjusted drug concentrations, allowing real-time investigation of resistance evolution and adaptive dosing protocols [209].

Stochastic modeling and chemical-kinetic structures further predict how bacterial populations react to fluctuating drug levels, isolating phenomena such as the inoculum effect and persister formation [4][119][241]. These approaches underline that bacterial survival depends on population heterogeneity, with subpopulations transiently adopting slow-growing or dormant states. Mathematical models of pulse dosing have provided vital insights into these dynamics, particularly for reversible ribosome-targeting antibiotics, which exhibit transient proteomic states characterized by excess ribosome synthesis during exposure and overshoot upon drug removal [72]. These frameworks emphasize that antibiotics with high binding affinity can cause prolonged growth suppression through hysteresis effects in ribosome synthesis, informing candidate selection for pulse-based regimens. Pulsed and intermittent dosing regimens have gathered particular interest for mitigating resistance by exploiting phases of recovery as transient vulnerabilities, potentially intercepting the fixation of resistant mutations [89][128]. These strategies aim to minimize selective pressure while maintaining potency, balancing empirical and mechanistic design.

Combination therapy remains a cornerstone in addressing multi-drug resistant infections (see Figure 6.2). Synergistic drug pairs can improve bactericidal activity, diminish dosing requirements, and limit resistance [39][177]. However, antagonistic interactions can arise, requiring careful assessment of drug compatibility through mechanistic and systems-level experiments [20][70][108]. Computational models increasingly assist in predicting such interactions by linking bacterial metabolic networks and proteome-allocation constraints. Emerging work highlights the importance of bacterial physiology in shaping dosing outcomes. Stress responses, including the SOS response and the ppGpp-mediated stringent response, reconfigure gene expression and proteome composition during antibiotic administration [108][165]. These adaptive shifts influence drug uptake, target modification, and efflux activity, contributing to transient tolerance and necessitating dosing strategies that account for such dynamic proteomic landscapes. Slow-growing cells within biofilms or nutrient-limited niches often display decreased antibiotic penetration and target activity, requiring higher doses or adjunctive therapies for clearance [183]. Pulse dosing may help counteract these effects by temporarily overwhelming these physiological barriers.

In clinical practice, physicians do not directly impose the concentration–time profile delivered to bacteria. Rather than prescribing an exact antibiotic "pulse", treatment choices influence the dynamics indirectly through dosage, dosing frequency, drug formulation, and route of administration. Host pharmacokinetics and pharmacodynamics then determine how quickly the drug reaches and leaves the infection site, while patient adherence further shapes exposure [42][210]. As a result, the *in vivo* concentration profile emerges from the combined effects of delivery route, clearance, and tissue penetration rather than being manually imposed, as in controlled *in vitro* experiments. Physiological modeling there-

fore identifies the regimes in which particular schedules would be effective, while PK/PD constraints dictate whether such regimens are clinically achievable and how closely real treatments can approximate an optimal dosing profile.

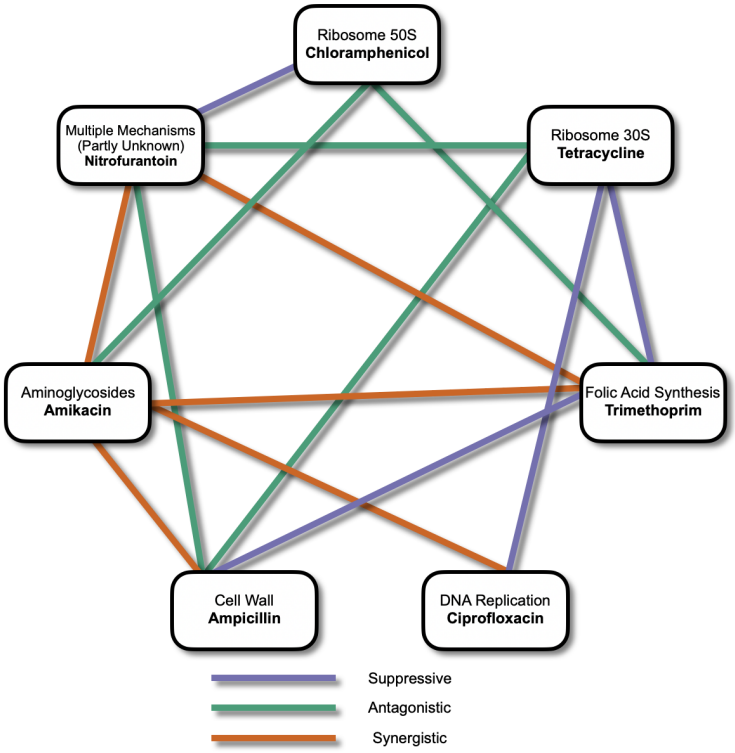


Figure 6.2: Example antibiotic interaction network in *E. coli*. Nodes represent major antibiotic classes labeled by their primary target or mode of action, along with a representative drug. Edges indicate typical drug interactions observed in *E. coli*: suppression (purple), antagonism (green), and synergism (orange). *Reproduced from* [20] *under the terms of the Creative Commons CC BY 4.0 license.*

6.6.3 Resistance Mechanisms and Proteomic Adaptation

The emergence and spread of antibiotic resistance remain one of the most critical challenges in medicine. While the present work focuses on bacterial physiology and growth dynamics under controlled dosing, future extensions may incorporate detailed resistance modeling, including proteomic and evolutionary mechanisms. Combating resistance demands a multifaceted approach that integrates pharmacodynamics, bacterial physiology,

evolutionary theory, and systems-level proteomics. Proteomic shifts under antibiotic stress include upregulation of efflux pumps, remodeling of targets, activation of protective stress factors, and metabolic reconfiguration to bypass inhibited pathways [59][202]. For example, exposure to sublethal antibiotic concentrations can trigger the stringent response mediated by ppGpp, leading to reduced ribosomal protein synthesis and global reprogramming of protein expression [76][101]. These responses, though initially protective, can lay the foundation for heritable resistance mutations. Suppressive drug interactions further reveal that misregulation of ribosomal genes during DNA stress can paradoxically enhance growth under protein synthesis inhibition [21]. This finding highlights that the balance between DNA repair and protein production is critical for bacterial survival under multi-drug pressure.

Innovative dosing strategies, including pulsed, sequential, and gradient methodologies, aim to disrupt bacterial adaptation and intercept the selection of resistant mutants [70][128]. Leveraging phases of vulnerability allows for more efficient clearance with reduced total drug exposure. Mechanistic and stochastic models reveal how phenotypic variability and single-cell fluctuations facilitate resistance emergence [119]. Systems biology studies also demonstrate that shifts in proteomic and metabolic landscapes, particularly under nutrient limitation or stress, can promote tolerance and persistence phenotypes [161][165]. These transient phenotypes often serve as reservoirs from which genetic resistance can evolve. Combination therapies remain an indispensable tool in resistance management, with synergistic pairings boosting bactericidal activity and certain antagonistic interactions paradoxically slowing resistance spread [2][39]. However, poorly designed combinations can promote stress-induced mutagenesis or horizontal gene transfer, accelerating resistance dissemination [112][237]. Proteomic profiling aids in predicting these interactions by revealing how resource allocation shifts in response to drug pairs. Targeting persistence and non-heritable resistance mechanisms is an emerging strategy to improve antibiotic efficacy. Phenotypic heterogeneity within bacterial populations, often tied to proteome variability, allows subsets of cells to survive antibiotic treatment without acquiring genetic mutations [7][165]. Approaches that interfere with these tolerances, such as blocking stress-response regulators or ribosomal assembly factors, may synergize with conventional antibiotics.

Environmental and ecological factors also play a critical role in resistance evolution. Pollutant antibiotics in wastewater, for instance, create low-level exposures that enable bacterial communities to develop resistance through proteome-level adaptation [237]. A substantial share of global antibiotic use occurs in livestock production, where drugs are routinely administered at low or moderate doses for prophylaxis and growth promotion rather than acute treatment. These prolonged subinhibitory exposures select for tolerance, metabolic remodeling, and slow-growth phenotypes [107][224]. Such selective environments resemble sustained metabolic limitation more closely than therapeutic inhibition,

and therefore parallel the proteome restructuring that drives delay time after reversible inhibition. In clinical medicine, by contrast, pharmacokinetics and adherence constraints impose shorter, higher-intensity exposures that induce transient physiological adaptation without prolonged selection pressure. Understanding how reversible inhibition produces metabolic limitation and proteome reshaping can therefore clarify why resistance emergence is disproportionately linked to agricultural use despite the clinical importance of treatment misuse [216]. Together, these perspectives emphasize that bridging physiological insights and clinical translation is essential for designing durable, resistance-aware therapies. Continued refinement across scales, from molecular signaling to ecological exposure regimes, will help clarify how resource allocation and stress adaptation shape bacterial resilience, guiding more predictive and physiology-based approaches to antibiotic therapy.

6.6.4 Generalizability and Robustness of the Framework

The modeling framework developed in this thesis is not confined to the specific experimental conditions used to study tetracycline exposure in *E. coli*. Its core assumptions rely on two features that extend across diverse bacterial species in exponential growth. First, the steady-state growth laws (3.1) and (3.2) are independent of species identity (not unique to *E. coli*) so long as balanced growth is maintained. The linear relation between ribosome mass fraction and growth rate, and the metabolic-limit relation when translational capacity is high, have been quantified across multiple bacterial strains growing in different nutrients (see Supplementary Information of [189]). Second, the antibiotic–ribosome interaction model (3.3) depends only on reversible binding kinetics and target sequestration. These mechanisms describe ribosome-targeting drugs broadly and are not specific to tetracycline or to *E. coli* as long as the drug reversibly inhibits translation through ribosomal binding [71]. What is not generalizable is the dynamic synthesis rate that governs feedback control. The proportional synthesis controller introduced in this work describes how ribosome production responds to shifts in translational demand and nutrient supply. The proportional gains must reflect the regulatory landscape of the organism and nutrient environment under study, and therefore require empirical calibration. In this sense, the growth laws and binding kinetics are transferable, while the feedback strengths must be determined experimentally if applied to other species or conditions.

The predictive robustness of the model is reinforced by the quantity

$$K = \frac{\mathrm{AUC}}{\mathrm{IC}_{50}},$$

which arises from the piecewise exponential structure of the pulse–recovery trajectories.

The plateau in $\Delta t \to K$ does not rely on any parameter fitting and does not depend on the detailed synthesis dynamics. It reflects a balance between the inhibitory effect during exposure and the regrowth dynamics after removal. Because both AUC and IC_{50} can be measured independently of the model, the transition point $T^* \approx K$ does not require model inference and can be validated experimentally. This strengthens the interpretation of T^* as an optimal pulse length that maximizes inhibition without unnecessary exposure. The shape of the output trajectories further supports this mechanism. For short pulses, the mismatch between the pre- and post-pulse exponential regimes is large, and Δt increases nearly linearly with exposure duration. As pulse length increases, the gap between these regimes becomes smaller, and the sharp transitions that distinguish pulse and recovery diminish. Eventually, at long exposure, the two exponential segments converge and Δt approaches the plateau at K. This qualitative behaviour holds regardless of the feedback controller and depends only on the separation of antibiotic-bound and drug-free exponential dynamics. Figure 6.3 illustrates this convergence for three representative pulse lengths. The shrinking gap demonstrates how the model predicts an optimal pulse without requiring fine-tuning of physiological parameters.

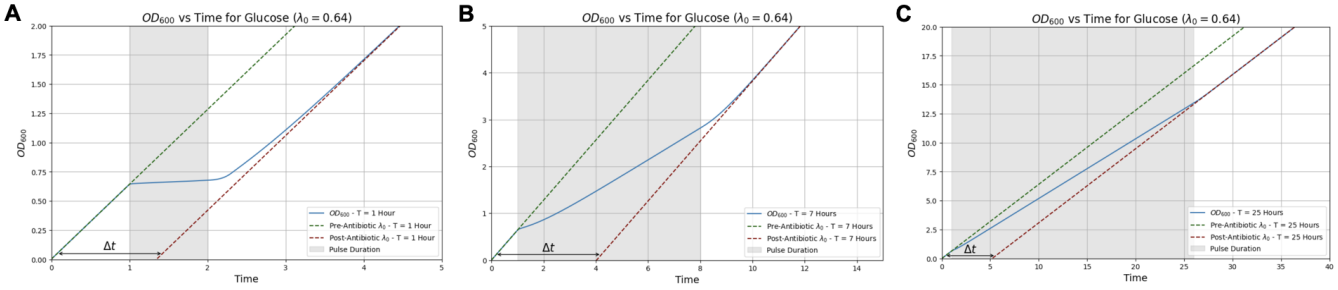


Figure 6.3: Illustration Δt for three pulse durations in glucose medium: a short pulse ($T = 1\,h$), the near-optimal regime ($T = 7\,h$), and a long pulse ($T = 25\,h$). Each panel shows the optical density trajectory (solid blue curve) together with the pre-pulse and post-pulse exponential fits (dashed green and red lines). The black arrow highlights Δt, which decreases as T increases and approaches a plateau as inhibition saturates. For long pulses, the two exponential regimes nearly coincide, the corner between them becomes negligible, and the sharp transition can be discarded. Thus, the saturation of Δt emerges independently of the piecewise construction of the OD curve.

Chapter 7

Conclusion

This chapter summarizes the major outcomes and broader significance of the work presented in this thesis. Building upon the steady-state framework of nutrient and antibiotic growth laws, the research developed a unified dynamic model that connects bacterial physiology, proteome reallocation, and antibiotic pulse response. Through progressive refinement, beginning with the correction of post-pulse growth limitation, followed by the introduction of dynamic synthesis feedback, the model evolved into a physiologically interpretable system that reconciles theoretical predictions with experimental data. The results demonstrate that bacterial recovery and adaptation follow a proportional, feedback-driven logic linking ribosome synthesis, amino acid availability, and antibiotic stress. The following sections outline the principal contributions, broader implications, and general insights arising from this framework.

7.1 Summary of Contributions

This thesis has developed, refined, and validated a dynamical model that links bacterial growth physiology with antibiotic pulse response. The central biological contribution is the demonstration that recovery after a ribosome-targeting antibiotic pulse is limited not by ribosome stock but by nutrient-driven proteome reallocation. Capturing this adjustment in the growth-limiting sector resolves the unphysical post-pulse overshoot observed in earlier models and aligns recovery dynamics with experimental observations. To represent this mechanism and accommodate the rapid timescale of adaptation, the model incorporates a proportional feedback controller that integrates nutrient- and antibiotic-limiting regimes within a single control formulation. Several additional contributions arise from this work:

1. **Mechanistic Clarity.** The model does not merely fit experimental data but provides mechanistic explanations for observed behaviours, including the plateau of delay time at long pulse durations, the RNA/protein recovery trajectories, and the influence of nutrient environment on antibiotic response. These outcomes emerge directly from feedback between translational demand and amino acid supply, highlighting the physiological role of ppGpp-mediated control.

2. **Unification of Regimes.** By embedding nutrient-dependent parameters (κ_N, κ_T, λ_0), the model reproduces antibiotic-limited growth under both glucose and glycerol without requiring separate formulations. This demonstrates that nutrient and antibiotic stress share a unifying control principle rooted in bacterial physiology.

3. **Quantitative Explanation of Delay Time Plateau.** Analysis of fitted delay time curves revealed scaling with pulse duration only up to a critical threshold, beyond which delay saturates. This arises from the effective pulse intensity,

$$a_{\text{ex}} = \frac{K \cdot \text{IC}_{50}}{T},$$

   which declines as duration T increases. For long pulses ($T \gg 8\,h$), the per-hour antibiotic concentration becomes negligible, allowing near-complete regrowth before the pulse ends. This analysis resolves why recovery delay saturates experimentally and clarifies why overly prolonged, low-intensity pulses are physiologically ineffective.

4. **Integration of Multiple Datasets.** The proportional feedback synthesis model accounts simultaneously for delay times, RNA/protein ratios, and inhibition curves using a single parameter set. This demonstrates that the model captures genuine physiological constraints rather than relying on independent curve fits, strengthening confidence in its predictive power.

5. **Methodological Innovation.** This work advances bacterial physiology modeling by combining growth laws, proteome partitioning, and stress adaptation within a dynamic feedback system. Sensitivity and Hessian analyses provide a systematic understanding of which parameter combinations are tightly constrained and which admit compensatory flexibility, clarifying the underlying physiological structure of the model.

Taken together, these contributions provide a consolidated and biologically interpretable model of antibiotic pulse response, bridging classical growth laws, modern proteome partitioning, and dynamic stress adaptation physiology.

7.2 Broader Implications

Beyond the technical details, the significance of this work lies in how it reframes bacterial stress adaptation and antibiotic response in both basic and applied contexts. The proportional feedback provides a mechanistic explanation for how *E. coli* recovers following translational inhibition, where delay time scaling, RNA/protein ratio adjustment, and inhibition profiles emerge naturally from the balance between supply and demand. These dynamics are consistent with ppGpp-mediated transcriptional regulation and reveal underlying physiological principles that are difficult to access directly in experiments. The same feedback mechanism that drives adaptation under glucose and glycerol also explains recovery from antibiotic pulses, reinforcing that proteome reallocation represents a universal organizing principle of bacterial physiology, regardless of whether stress arises from nutrient scarcity or translational inhibition. Therapeutically, the model shows that extending pulse duration beyond a critical threshold yields reduced effectiveness, as cells begin recovering during the pulse itself. This result emphasizes that appropriately intensified pulse dosing can maximize inhibition while minimizing total drug exposure, thereby reducing toxicity and selective pressure for resistance. Such insights align with pharmacokinetic and pharmacodynamic frameworks, underscoring that binding–transport balance and recovery kinetics are as critical as extracellular concentration in determining efficacy. The plateau in delay time may even represent an evolved strategy, allowing cells to minimize the metabolic cost of prolonged stress while preserving growth potential. This suggests that low-dose, extended exposures could promote tolerance rather than eradication, with implications for microbial ecology and resistance evolution in biofilms, environmental niches, and clinical contexts. Here, tolerance refers to a reversible physiological slowdown governed by proteome reallocation and synthesis feedback, distinct from genetic resistance, which arises from heritable mutations that alter antibiotic binding or transport. While the present model captures only the physiological component, such dynamics can shape the ecological and temporal conditions under which resistance is selected.

The framework developed here also provides predictive capacity for experimental design. By simulating unexplored pulse durations and concentrations, the model can identify regimes most likely to reveal differences in proteome allocation or ppGpp regulation across nutrient conditions. This capability enables targeted hypothesis testing and efficient experimental planning. Although this work focused on *E. coli* and tetracycline, the feedback formulation and delay plateau dynamics are likely generalizable to other bacterial species and translation-targeting antibiotics. Extensions to high-affinity drugs, alternative translation mechanisms, or DNA-type stresses could reveal how broadly this physiological logic applies, with possible relevance to synthetic biology and precision medicine. Finally, this

thesis contributes methodologically by demonstrating how coarse-grained but physiologically grounded models can reconcile diverse datasets into a coherent framework, providing a foundation for future efforts that integrate molecular mechanisms, physiological responses, and therapeutic strategies. Overall, this thesis demonstrates that bacterial adaptation to antibiotic stress can be understood through a unifying physiological framework grounded in proteome balance and feedback control. By bridging theoretical modeling with experimental validation, the work advances both mechanistic understanding and translational relevance. The proportional feedback formulation provides not only a refined description of growth recovery under antibiotic pulses but also a general principle for interpreting cellular adaptation across environmental and therapeutic contexts. In doing so, this research contributes to the broader goal of integrating quantitative modeling, molecular physiology, and rational antibiotic design into a cohesive foundation for future investigation. Together, these insights reaffirm that even in the complexity of bacterial stress and recovery, growth remains governed by a simple principle of balance.

References

[1] Akaike, H. A new look at the statistical model identification. *IEEE Transactions on Automatic Control 19*, 6 (1974), 716–723.

[2] Allen, R., and Waclaw, B. Antibiotic resistance: a physicist's view. *Physical Biology 13*, 4 (2016).

[3] Angermayr, S. A., et al. Growth-mediated negative feedback shapes quantitative antibiotic response. *Molecular System Biology 18*, 9 (2022).

[4] Baeder, D. Y., and Regoes, R. R. The pharmacodynamic inoculum effect from the perspective of bacterial population modeling. *bioRxiv* (2025). Preprint. DOI: https://doi.org/10.1101/550368.

[5] Baek, J. H., and Lee, S. Y. Transcriptome Analysis of Phosphate Starvation Response in *Escherichia coli*. *Journal of Microbiology and Biotechnology 17*, 2 (2006), 244–252.

[6] Bakshi, S., et al. Tracking bacterial lineages in complex and dynamic environments with applications for growth control and persistence. *Nature Microbiology 6* (2021), 783–791.

[7] Balaban, N. Q., et al. Bacterial Persistance as a Phenotypic Switch. *Science 305*, 5690 (2004), 1622–1625.

[8] Ball, C. A., et al. Dramatic Changes in Fis Levels upon Nutrient Upshift in *Escherichia coli*. *Bacteriology 174*, 24 (1992), 8043–8056.

[9] Banerjee, S., et al. Mechanical feedback promotes bacterial adaptation to antibiotics. *Nature Physics 17* (2021), 403–409.

[10] Baranyi, J., and Roberts, T. A. A dynamic approach to predicting bacterial growth in food. *International Journal of Food Microbiology 23*, 3-4 (1994), 277–294.

[11] Baron, S. *Medical Microbiology.* Addison-Wesley Publishing Company Inc., California, 1982.

[12] Basan, M., et al. Overflow metabolism in *Escherichia coli* results from efficient proteome allocation. *Nature 528* (2015), 99–104.

[13] Baym, M., et al. Multidrug evolutionary strategies to reverse antibiotic resistance. *Science 351*, 6268 (2016).

[14] Belliveau, N. M., et al. Fundamental limits on the rate of bacterial growth and their influence on proteomic composition. *Cell Systems 12*, 9 (2021), 924–944.

[15] Benthin, S., et al. A simple and reliable method for the determination of cellular RNA content. *Biotechnology Techniques 5*, 1 (1991), 39–42.

[16] Berg, H. C. Motile Behavior of Bacteria. *Physics Today 53*, 1 (2000), 24–29.

[17] Berkhout, J., et al. How Biochemical Constraints of Cellular Growth Shape Evolutionary Adaptations in Metabolism. *Genetics 194*, 2 (2013), 505–512.

[18] Berthoumieux, S., et al. Shared control of gene expression in bacteria by transcription factors and global physiology of the cell. *Molecular Systems Biology 9* (2013).

[19] Bevington, P. R., and Robinson, D. K. *Data Reduction and Error Analysis for the Physical Sciences*, 3 ed. McGraw-Hill, 2003.

[20] Bollenbach, T. Antimicrobial interactions: mechanisms and implications for drug discovery and resistance. *Current Opinion in Microbiology 27* (2015), 1–9.

[21] Bollenbach, T., et al. Nonoptimal Microbial Response to Antibiotics Underlies Suppressive Drug Interactions. *Cell 139*, 4 (2009), 707–718.

[22] Boyd, S., and Vandenberghe, L. *Convex Optimization.* Cambridge University Press, 2004.

[23] Braniff, N., et al. Component Characterization in a Growth-Dependent Physiological Context: Optimal Experimental Design. *Processes 7*, 1 (2019).

[24] Braz, V. S., et al. *Escherichia coli* as a Multifaceted Pathogenic and Versatile Bacterium. *Frontiers in Cellular and Infection Microbiology 10* (2020).

[25] Bremer, H., and Churchward, G. An Examination of the Cooper-Helmstetter Theory of DNA Replication in Bacteria and its Underlying Assumptions. *Journal of Theoretical Biology 69*, 4 (1977), 645–654.

[26] Bremer, H., and Dennis, P. Modulation of Chemical Composition and Other Parameters of the Cell by Growth Rate. *Escherchia coli and Salmonella: Cellular and Molecular Biology 2* (1996).

[27] Bren, A., et al. Tradeoffs in bacterial physiology determine the efficiency of antibiotic killing. *PNAS 120*, 51 (2023).

[28] Brodersen, D. E., et al. The Structural Basis for the Action of the Antibiotics Tetracycline, Pactamycin, and Hygromycin B on the 30S Ribosomal Subunit. *Cell 103*, 7 (2000), 1143–1154.

[29] Bruslind, L. *General Micrbiology*. Oregon State University, Corvallis, 2019.

[30] Buchanan, R. E. Life Phases in a Bacterial Culture. *Journal of Infectious Diseases 23*, 2 (1918), 109–125.

[31] Bundtzen, R. W., et al. Postantibiotic Suppression of Bacterial Growth. *Reviews of Infectious Diseases 3*, 1 (1981), 28–37.

[32] Cama, J., et al. Single-cell microfluidics facilitates the rapid quantification of antibiotic accumulation in Gram-negative bacteria. *Lab on a Chip 20*, 15 (2020), 2765–2775.

[33] Cardinale, S., et al. Effects of Genetic Variation on the *E. coli* Host-Circuit Interface. *Cell Reports 4*, 2 (2013), 231–237.

[34] Ceroni, F., Boo, A., et al. Burden-driven feedback control of gene expression. *Nature Methods 15*, 5 (2018), 387–393.

[35] Champney, W. S. The Other Target for Ribosomal Antibiotics: Inhibition of Bacterial Ribosomal Subunit Formation. *Infectious Disorders - Drug Targets 6*, 4 (2006), 377–390.

[36] Champney, W. S. Antibiotics targeting bacterial ribosomal subunit biogenesis. *Journal of Antimicrobial Chemotherapy 75*, 4 (2020), 787–806.

[37] Chen, K., et al. Bacterial fitness landscapes stratify based on proteome allocation associated with discrete aero-types. *PLoS Computational Biology 17*, 1 (2021).

[38] Chen, W., et al. Universal, untargeted detection of bacteria in tissues using metabolomics workflows. *Nature Communications 16*, 165 (2025).

[39] Chevereau, G., and Bollenbach, T. Systematic discovery of drug interaction mechanisms. *Molecular Systems Biology 11*, 4 (2015).

[40] Chou, C. P. Engineering cell physiology to enhance recombinant protein production in *Escherichia coli*. *Applied Microbiology and Biotechnology 76*, 3 (2007), 521–532.

[41] Cooper, S., and Helmstetter, C. E. Chromosome Replication and the Division Cycle of *Escherichia coli* B/r. *Journal of Molecular Biology 31*, 3 (1968), 519–540.

[42] Craig, W. Pharmacodynamics of antimicrobial agents as a basis for determining dosage regimens. *European Journal of Clinical Microbiology & Infectious Diseases 12*, 1 (1993), 6–8.

[43] Cylke, K. C., et al. Effects of antibiotics on bacterial cell morphology and their physiological origins. *Biochemistry Society Transactions 50*, 5 (2022), 1269–1279.

[44] Dai, X., et al. Reduction of translating ribosomes enables *Escherichia coli* to maintain elongation rates during slow growth. *Nature Microbiology 2* (2016).

[45] Davies, J., and Davies, D. Origins and Evolution of Antibiotic Resistance. *Microbiology and Molecular Biology Reviews 74*, 3 (2010), 417–433.

[46] Davis, J. H., and Williamson, J. R. Structure and dynamics of bacterial ribosome biogenesis. *Philosophical Transactions of the Royal Society B 372*, 1716 (2017).

[47] de Jong, H., et al. Mathematical modelling of microbes: metabolism, gene expression and growth. *Journal of the Royal Society Interface 14* (2017).

[48] De Vos, D., et al. How Molecular Competition Influences Fluxes in Gene Expression Networks. *PLoS ONE 6*, 12 (2011).

[49] Dennis, P. P., and Bremer, H. Differential Rate of Ribosomal Protein Synthesis in *Escherichia coli* B/r. *Journal of Molecular Biology 84*, 3 (1974), 407–422.

[50] Deris, J. B., et al. The innate growth bistability and fitness landscapes of antibiotic resistant bacteria. *Science 342*, 6162 (2013).

[51] Doolittle, W. F. Phylogenetic classification and the universal tree. *Science 284*, 5423 (1999), 2124–2129.

[52] Doolittle, W. F., and Brown, J. R. Tempo, Mode, the Prokaryote/Eukaryote Dichotomy, and the Root of the Universal Tree. *PNAS 91*, 15 (1994), 6721–6728.

[53] Edelstein-Keshet, L. *Mathematical Models in Biology.* Society for Industrial and Applied Mathematics, 2005.

[54] El-Sharoud, W. *Bacterial Physiology: A Molecular Approach.* Springer, Berlin, 2008.

[55] Elf, J., et al. Bistable Bacterial Growth Rate in Response to Antibiotics with Low Membrane Permeability. *Physical Review Letters 97*, 25 (2006).

[56] Erickson, D. W., et al. A global resource allocation strategy governs growth transition kinetics of *Escherichia coli*. *Nature 551* (2017), 119–123.

[57] Faizi, M., et al. A model of optimal protein allocation during phototrophic growth. *Biosystems 166* (2018).

[58] Falkowski, P. G., et al. The Microbial Engines That Drive Earth's Biogeochemical Cycles. *Science 320*, 5879 (2008), 1034–1039.

[59] Fange, D., et al. Drug efflux pump deficiency and drug target resistance masking in growing bacteria. *PNAS 106*, 20 (2009), 8215–8220.

[60] Ferenci, T. 'Growth of bacterial cultures' 50 years on: towards an uncertainty principle instead of constants in bacterial growth kinetics. *Research in Microbiology 150*, 7 (1999), 431–438.

[61] Flemming, H. C., and Wingender, J. The biofilm matrix. *Nature Reviews Microbiology 8* (2010), 623–633.

[62] Flensburg, J., and Sköld, O. Massive overproduction of dihydrofolate reductase in bacteria as a response to the use of trimethoprim. *European Journal of Biochemistry 162*, 3 (1987), 473–476.

[63] Folsom, J. P., and Carlson, R. P. Physiological, biomass elemental composition and proteomic analyses of *Escherichia coli* ammoniumlimited chemostat growth, and comparison with iron- and glucose-limited chemostat growth. *Microbiology 161*, 8 (2015), 1659–1670.

[64] Frenkiel-Krispin, D., et al. Nucleoid restructuring in stationary-state bacteria. *Molecular Microbiology 51*, 2 (2004), 395–405.

[65] Geigenmüller, U., and Neirhaus, K. H. Tetracycline can inhibit tRNA binding to the ribosomal P site as well as to the A site. *European Journal of Biochemistry 161*, 3 (1986), 723–726.

[66] Giordano, N., et al. Dynamical Allocation of Cellular Resources as an Optimal Control Problem: Novel Insights into Microbial Growth Strategies. *PLoS Computational Biology 12*, 3 (2016).

[67] Goelzer, A., et al. Cell design in bacteria as a convex optimization problem. *Automatica 47*, 6 (2011), 1210–1218.

[68] Graber, E. M. Treating acne with the tetracycline class of antibiotics: A review. *Dermatological Reviews 2*, 6 (2021), 321–330.

[69] Gray, M. W., et al. The Origin and Early Evolution of Mitochondria. *Genome Biology 2*, 6 (2001).

[70] Greulich, P., et al. Mutational Pathway Determines Whether Drug Gradients Accelerate Evolution of Drug-Resistant Cells. *Physical Review Letters 109*, 8 (2012).

[71] Greulich, P., et al. Growth-dependent bacterial susceptibility to ribosome-targeting antibiotics. *Molecular Systems Biology 11*, 3 (2015).

[72] Greulich, P., et al. Predicting the dynamics of bacterial growth inhibition by ribosome-targeting antibiotics. *Physical Biology 14*, 6 (2017).

[73] Gutenkunst, R. N., et al. Universally Sloppy Parameter Sensitivities in Systems Biology Models. *PLoS Computational Biology 2*, 10 (2007), 1871–1878.

[74] Hall-Stoodley, L., et al. Bacterial Biofilms: From the Natural Environment to Infectious Diseases. *Nature Reviews Microbiology 2*, 2 (2004), 95–108.

[75] Harvey, R. J. Growth and Initiation of Protein Synthesis in *Escherichia coli* in the Presence of Trimethoprim. *Journal of Bacteriology 114*, 1 (1973), 309–322.

[76] Hauryliuk, V., et al. Recent functional insights into the role of (p)ppGpp in bacterial physiology. *Nature Reviews Microbiology 13* (2015), 298–309.

[77] Helmstetter, C. E. A ten-year search for synchronous cells: obstacles, solutions, and practical applications. *Frontiers in Microbiology 6* (2015).

[78] Helmstetter, C. E., and Cooper, S. DNA Synthesis during the Division Cycle of Rapidly Growing *Escherichia coli* B/r. *Journal of Molecular Biology 31*, 3 (1968), 507–518.

[79] Herbert, D., et al. Chemical analysis of microbial cells. In *Methods in Microbiology*, vol. 5. Academic Press, 1971, pp. 209–344.

[80] Hermsen, R., et al. On the rapidity of antibiotic resistance evolution facilitated by a concentration gradient. *PNAS 109*, 27 (2012), 10775–10780.

[81] Hermsen, R., et al. A growth-rate composition formula for the growth of *E. coli* on co-utilized carbon substrates. *Molecular Systems Biology 11*, 4 (2015).

[82] Hirsch, M. W., et al. *Differential Equations, Dynamical Systems, and an Introduction to Chaos*, 3 ed. Elsevier Inc., 2013.

[83] Hug, L. A., et al. A new view of the tree of life. *Nature Microbiology 1*, 5 (2016).

[84] Hungate, R. E., et al. Bacteria. *AccessScience* (2023). Retrieved February 23, 2025, from https://doi.org/10.1036/1097-8542.068100.https://www.accessscience.com/content/article/a068100.

[85] Jacob, F., and Monod, J. Genetic regulatory mechanisms in the synthesis of proteins. *Journal of Molecular Biology 3*, 3 (1961), 318–356.

[86] Jaramillo-Riveri, S., et al. Growth-dependent heterogeneity in the DNA damage response in *Escherchia coli*. *Molecular Systems Biology 18*, 5 (2022).

[87] Jun, S., et al. Fundamental Principles in Bacterial Physiology - History, Recent progress, and the Future with Focus on Cell Size Control: A Review. *Reports on Progress in Physics 81*, 5 (2018).

[88] Juška, A., et al. Growth of Microbial Populations. Mathematical Modeling, Laboratory Exercises, and Model-Based Data Analysis. *Biochemistry and Molecular Biology Education 34*, 6 (2006), 417–422.

[89] Kavčič, B., et al. Minimal biophysical model of combined antibiotic action. *PLoS Computational Biology 17*, 1 (2021).

[90] Kim, J., et al. Trade-offs between gene expression, growth and phenotypic diversity in microbial populations. *Current Opinion in Biotechnology 62* (2020), 29–37.

[91] Kjeldgaard, N. O., et al. The Transition Between Different Physiological States During Balanced Growth of *Salmonella typhimurium*. *Microbiology 19*, 3 (1958), 607–616.

[92] Kleijn, I. T., et al. A coarse-grained resource allocation model of carbon and nitrogen metabolism in unicellular microbes. *Journal of the Royal Society Interface 20*, 206 (2023).

[93] Klumpp, S., et al. Growth rate-dependent global effects on gene expression in bacteria. *Cell 139*, 7 (2009), 1366–1375.

[94] Klumpp, S., et al. Molecular crowding limits translation and cell growth. *Proceedings of the National Academy of Sciences 110*, 42 (2013), 16754–16759.

[95] Knoll, A. H. *Life on a Young Planet: The First Three Billion Years of Evolution on Earth - Updated Edition*. Princeton University Press, 2015.

[96] Koch, A. L. Turbidity Measurements of Bacterial Cultures in Some Available Commercial Instruments. *Analytical Biochemistry 38*, 2 (1970), 252–259.

[97] Koch, A. L. Microbial Physiology and Ecology of Slow Growth. *Microbiology and Molecular Biology Reviews 61*, 3 (1997), 305–318.

[98] Koch, A. L., and Gross, G. H. Growth Conditions and Rifampin Susceptibility. *Antimicrobial Agents and Chemotherapy 15*, 2 (1979), 220–228.

[99] Kochanowski, K., et al. Functioning of a metabolic flux sensor in *Escherichia coli*. *PNAS 110*, 3 (2013), 1130–1135.

[100] Kohanim, Y. K., et al. A Bacterial Growth Law out of Steady State. *Cell Reports 23*, 10 (2018), 2891–2900.

[101] Kohanski, M. A., et al. Sub-lethal antibiotic treatment leads to multidrug resistance via radical-induced mutagenesis. *Molecular Cell 37*, 3 (2010), 311–320.

[102] Kollerová, S., et al. Phenotypic resistant single-cell characteristics under recurring ampicillin antibiotic exposure in *Escherichia coli*. *mSystems 9*, 7 (2024).

[103] Kostinski, S., and Reuveni, S. Growth laws and invariants from ribosome biogenesis in lower Eukarya. *Physical Review Research 3* (2021).

[104] Kotte, O., et al. Bacterial adaptation through distributed sensing of metabolic fluxes. *Molecular Systems Biology 6* (2010).

[105] LeBel, M., and Spino, M. Pulse Dosing Versus Continuous Infusion of Antibiotics. Pharmacokinetic-Pharmacodynamic Considerations. *Clinical Pharmacokinetics 14* (1988), 71–95.

[106] Levison, M. E., and Levison, J. H. Pharmacokinetics and Pharmacodynamics of Antibacterial Agents. *Infectious Disease Clinics of North America 23*, 4 (2009), 791–815.

[107] Levy, S. B., and Marshall, B. Antibacterial resistance worldwide: causes, challenges and responses. *Nature Medicine 10*, 12 (2004), 122–129.

[108] Lin, W.-H., and Kussell, E. Complex interplay of physiology and selection in the emergence of antibiotic resistance. *Current Biology 26*, 11 (2016), 1486–1493.

[109] Lindemann, D., et al. Microbial single-cell growth response at defined carbon limiting conditions. *RSC Advances 9*, 25 (2019), 14040–14050.

[110] Ling, J., et al. Aminoacyl-tRNA Synthesis and Translational Quality Control. *Annual Review of Microbiology 63* (2009), 61–78.

[111] Lodish, H., et al. *Molecular Cell Biology*, 5th ed. W. H. Freeman, New York, 2004.

[112] Lopatkin, A. J., et al. Dissecting the effects of antibiotics on horizontal gene transfer: Analysis suggests a critical role of selection dynamics. *Bioessays 38*, 12 (2016), 1283–1292.

[113] Lopatkin, A. J., et al. Bacterial metabolic state more accurately predicts antibiotic lethality than growth rate. *Nature Microbiology 4* (2019), 2109–2117.

[114] MacKenzie, F. M., and Gould, I. M. The post-antibiotic effect. *Journal of Antimicrobial Chemotherapy 32*, 4 (1993), 519–537.

[115] Madigan, M. T., et al. *Brock Biology of Microorganisms*, 15th ed. Pearson, 2018.

[116] Maguire, B. A. Inhibition of Bacterial Ribosome Assembly: A Suitable Drug Target? *Microbiology and Molecular Biology Reviews 73*, 1 (2009), 22–35.

[117] Maitra, A., and Dill, K. A. Modeling the Overproduction of Ribosomes when Antibacterial Drugs Act on Cells. *Biophysical Journal 110*, 3 (2016), 743–748.

[118] Maki, Y., et al. Two proteins, *YfiA* and *YhbH*, associated with resting ribosomes in stationary phase *Escherichia coli*. *Genes to Cells 5*, 12 (2000), 965–974.

[119] Mansour, M. B. A. Stochastic Modeling of Bacterial Growth and Antimicrobial Resistance. *Journal of Statistical Physics 190*, 8 (2023).

[120] Margulis, L. *Origin of Eukaryotic Cells.* Yale University Press, 1970.

[121] Marr, A. G. Growth Rate of *Escherichia coli*. *Microbiological Reviews 55*, 2 (1991), 316–333.

[122] Martinez-Antonio, A. Protein and mRNA levels support the notion that a genetic regulatory circuit controls growth phases in *E. coli* populations. *Network Biology 5*, 3 (2015), 82–94.

[123] Mateus, A., et al. The functional proteome landscape of *Escherichia coli*. *Nature 588* (2020), 473–478.

[124] McCoy, L. S., et al. Antibiotics that target protein synthesis. *Wiley Interdisciplinary Reviews: RNA 2*, 2 (2011), 209–232.

[125] McGary, K., and Nudler, E. RNA polymerase and the Ribosome: The Close Relationship. *Current Opinion in Microbiology 16*, 2 (2013), 112–117.

[126] Mehta, R., and Champney, W. S. 30S Ribosomal Subunit Assembly Is a Target for Inhibition by Aminoglycosides in *Escherichia coli*. *Antimicrobial Agents and Chemotherapy 46*, 5 (2002), 1546–1549.

[127] Menninger, J. R. Mechanism of inhibition of protein synthesis by macrolide and lincosamide antibiotics. *Journal of Basic and Clinical Physiology and Pharmacology 6*, 3-4 (1995), 229–250.

[128] Meredith, H. R., et al. Bacterial Temporal Dynamics Enable Optimal Design of Antibiotic Treatment. *PLoS Computational Biology 11*, 4 (2015).

[129] Metzl-Raz, E., et al. Principles of cellular resource allocation revealed by condition-dependent proteome profiling. *eLife 6* (2017).

[130] Michaelis, L., and Menten, M. L. Die kinetik der invertinwirkung. *Biochemische Zeitschrift 49* (1913), 333–369.

[131] Molenaar, D., et al. Shifts in growth strategies reflect tradeoffs in cellular economics. *Molecular Systems Biology 5* (2009).

[132] Monod, J. The Growth of Bacterial Cultures. *Annual Review of Microbiology 3* (1949), 371–394.

[133] Mori, M., et al. Quantifying the benefit of a proteome reserve in fluctuating environments. *Nature Communications 8* (2017).

[134] Mori, M., et al. A yield-cost trade-off governs *Escherichia coli*'s decision between fermentation and respiration in carbon-limited growth. *npj Systems Biology and Application 5*, 16 (2019).

[135] Mori, M., et al. From coarse to fine: The absolute *Escherichia coli* proteome under diverse growth conditions. *Molecular Systems Biology 17*, 5 (2021).

[136] Mori, M., et al. Proteome partitioning constraints in long-term laboratory evolution. *Nature Communications 15* (2024).

[137] Murray, J. D. *Mathematical Biology I. An Introduction*, 3 ed. Springer New York, 2002.

[138] Neidhardt, F., et al. Culture Medium for Enterobacteria. *Journal of Bacteriology 119*, 3 (1974), 736–747.

[139] Neidhardt, F. C. Bacterial Growth: Constant Obsession with dN/dt. *Journal of Bacteriology 181*, 24 (1999), 7405–7408.

[140] Neidhardt, F. C., et al. *Physiology of the Bacterial Cell: A Molecular Approach.* Sinauer Associates Inc., Sunderland, 1990.

[141] Neidhardt, F. C., and Magasanik, B. Studies on the role of ribonucleic acid in the growth of bacteria. *Biochimica et Biophysica Acta 42* (1960), 99–116.

[142] Neupert, J., et al. Design of simple synthetic RNA thermometers for temperature-controlled gene expression in *Escherichia coli*. *Nucleic Acids Research 36*, 19 (2008).

[143] Nguyen, J., et al. A distinct growth physiology enhances bacterial growth under rapid nutrient fluctuations. *Nature Communications 12* (2021).

[144] Noeske, J., et al. High-resolution structure of the *Escherichia coli* ribosome. *Nature Structural & Molecular Biology 22*, 4 (2015).

[145] Nomura, M. Regulation Ribosome Biosynthesis in *Escherichia coli* and *Saccharomyces cerevisiae*: Diversity and Common Principles. *Journal of Bacteriology 181*, 22 (1999), 6857–6864.

[146] Nomura, M., et al. Regulation of the Synthesis of Ribosomes and Ribosomal Components. *Annual Review of Biochemistry 53* (1984), 75–117.

[147] Novick, A., and Szilard, L. Experiments with the Chemostat on Spontaneous Mutations of Bacteria. *Proceedings of the Natational Academy of Sciences 36*, 12 (1950), 708–719.

[148] Ojkic, N., et al. A Roadblock-and-Kill Mechanism of Action Model for the DNA-Targeting Antibiotic Ciprofloxacin. *Antimicrobial Agents and Chemotherapy 64*, 9 (2020).

[149] Otieno, J., et al. The Occurrence and Role of *Tetrasphaera* in Enhanced Biological Phosphorus Removal Systems. *Water 14*, 21 (2022).

[150] Pacciani-Mori, L., et al. Constrained proteome allocation affects coexistence in models of competitive microbial communities. *ISME Journal 15*, 5 (2021), 1458–1477.

[151] Pace, N. R. Time for a change. *Nature 441*, 7091 (2006).

[152] Pace, N. R. Mapping the Tree of Life: Progress and Prospects. *Microbiology and Molecular Biology Reviews 73*, 4 (2009), 565–576.

[153] Pankey, G. A., and Sabath, L. D. Clinical Relevance of Bacteriostatic versus Bactericidal Mechanisms of Action in the Treatment of Gram-Positive Bacterial Infections. *Clinical Infectious Diseases 36*, 6 (2004), 864–870.

[154] Paul, B. J., et al. rRNA Transcription in *Escherichia coli*. *Annual Review of Genetics 38* (2004), 749–770.

[155] Pavlov, M. Y., and Ehrenberg, M. Optimal control of gene expression for fast proteome adaptation to environmental change. *PNAS 110*, 51 (2013), 20527–20532.

[156] Pedersen, S. *Escherichia coli* ribosomes translate *in vivo* with variable rate. *The EMBO Journal 3*, 12 (1984), 2895–2898.

[157] Peebo, K., et al. Proteome reallocation in *Escherichia coli* with increasing specific growth rate. *Molecular Biosystems 11* (2015), 1184–1193.

[158] Peretti, S. W., and Bailey, J. E. Simulations of host-plasmid interactions in *Escherichia coli*: Copy number, promoter strength, and ribosome binding site strength effects on metabolic activity and plasmid gene expression. *Biotechnology and Bioengineering 29*, 3 (1987), 316–328.

[159] Petrungaro, G., et al. Antibiotic resistance: Insights from evolution experiments and mathematical modeling. *Current Opinion in Systems Biology 28* (2021).

[160] Pinheiro, F., et al. Predicting trajectories and mechanisms of antibiotic resistance evolution. *bioRxiv* (2020). Preprint. DOI: https://doi.org/10.1101/2020.07.02.184622.

[161] Pinheiro, F., et al. Metabolic fitness landscapes predict the evolution of antibiotic resistance. *Nature Ecology & Evolution 5* (2021), 677–687.

[162] Pirt, S. J. *Priniciples of Microbe and Cell Cultivation*. Blackwell Scientific Publications, London, 1975.

[163] Podnecky, N. L., et al. Conserved collateral antibiotic susceptibility networks in diverse clinical strains of *Escherichia coli*. *Nature Communications 9*, 1 (2018).

[164] Poehlsgaard, J., and Douthwaite, S. The bacterial ribosome as a target for antibiotics. *Nature Reviews Microbiology 3*, 11 (2005), 870–881.

[165] Pontes, M. H., and Groisman, E. A. A Physiological Basis for Nonheritable Antibiotic Resistance. *mBio 11*, 3 (2020), 817–820.

[166] Poole, K. Bacterial stress responses as determinants of antimicrobial resistance. *Journal of Antimicrobial Chemotherapy 67*, 9 (2012), 2069–2089.

[167] Potrykus, K., and Cashel, M. (p)ppGpp: Still Magical? *Annual Review of Microbiology 62* (2008), 35–51.

[168] Powell, E. O. Growth Rate and Generation Time of Bacteria, with Special Reference to Continuous Culture. *Journal of General Microbiology 15*, 3 (1956), 492–511.

[169] Press, W. H., et al. *Numerical Recipes: The Art of Scientific Computing*, 3 ed. Cambridge University Press, 2007.

[170] Quinn, K. N., et al. Information geometry for multiparameter models: new perspectives on the origin of simplicity. *Reports on Progress in Physics 86*, 3 (2022).

[171] Radzikowski, J. L., et al. Bacterial persistence is an active σS stress response to metabolic flux. *Molecular Systems Biology 12*, 9 (2016).

[172] Ramakrishnan, V. Ribosome Structure Review and the Mechanism of Translation. *Cell 108*, 4 (2002), 557–572.

[173] Raue, A., et al. Structural and practical identifiability analysis of partially observed dynamical models by exploiting the profile likelihood. *Bioinformatics 25*, 15 (2009), 1923–1929.

[174] Regoes, R. R., et al. Pharmacodynamic functions: a multiparameter approach to the design of antibiotic treatment regimens. *Antimicrobial Agents and Chemotherapy 48*, 10 (2004), 3670–3676.

[175] Reyes-González, D., et al. Dynamic proteome allocation regulates the profile of interaction of auxotrophic bacterial consortia. *Royal Society Open Science 9*, 5 (2022).

[176] Ringquist, S., et al. Translation initiation in *Escherichia coli*: sequences within the ribosome-binding site. *Molecular Microbiology 6*, 9 (1992), 1219–1229.

[177] Roemhild, R., et al. The physiology and genetics of bacterial responses to antibiotic combinations. *Nature Reviews Microbiology 20*, 8 (2022), 478–490.

[178] Rogalla, P. S., et al. An equilibrium model for ribosome competition. *Physical Biology 17*, 1 (2020).

[179] Ross, J. I., et al. 16S rRNA Mutation Associated with Tetracycline Resistance in a Gram-Positive Bacterium. *Antimicrobial Agents and Chemotherapy 42*, 7 (1998), 1702–1705.

[180] Ruiz, N., and Silhavy, T. J. How *Escherichia coli* Became the Flagship Bacterium of Molecular Biology. *Journal of Bacteriology 204*, 9 (2022).

[181] Saltelli, A., et al. *Sensitivity Analysis in Practice: A Guide to Assessing Scientific Models*. John Wiley & Sons Ltd., 2004.

[182] Sanders, S., et al. Beyond the average: An updated framework for understanding the relationship between cell growth, DNA replication, and division in a bacterial system. *PLoS Genetics 19*, 1 (2023).

[183] Schaechter, M. From growth physiology to systems biology. *International Microbiology 9*, 3 (2006), 157–161.

[184] Schaechter, M., et al. Dependency on Medium and Temperature of Cell Size and Chemical Composition during Balanced Growth of *Salmonella typhimurium*. *Microbiology 19*, 3 (1958), 592–606.

[185] Schmidt, A., et al. The quantitative and condition-dependent *Escherichia coli* proteome. *Nature Biotechnology 34*, 1 (2016), 104–110.

[186] Schopf, J. W. Microfossils of the Early Archean Apex Chert: New Evidence of the Antiquity of Life. *Science 260*, 5108 (1993), 640–646.

[187] Schwarz, G. Estimating the dimension of a model. *The Annals of Statistics 6*, 2 (1978), 461–464.

[188] Scott, M. Metabolic models predict evolutionary dynamics. *Nature Ecology & Evolution 5*, 5 (2021), 560–561.

[189] Scott, M., et al. Interdependence of cell growth and gene expression: origins and consequences. *Science 330*, 6007 (2010), 1099–1102.

[190] Scott, M., et al. Emergence of robust growth laws from optimal regulation of ribosome synthesis. *Molecular Systems Biology 10*, 8 (2014).

[191] Scott, M., and Hwa, T. Bacterial growth laws and their applications. *Current opinion in biotechnology 22*, 4 (2011), 559–565.

[192] Scott, M., and Hwa, T. Shaping bacterial gene expression by physiological and proteome allocation constraints. *Nature Reviews Microbiology 21*, 5 (2023), 327–342.

[193] Segel, I. H. *Enzyme Kinetics: Behavior and Analysis of Rapid Equilibrium and Steady-State Enzyme Systems*. Wiley-Interscience, 1993.

[194] Si, F., et al. Invariance of initiation mass and predictability of cell size in *Escherichia coli*. *Current Biology 27*, 9 (2017), 1278–1287.

[195] Siiback, T., et al. Antibiotic-induced ribosomal assembly defects result from changes in the synthesis of ribosomal proteins. *Molecular Microbiology 80*, 1 (2011), 54–67.

[196] Singleton, P., and Sainsbury, D. *Introduction to Bacteria: for students in the biological sciences*. John Wiley & Sons Ltd., Chichester; New York, 1981.

[197] Smirnova, G. V., et al. Study of the contribution of active defense mechanisms to ciprofloxacin tolerance in *Escherchia coli* growing at different rates. *Antonie van Leeuwenhoek 115*, 2 (2022), 233–251.

[198] Steinchen, W., et al. (p)ppGpp: Magic Modulators of Bacterial Physiology and Metabolism. *Frontiers in Microbiology 11* (2020).

[199] Stokes, J. M., and Brown, E. D. Chemical modulators of ribosome biogenesis as biological probes. *Nature Chemical Biology 11*, 12 (2015), 924–932.

[200] Stokes, J. M., et al. Discovery of a small molecule that inhibits bacterial ribosome biogenesis. *eLife 3* (2014).

[201] Strogatz, S. H. *Nonlinear Dynamics and Chaos: With Applications to Physics, Biology, Chemistry, and Engineering*, 2 ed. CRC Press, 2018.

[202] Sun, J., et al. Bacterial multidrug efflux pumps: Mechanisms, physiology and pharmacological exploitations. *Biochemical and Biophysical Research Communications 453*, 2 (2014), 254–267.

[203] Svetlov, M. S., et al. Kinetics of drug–ribosome interactions defines the cidality of macrolide antibiotics. *PNAS 114*, 52 (2017), 13673–13678.

[204] Swanson, M., et al. *Microbe*, 2nd ed. American Society for Microbiology Press, Washington DC, 2016.

[205] Tadmor, A. D., and Tlusty, T. A Coarse-Grained Biophysical Model of *E. coli* and Its Application to Perturbation of the rRNA Operon Copy Number. *PLoS Computational Biology 4*, 5 (2008).

[206] Takano, S., et al. Inference of transcriptome signatures of *Escherichia coli* in long-term stationary phase. *Scientific Reports 13*, 1 (2023).

[207] Taniguchi, Y., et al. Quantifying *E. coli* proteome and transcriptome with single-molecule sensitivity in single cells. *Science 329*, 5991 (2010), 533–538.

[208] Tereshchenkov, A. G., et al. Binding and action of amino-acid analogues of chloramphenicol upon the bacterial ribosome. *Journal of Molecular Biology 430*, 6 (2018), 842–852.

[209] Toprak, E., et al. Building a morbidostat: an automated continuous culture device for studying bacterial drug resistance under dynamically sustained drug inhibition. *Nature Protocols 8*, 3 (2013), 555–567.

[210] Tozer, T. N., and Rowland, M. *Introduction to Pharmacokinetics and Pharmacodynamics*. Lippincott Williams & Wilkins, Baltimore, 2006.

[211] Trickovic, B., and Lynch, M. Resource allocation to cell envelopes and the scaling of bacterial growth rate. *Physical Biology 22*, 4 (2025).

[212] Tritton, T. R. Ribosome-Tetracycline Interactions. *Biochemistry 16*, 18 (1977), 4133–4138.

[213] Turnbaugh, P. J., et al. The Human Microbiome Project. *Nature 449*, 7164 (2007), 804–810.

[214] Utrilla, J., et al. Global Rebalancing of Cellular Resources by Pleiotropic Point Mutations Illustrates a Multi-scale Mechanism of Adaptive Evolution. *Cell Systems 2*, 4 (2016), 260–271.

[215] Valgepea, K., et al. *Escherichia coli* achieves faster growth by increasing catalytic and translation rates of proteins. *Microbiology and Molecular Biology Reviews 9* (2013), 2344–2358.

[216] Van Boeckel, T. P., et al. Global trends in antimicrobial use in food animals. *Proceedings of the National Academy of Sciences 112*, 18 (2015), 5649–5654.

[217] Verhulst, P. Notice on the law that a population follows in its growth. *Correspondance in Mathematical Physics 10* (1838), 113–121.

[218] Vila, J., et al. *Escherichia coli*: an old friend with new tidings. *FEMS Microbiology Reviews 40*, 4 (2016), 437–463.

[219] Vinogradova, D. S., et al. How the initiating ribosome copes with ppGpp to translate mRNAs. *PLoS Biology 18*, 1 (2020).

[220] Wang, P., et al. Robust growth of *Escherichia coli*. *Current Biology 20*, 12 (2010), 1099–1103.

[221] Wassenaar, T. M. *Bacteria: The Benign, the Bad, and the Beautiful.* Wiley-Blackwell, 2011.

[222] Weber, A., et al. Time-Dependent Proteome Alterations under Osmotic Stress during Aerobic and Anaerobic Growth in *Escherichia coli*. *Journal of Bacteriology 188*, 20 (2006), 7165–7175.

[223] Wecke, T., and Mascher, T. Antibiotic research in the age of omics: from expression profiles to interspecies communication. *Journal of Antimicrobial Chemotherapy 66*, 12 (2011), 2689–2704.

[224] Wellington, E. M. H., et al. The role of the natural environment in the emergence of antibiotic resistance in Gram-negative bacteria. *The Lancet Infectious Diseases 13*, 2 (2013), 155–165.

[225] Whitman, W. B., et al. Prokaryotes: The unseen majority. *Proceedings of the National Academy of Sciences 95*, 12 (1998), 6578–6583.

[226] Wickner, S., et al. Posttranslational Quality Control: Folding, Refolding, and Degrading Proteins. *Science 286*, 5446 (1999), 1888–1893.

[227] Wilson, D. N. The A–Z of Bacterial Translation Inhibitors. *Critical Reviews in Biochemistry and Molecular Biology 44*, 6 (2009), 393–433.

[228] Wilson, D. N. Ribosome-targeting antibiotics and mechanisms of bacterial resistance. *Nature Reviews Microbiology 12*, 1 (2014), 35–48.

[229] Wlodarski, M., et al. Cytosolic Crowding Drives the Dynamics of Both Genome and Cytosol in *Escherichia coli* Challenged with Sub-lethal Antibiotic Treatments. *iScience 23*, 10 (2020).

[230] Woolstenhulme, C. J., et al. Nascent peptides that block protein synthesis in bacteria. *PNAS 110*, 10 (2013), 878–887.

[231] Wortel, M. T., et al. Evolutionary pressures on microbial metabolic strategies in the chemostat. *Scientific Reports 6* (2016).

[232] Wu, C., et al. Enzyme expression kinetics by *Escherichia coli* during transition from rich to minimal media depends on proteome reserves. *Nature Microbiology 8* (2023), 347–359.

[233] Yang, L., et al. Principles of proteome allocation are revealed using proteomic data and genome-scale models. *Scientific Reports 6* (2016).

[234] Yang, Y., et al. Changes in the Carbon Metabolism of *Escherichia coli* During the Evolution of Doxycycline Resistance. *Frontiers in Microbiology 10* (2019).

[235] Yonath, A. Antibiotics Targeting Ribosomes: Resistance, Selectivity, Synergism, and Cellular Regulation. *Annual Review of Biochemistry 74* (2005), 649–679.

[236] Young, R., and Bremer, H. Polypeptide-Chain-Elongation Rate in *Escherichia coli* B/r as a Function of Growth Rate. *Biochemical Journal 160*, 2 (1976), 185–194.

[237] Zhang, Q., et al. Acceleration of Emergence of Bacterial Antibiotic Resistance in Connected Microenvironments. *Science 333*, 6050 (2011), 1764–1767.

[238] Zhang, Q., et al. A Decrease in Transcription Capacity Limits Growth Rate upon Translation Inhibition. *mSystems 5*, 5 (2020).

[239] Zhou, Q., et al. Phylogenomics of 10,575 genomes reveals evolutionary proximity between domains Bacteria and Archaea. *Nature Communications 10* (2019).

[240] Zhu, M., and Dai, X. Maintenance of translational elongation rate underlies the survival of *Escherichia coli* during oxidative stress. *Nucleic Acids Research 47*, 14 (2019), 7592–7604.

[241] zur Wiesch, P. A., et al. Using Chemical Reaction Kinetics to Predict Optimal Antibiotic Treatment Strategies. *PLoS Computational Biology 13*, 1 (2017).

APPENDIX

Code Availability

The full codebase used for model simulations, parameter optimization, and figure generation is available at: https://github.com/BrittanyH06/PhD-Thesis-Code

The repository reflects the code as used in the thesis. See the repository's README for instructions on installation, dependencies, and formatting of user-supplied data.